공학박사학위논문

Theoretical and Experimental Exploration to Maximizing the Tensile Performance of Carbon Nanotube Yarns

탄소나노튜브 섬유의 인장 성능 극대화를 위한 이론 및 실험적 연구

2021년 8월

서울대학교 대학원

재료공학부

조 영 식

Theoretical and Experimental Exploration to Maximizing the Tensile Performance of Carbon Nanotube Yarns

탄소나노튜브 섬유의 인장 성능 극대화를 위한 이론 및 실험적 연구

지도교수 박 종 래

이 논문을 공학박사 학위논문으로 제출함

2021년 4월

서울대학교 대학원

재료공학부

조 영 식

조 영 식의 박사학위논문을 인준함

2021년 6월

위 원 장		장 지 영
부 위 원 장		박 종 래
위 원		유 웅 열
위 원		선 정 윤
위 원		김 세 훈

Abstract

Theoretical and Experimental Exploration to Maximizing the Tensile Performance of Carbon Nanotube Yarns

Young Shik Cho

Department of Materials Science and Engineering

The Graduate School

Seoul National University

This study theoretically describes the model of carbon nanotube yarns (CNTYs) with empirical verification to maximize the mechanical performance. Due to the inherently superb mechanical properties and high aspect ratios of CNTs, efforts to improve the mechanical properties of CNTYs which that exceed those of conventional high-strength fibers such as carbon fibers have continued over the last few decades. Nevertheless, though CNT is the most attractive materials in the fields of structural materials, CNT assembly including CNTY shows relatively very low mechanical performance in macroscopic scale comparing to the strength of individual CNTs in nanoscale. To overcome the limitation, new insight for correlation between properties of CNT and CNTY should be considered. The mechanical properties of CNT assembly depend on structural factors of CNT such as the length, number of walls, and the diameter of the

nanotubes. Therefore, the most important issue to fabricate ultrahigh-strength CNTY is to control the nanostructure of CNTs and the microstructure of the CNT assembly by revisiting the hierarchy of CNTYs.

Chapter 1 briefly describes the CNTYs and related factors that affect the mechanical properties of yarns. As discussed in state-of-the-art of strength of CNTY based on structural factors of CNT, previous works based on conventional yarn mechanics does not provide a guideline and insight for high strength CNTY. This study attempts to draw possible correlations between the intrinsic and extrinsic structural parameters of load-bearing elements and the specific strength of the resulting CNTYs to improve the mechanical properties of CNTY

Chapter 2 presents the theoretical model related to the specific strength of CNTYs based on consideration of load-bearing element. On the basis of energy calculation, the actual load-bearing element, which is CNT elementary bundle, of CNTY is determined. By revisiting failure mechanism, slippage of load-bearing element, the equation describing the specific strength of CNTYs is derived based on the structural factors of elementary bundle relying on the intrinsic structure of CNTs. Through the relation between the specific strength of CNTYs and nanostructure of component CNT elementary bundle, dependence of CNTY strength on CNT assembly structure and basic load-bearing element is dealt with. Finally, the ideal structure for high specific strength CNTY is proposed through the theoretical approach.

Chapter 3 and 4 discuss the reliability of theoretical approach by comparing the specific strength of CNTYs made of various nanostructured CNTs as derived from chapter 2. In chapter 3, effect of microstructure of CNT microbundle is investigated through *in-situ* direct spinning which enables the control of the self-assembly behavior

of CNT. The strength of fabricated as-spun CNTY successfully reached 80% of the empirically estimated maximum strength according to the theory in chapter 2. In chapter 4, a simplified model of crosslinked CNT yarn derived from chapter 2 to predict the main factors influencing the strength of the yarn is suggested in function of degree of reaction. By giving variety to linking reagent or degree of reaction and analyzing junction of linking reagent and surface of CNT from reaction, developed model fitted well to experimental data, giving basis to the model as well as insight to the strategy to strengthen CNTY. Finally, through applying the model in chapter 3 and 4, ultra-high strength CNTY was realized.

Chapter 5 suggests the method of maximizing the tensile strain and modulus of CNTY. The empirical approach, which is modified *in-situ* direct spinning, to increase elongation and modulus of CNTY is proposed. Through self-assembly control during spinning, elongation specialized CNTY and modulus specialized CNTY are prepared and analyzed based on bundling and orientation properties.

Contents

List of Tables

List of Figures

Part I. Fundamental backgrounds

Chapter 1 Introduction

1.1 Overview of CNTYs

Carbon nanotubes (CNTs), composed of a network of sp^2 hybridized carbons with outstanding mechanical properties, viz. the theoretical tensile strength of 60 GPa and modulus of 1 TPa [1-3]. The one-dimensional morphological features with high aspect ratio are very attractive, particularly when considered as basic building blocks for high-performance CNT yarns (CNTYs) [4-13]. However, in practice, such unprecedented advantages of CNTs have not yet been realized regardless of CNTs that have been applied in CNTYs. The tensile strength of CNTY ranged from 0.05 to 5.53 GPa, though this is far below the theoretical tensile strength of CNTs.

1.2 Theoretical consideration of the tensile strength of CNTYs

CNTY is commonly considered a one-dimensional material composed of interlocked elementary fibers, i.e., CNTs [14-17]. Thus, the tensile strength ratio of the yarn to the elementary fiber has been estimated by the classical yarn mechanics theory [18] described by equation (1.1),

$$\frac{\sigma_{yarn}}{\sigma_{fiber}} \approx cos^2\alpha[1 - (k \text{ cosec } \alpha)] \qquad (1.1)$$

where σ_{yarn} and σ_{fiber} are the strengths of the CNTY and the elementary fiber, or CNT, respectively.

According to equation (1.1), the yarn strength depends on the value of k on the twist angle (α), the fiber diameter (d), and the fiber length (L) of the elementary fibers (CNTs). The term $\cos^2\alpha$ describes a gradual decline of the yarn strength as the twist angle of the elementary fibers increases. The second term $[1-(k\ \mathrm{cosec}\alpha)]$ compensates for the drop-off effect of the yarn strength due to the increased transverse force from twisting. As the twist angle increases, the distance between the CNTs becomes narrower and the degree of yarn compaction becomes higher, resulting in a strengthening of the inter-tubular interactions.

Excluding the effect of twist angle, the yarn strength is determined by the material term $k=(dQ/\mu)^{0.5}/(3L)$, where d is the diameter of elementary fiber, Q is the migration length of the fibers from the yarn surface to the inside, μ is the friction coefficient of the fiber with the neighboring fibers, and L is the length of the fiber. This describes a contribution factor of the unit length of elementary fibers. Equation (1.1) shows how a shorter diameter, shorter migration length, higher friction coefficient, and a longer length of the elementary fibers are advantageous for stronger yarns.

Although equation (1.1) suggests that the longer and thinner the elementary CNTs are, the stronger the CNTY would be, this equation does not appear to be feasible when applied to a practical CNTY. There are two reasons for this; first is the dimensional difference and the second is the deformability of CNTs. Indeed, in the equation derived originally for cotton or woolen yarns, the elementary fibers - given their micron-sized diameters and millimeter-sized lengths - were considered non-deformable cylinders of a uniformly specific volume with a circular cross-section. Meanwhile, actual CNTs with

3

nanometer-sized diameter and micron-sized length are deformable, with the deformability depending on the structural parameters.

To overcome the limitations of equation (1.1), Vilatela et al. [15] developed a new equation by considering that the failure of CNT yarns consisting of millions of elementary CNTs is governed not by the rupture of elementary CNT, but by the pull-out due to weak interaction between CNTs. As described in equation (1.2), the strength of the CNT yarn strongly depends on the shear strength between elementary CNTs.

$$\sigma = \frac{1}{6n}\Omega_{CNT}\tau_{F}L \qquad (1.2)$$

where τ_F and L are the shear strength and the length of elementary CNTs. Since only the outermost tube layer contributes to the shear force between adjacent tubes where the basic load-bearing element is a single nanotube, the total strength is divided by n, where n is the number of nanotube walls. The term of Ω_{CNT}, derived from a classical elasticity theory, is the fraction of outer layer surface in contact with neighboring CNTs [19]. Due to the unique hollow nanostructure, the elementary CNTs are deformable, implying that the larger diameter of CNTs is easier to be deformed so as to increase the contact area between the elementary CNTs. However, this equation does not fully describe the strength of the yarn due to the hierarchy of CNTY. The equation only describes the strength of the CNT bundle rather than that of CNTY.

It should be noted that both equations (1.1) and (1.2) suggest the importance of the interfacial shear strength and the structural factor of the elementary CNTs when

attempting to make CNTYs stronger. These factors are a function of multiple variables like the length, diameter, surface roughness, orientation, and degree of crosslinking. It is necessary to gain a deep understanding of these parameter influences to see how to improve the CNTY strength.

1.3 The state-of-the-art of tensile performance of CNTYs

1.3.1 Influence of the structural features of CNTs on the resulting yarn strength

1.3.1.1 Length of CNTs

In the theories that predict the tensile strength of CNTYs, one of the most influential parameters is the interaction energy between the CNTs that dissipates the crack propagation energy based on the slippage failure mechanism. For this reason, there have been many efforts to synthesize long CNTs so as to increase the interaction forces by extending the contact area between the CNTs with weak shear strength [20-24]. For example, CNT arrays that were 2.2 cm [25] or 4.7 mm [21] long were successfully synthesized, but only CNTs in the range of 0.5~1.5 mm could be spun into a yarn. Zhang et al. [20] and Ghemes et al. [26] prepared CNT arrays with lengths in the range of 0.3~2 mm, which were spun into yarns. Fig. 1.1 clearly illustrates that the strength of the CNTY increases linearly with the length of the elementary CNTs.

It is crucial to note here that despite a clear correlation, the strength of the resulting CNTYs from millimeter-long CNTs, as shown in Fig. 1.1b, is lower than that of micrometer-long CNTs, as presented in Fig. 1.1a. This indicates that if structural characteristics other than the length of the elementary CNTs are identical, a linear correlation becomes true. In other words, there are other structural parameters like the tube diameter and the number of walls that affect the evolution of CNTY strength.
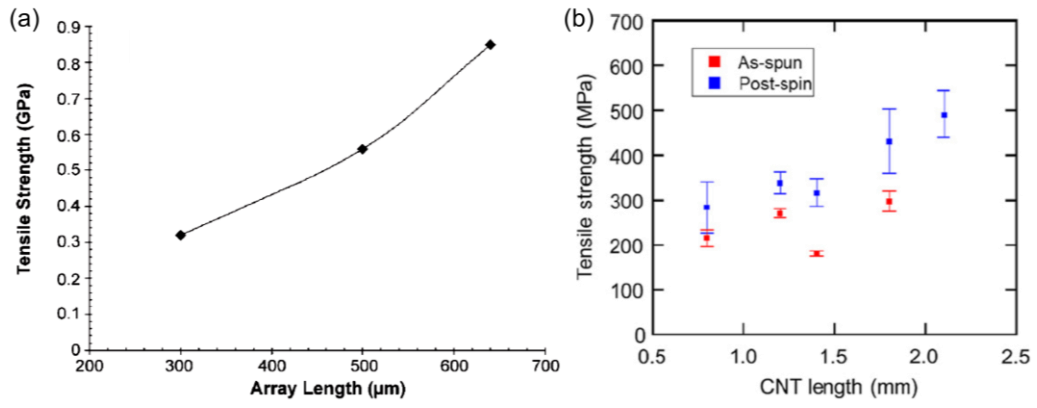
Fig. 1. 1. Dependence of tensile strengths of MWCNT yarns on the length of elementary CNTs: (a) in micron scale [20, 26] and (b) in millimeter scale [35], Reproduced with permission. Copyright 2012, Elsevier.

1.3.1.2 Diameter and number of walls of CNTs

Given the length of elementary CNTs, the strength of the resulting CNTYs varies significantly with the diameter and the number of walls of the CNTs, thus determining the extent of inter-tubular interactions. Jia et al. [27] elaborately controlled the synthesis conditions in their effort to synthesize CNT arrays with different numbers of walls ranging from a few walls (2-3) to multiple walls (>15) that have lengths in the range of 260~1000 µm. They then tested the strength of the resulting CNTYs with controlled diameters of 10-15 µm.

From Table 1.1, it is clear that the maximum strength of CNTYs is achieved when the elementary CNTs have the smallest diameters and fewest walls. Using the data in Table 1.1, we calculated the parameters in equations (1.1) and (1.2), (i.e., $L/(2R_n)$, $L/(2R_n)^{0.5}$, Ω_{CNT}/n, and $L\Omega_{CNT}/n$) and plotted them in relation to the yarn strength as shown in Fig. 1.2. Here, Ω_{CNT} was approximated as $1-(nD_G/2\gamma R_n^2)^{0.5}$, where D_G, γ, and R_n are the bending rigidity of the graphene layer, the surface energy of the graphene layer, and the outer radius of CNT, respectively. The surface energy and flexural rigidity are 0.0597 J/m^2 and 2.11×10^{-19} J, respectively [28, 29]. However, as shown in Fig 1.2, both classical yarn mechanics and classical elasticity theory (equation (1.1) and equation (1.2), respectively) failed to describe the relationship between the structural features of the elementary CNTs and the resultant CNTY strength.

Table 1.1. Effect of diameter and number of walls of elementary CNTs on the tensile strength of resulting CNTYs. Adapted from ref. [27]. Copyright 2011, Elsevier.

Carbon source	C_2H_2- I	C_2H_2- II	C_2H_4	C_2H_2-CM
Tube diameter (nm)	8-10	8-10	< 6	> 17
Number of walls	8-10	~ 6	2-3	> 15
I_G/I_D	0.88	0.99	1.27	1.65
Length (µm)	320	320	260	1000
Strength (MPa)	689	866	1170	383
Modulus (GPa)	10.1	16.0	53.5	6.5
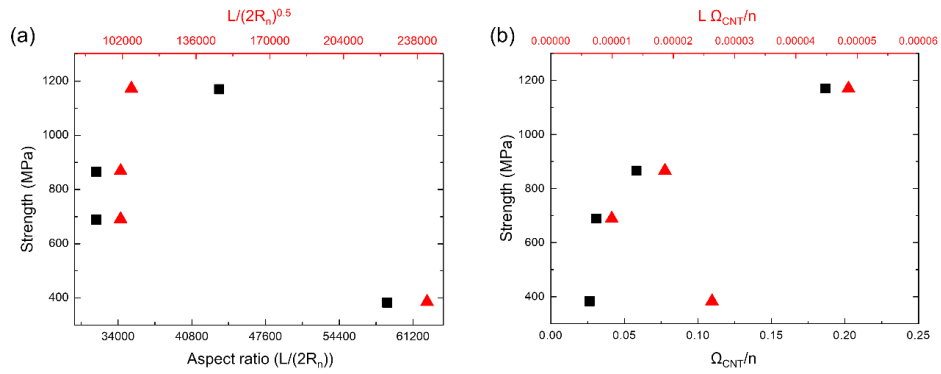
Fig. 1.2. Yarn strength as a function of the different variables of $L/(2R_n)$, $L/(2R_n)^{0.5}$, Ω_{CNT}/n and $L\Omega_{CNT}/n$. Here, the data in Table 1.1 were used to calculate the value of each variable.

1.3.1.3 Orientation of CNTs

Apart from the intrinsic structural characteristics of elementary CNTs, there are other factors that influence the strength of CNTYs, as indicated by conventional yarn mechanics. These include the orientation of the elementary CNTs along the loading axis, which crucially influence the compaction of the elementary CNTs, or the load bearing efficiency.

During the wet spinning of CNTY, the orientation of elementary CNTs can be enhanced by using a spinning dope where CNTs form a lyotropic-nematic liquid crystalline-like phase [10, 25, 45]. During the direct spinning process, CNTs assemble *in-situ* into a yarn form in the gas phase. Alemán et al. [30] demonstrated a means of controlling the orientation of the elementary CNTs in the resulting yarn by diluting the concentration of the CNTs in a reactor as shown in Fig. 1.3. The concentration of CNTs in the reactor critically determines the draw ratio of the CNT aerogel and the orientation of the elementary CNTs in the resulting CNTYs. With a low feed rate of the carbon source for CNT synthesis and a high draw ratio up to 18, the specific strength of the resulting CNTYs was improved from 0.3 to 1 GPa/SG [30].

The winding speed of the yarn is also an effective variable when attempting to control the orientation of elementary CNTs in the yarn [31] as shown in Fig. 1.4. By controlling the winding speed, an extremely high specific strength of 3 N/tex (equivalent to 3 GPa/SG) of CNTYs was obtained.
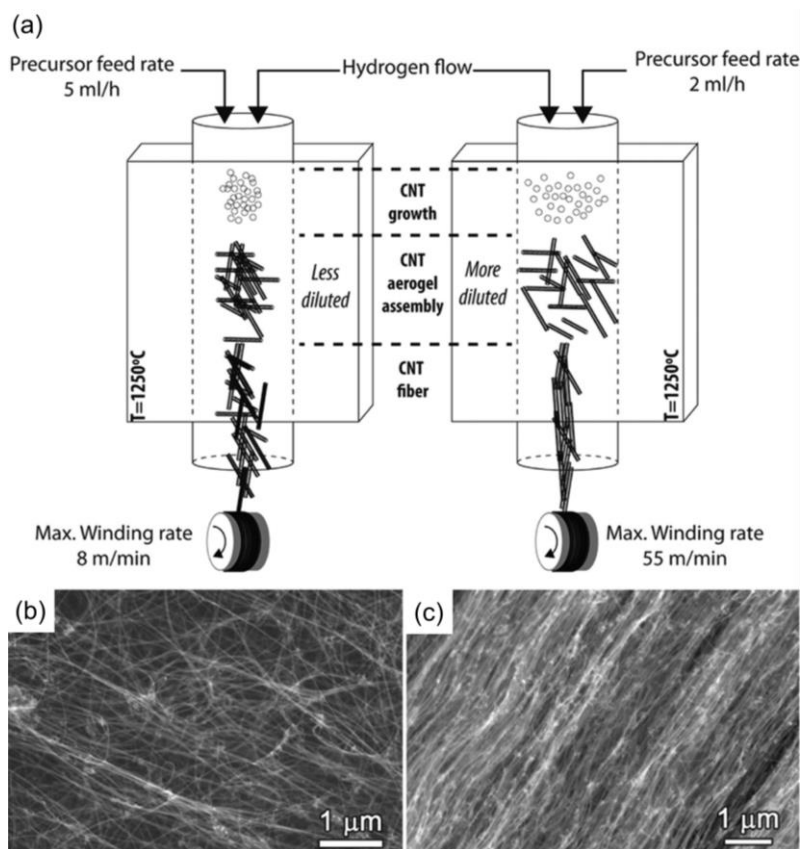
Fig. 1.3. A way of controlling the alignment of CNTs in a direct CNTY formation by diluting the concentration of CNTs in a reactor (a) a schematic representation of the direct CNTY spinning process showing the effect of aerogel dilution on the orientability of the final fibers, and scanning electron micrographs of (b) nonoriented and (c) oriented CNTYs. Reproduced with permission.[30] Copyright 2015, ACS Publications.
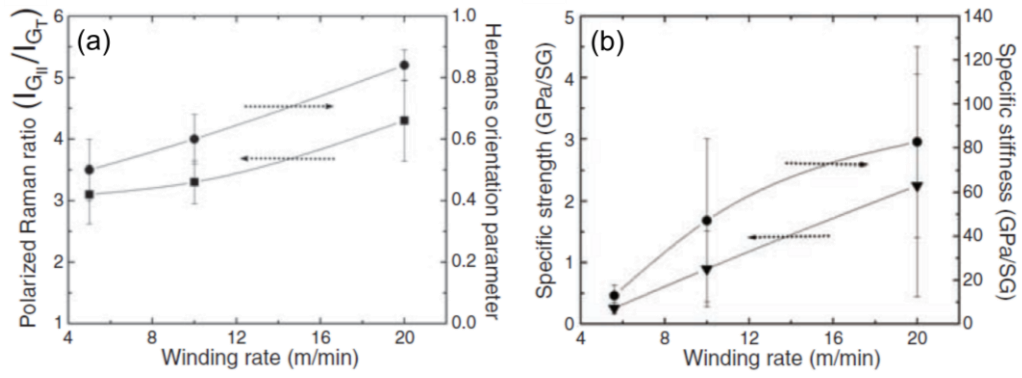
Fig. 1.4. Effect of winding rate on (a) the orientation and (b) the average specific strength and stiffness of CNTYs at 2-mm gauge length. From ref. [31]. Reprinted with permission from AAAS.

1.3.2 Enhancement of contact between CNTs

1.3.2.1 Physical densification

Improvements in the strength of CNTY can be achieved by two approaches: reducing the cross-sectional area of the CNTYs under a given load and increasing the load-bearing capacity by increasing the inter-tubular interactions under a given cross-sectional area of the yarn. In this vein, any effort to maximize the inter-tubular interactions can be effective not only to reduce the effective cross-sectional area of the CNTY, but also to increase the load bearing capability through enhanced interactions.

One of the most commonly adopted methods to reduce the cross-sectional area of CNTYs is by solvent densification [32-36]. Among the various types of solvents used for this process (i.e., non-polar, polar protic, and polar aprotic), ethylene glycol was reported as the most effective when used to densify CNTYs, implying that polarity is the key factor due to the dipole-induced interaction among CNTs. Fig. 1.5 shows the improvements in the average strength and electrical conductivity of CNTYs after solvent densification.

Mechanical densification means, such as pressing CNTYs between rollers as shown in Fig. 1.6, has also been reported to have great potential in improving the tensile strength of CNTYs [37-40]. Indeed, Wang et al. [37] demonstrated that the average tensile strength of CNTY can be improved by up to 4.34 GPa after mechanical densification due to the synergetic effect of the reduced cross-sectional area by a factor of ~10 with an increase in the load-bearing capacity by 120% through enhanced inter-tubular interactions. Table 1.2 shows the effectiveness of mechanical pressure when utilized to increase the packing density and mechanical performance of CNTY.

However, there is an upper limit with regards to the compaction of elementary CNTs in a CNTY, as the density of CNTY cannot surpass the density of graphite - 2.23 g cm^{-3}

- even if the elementary CNTs are fully collapsed and flattened without any inter-tubular space.
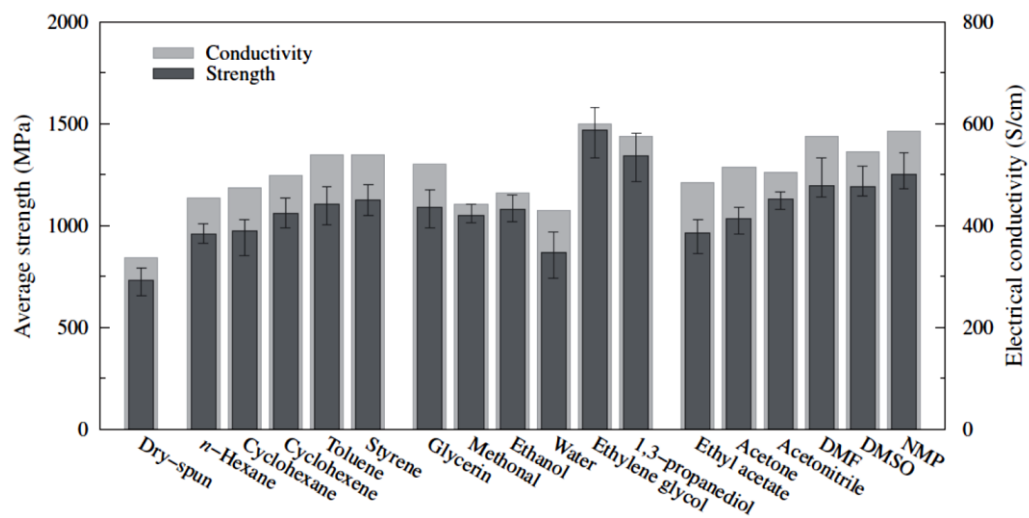
Fig. 1.5. Tensile strength and electrical conductivity of CNTYs after solvent densification. Reproduced with permission.[35] Copyright 2012, Elsevier.
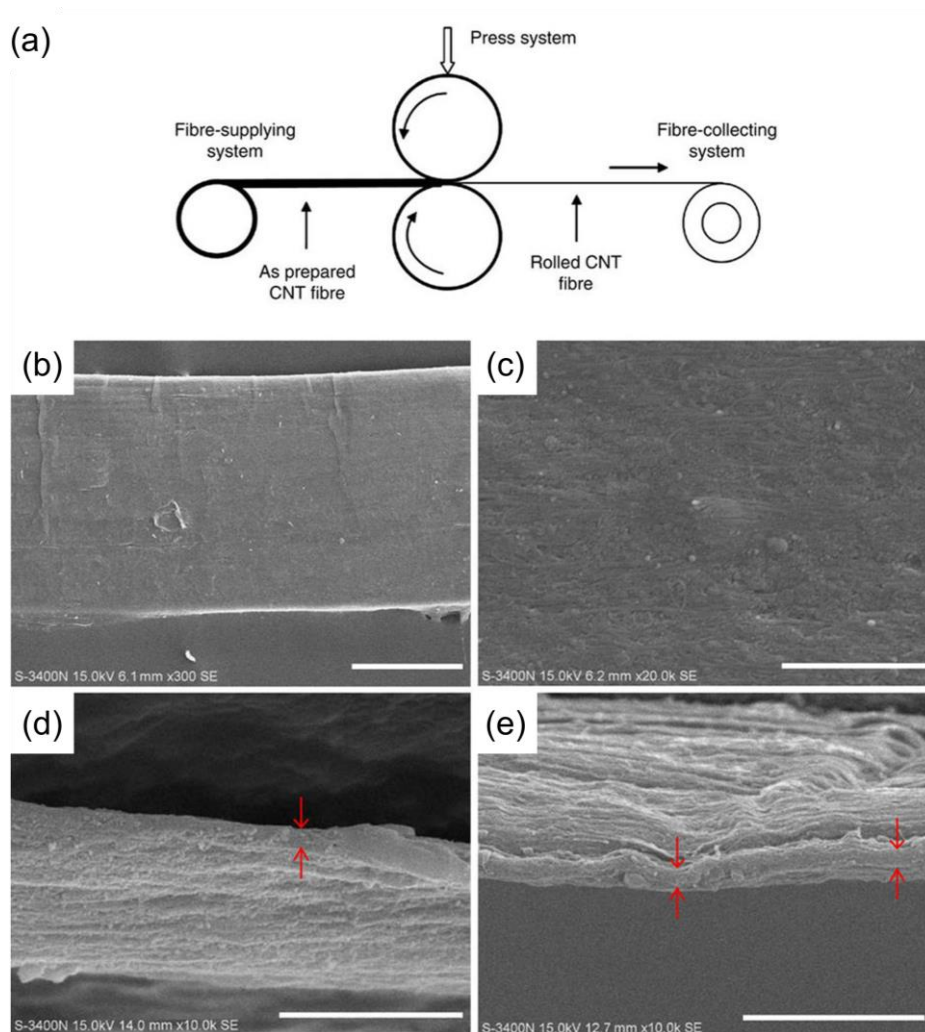
Fig. 1.6. (a) A schematic representation of mechanical densification of CNTY, (b~e) SEM micrographs after rolling, showing a smooth surface morphology. Scale bars, 100 mm (b), 2 mm (c) and 5 mm (d,e). Reproduced with permission.[37] Copyright 2014, Nature Publishing Group.

Table 1.2. Mechanical densification effect on the tensile strength of cylindrical and ribbon-like SWCNT yarns. Reproduced with permission.[38] Copyright 2016, Royal Society of Chemistry.

Sample	Diameter/width × thickness (μm)	Apparent density (g cm^{-3})	Breaking elongation (%)	Tensile strength (MPa)	Young's modulus (GPa)	Treatment pressure (GPa)
Cylindrical fiber 1	Φ: 280	0.68	13.7	17	0.35	-
Cylindrical fiber 2	Φ: 300	0.53	27	18	0.30	-
Ribbon-like fiber 1	800 × 36	1.11	4.8	300	6.5	0.9
Ribbon-like fiber 2	1500 ×13	1.53	1.5	700	50	2.1
Ribbon-like fiber 3	1600 × 13	1.54	1.8	720	72	2.7
Ribbon-like fiber 4	1800 × 8	1.66	1.2	960	81	3.7

1.3.2.2 Polymeric or carbon mediator

Based on the slippage failure mechanism, the strength of CNTYs can basically be ascribed to the shear strength between the elementary CNTs. There have been many efforts to improve the shear strength by infiltrating mediating materials, such as polymers or carbon materials, into the inter-tubular spaces. For example, Ma et al. [41] experimentally demonstrated that the load-transfer efficiency between elementary CNTs improves greatly from 0.045 to 0.4 by infiltrating polymers (e.g. polyvinyl alcohol) (PVA) [34, 35, 41-43].

Apart from linear chain polymers, cross-linkable polymers like epoxy and bismaleimide (BMI) have also been widely adopted for CNTY strengthening [35, 41, 44-47]. Ryu et al. [46] introduced mussel-inspired catecholamine polymer (PEI-C) infiltrated CNTYs in order to achieve strength levels exceeding 2 GPa.

Carbon-coated CNTYs are another route to achieving higher strength. For example, Hahm et al. [48] showed a dramatically enhanced tensile strength level of CNTYs. An increase from 0.068 to 0.80 GPa is possible when using a core of CNTY and a glassy carbon shell as shown in Fig. 1.7a. Similarly, Ryu et al. [49] also showed greatly increased tensile strength up to 4.0 GPa, which is nearly 400 % higher than the tensile strength of pure CNTY. This was achieved by fabricating CNTYs with a carbonized polydopamine (PDA) coating as shown in Fig. 1.7b.
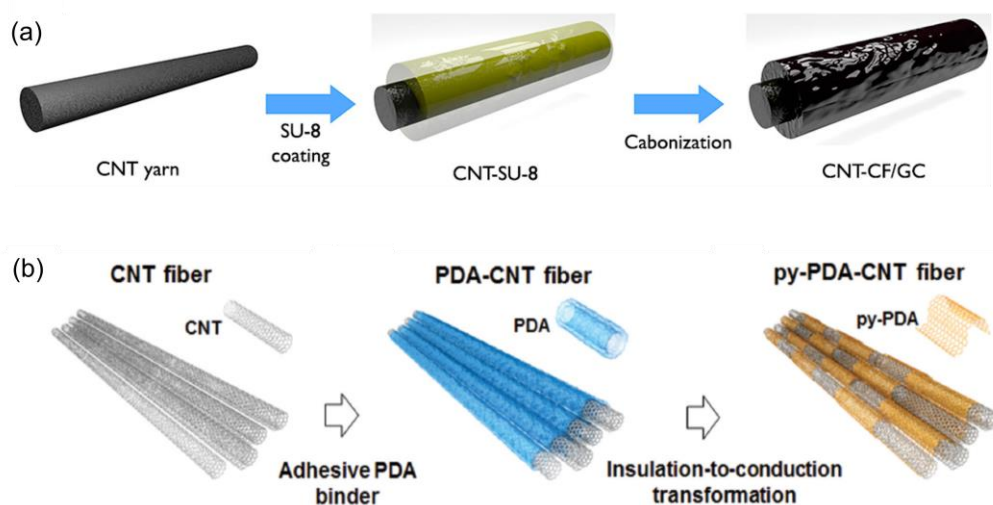
Fig. 1.7. The fabrication process of (a) CNTY/GC core/shell type yarns, (b) PDA-CNTY and py-PDA-CNTY. Reproduced with permission.[48, 49] Copyright 2013, ACS Publications and Copyright 2015, Wiley-VCH.

1.3.3 Improvement of interfacial shear strength of CNTs

1.3.3.1 Surface modification of CNTs

As chemically strengthened CNTYs were produced mostly by a wet-process, chemical modification methods can be classified into three types on the basis of the functional groups attached to the surfaces of the elementary CNTs.

The first method enhances the van der Waals interactions without attaching further functional groups. Impurities and defects, such as sp^3 carbons, are usually considered as obstacles for π-π interaction. Thus, the eliminating impurities and restoring sp^2 carbons can increase the interaction forces between the elementary CNTs [50-53]. A typical example of this can be found in the work of Choi et al. [50], which reported CNTYs with an improved strength value of 420 MPa after removing defects in a sp^2 conjugated system of CNT walls through intramolecular cross-dehydrogenative coupling (ICDC), which converts sp^3 carbons into sp^2 carbons as shown in Fig. 1.8.

The strength of as-spun CNTY is relatively low due to the weak inter-tubular interaction between CNTs, which is van der Waals interaction or π-π interaction between CNTs. It is reasonable to enhance the inter-tubular interaction by introducing additional strong bonds instead of the existing π-π interaction so as to realize enhanced mechanical performance of CNTYs. Hence, the second method involves introducing functional groups that induce ionic or hydrogen bonding as compared to π-π interaction [54-56]. For instance, Park et al. [54] doped CNTs with nitrogen by the thermal decomposition of an ionic liquid and successfully induced hydrogen bonds between the CNTs to obtain the resultant CNTY, which in their case showed an increased specific strength from 0.32 GPa/SG to 0.65 GPa/SG.

The third improvement method involves grafting a polymer onto the surfaces of the CNTs [56, 57]. Indeed, Naraghi et al. [57] reported a CNTY grafted with PMMA

oligomer, achieving a shear strength value of 400 MPa between CNTs due to the increased interlocking of the PMMA oligomers (Fig. 1.9).
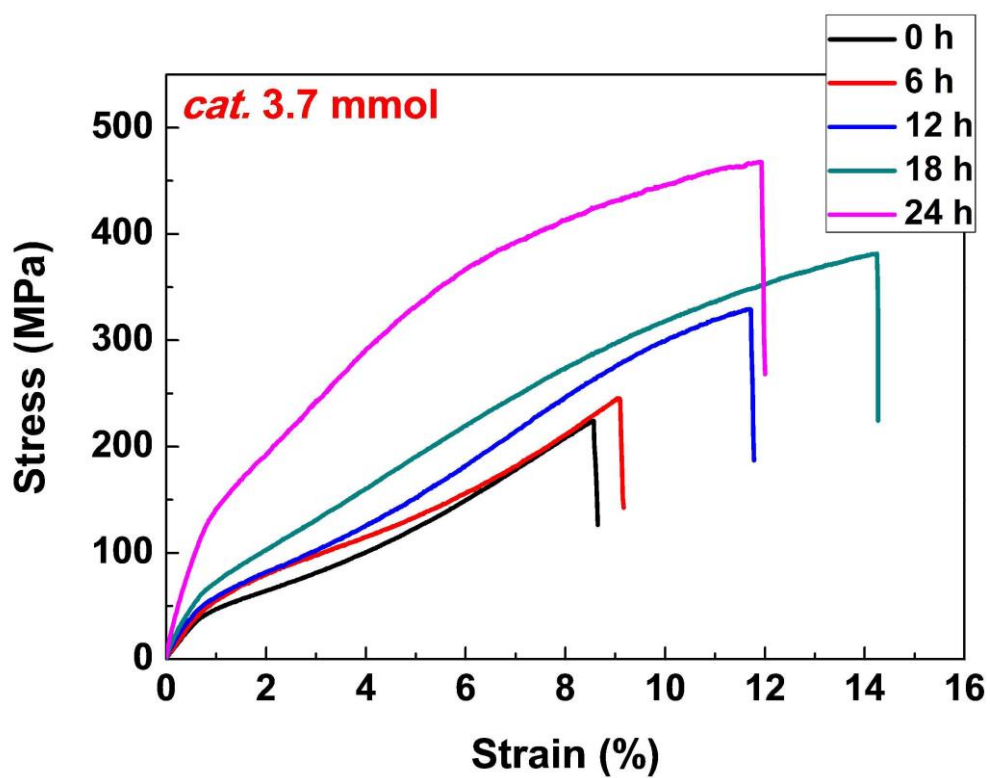
Fig. 1.8. Changes of S-S curves of CNTYs with increasing ICDC reaction time. Reproduced with permission.[65] Copyright 2013, ACS.
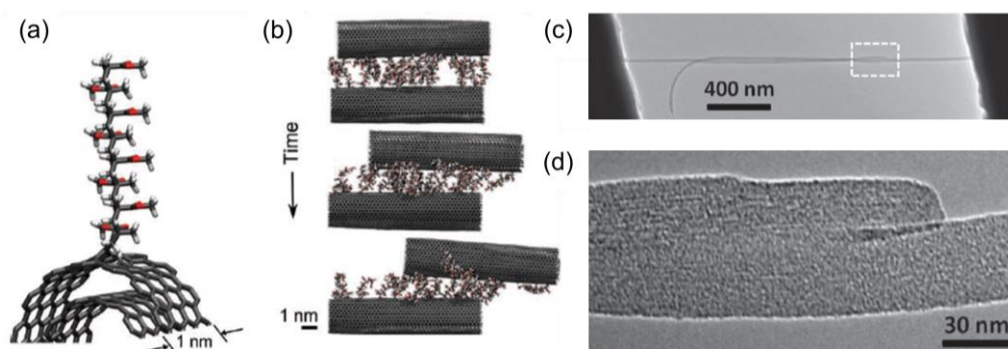
Fig. 1.9. A schematic representation of (a) PMMA grafted CNT and (b) shearing between oligomer grafted CNTs, (c) TEM micrograph of two overlapping CNTs, and (d) High-resolution TEM micrograph of the end of the oligomer grafted CNTs. Reproduced with permission.[57] Copyright 2013, Wiley-VCH.

1.3.3.2 Crosslinking between elementary CNTs

An extreme means of maximizing the inter-tubular interaction is to bond CNTs together covalently. In order to obtain the highest strength of CNTYs, the chemical crosslinking of CNTs has been considered. Cornwell and Welch [58] suggested a model of directly crosslinked CNTY as shown in Fig. 1. 10a and b exhibit yarn strength levels as high as 60 GPa, which are very close to the theoretical strengths of CNTs. If this is realized, the CNTY would fail not from slippage, but due to the CNT rupture. Furthermore, Filleter et al. [59] reported through in situ TEM tensile testing that an e-beam irradiated CNT bundle showed the strength of 17 GPa, though this remains below the theoretically predicted value. In this case, despite the direct crosslinking between CNTs, the dramatic destruction of the outer CNT wall as shown in Fig. 1.10c, was found to be a limiting factor with reference to the strength.

To avoid any structural deterioration of CNTs while preserving the crosslinking of CNTs, several linker molecules have been introduced such as aliphatic diols [60], aromatic diamines [61], reactive polymeric molecules [62], and more, as schematically shown in Fig. 1. 11. Given that as-produced CNTs do not possess any functional groups on the surface, the functionalization of CNTs is required prior to chemical crosslinking. For example, the pre-oxidation of CNTs was adopted to introduce carboxylic groups, which can participate in the crosslinking process through subsequent reactions like esterification [60] and amidation [62]. Further, diazotization of CNTs using either 4-carboxybenzenediazonium salts or p-phenylenediamine was found to be effective for the crosslinking of CNTs through the subsequent amidation of the CNTs.

It is important to note that although the strength of CNTYs could be enhanced remarkably via the chemical crosslinking of CNTs, the current state of research remains far from the theoretically predicted value. This implies that there should be further

research to find possible routes to either crosslink CNTs directly without structural deterioration or increase the degree of crosslinking between CNTs.
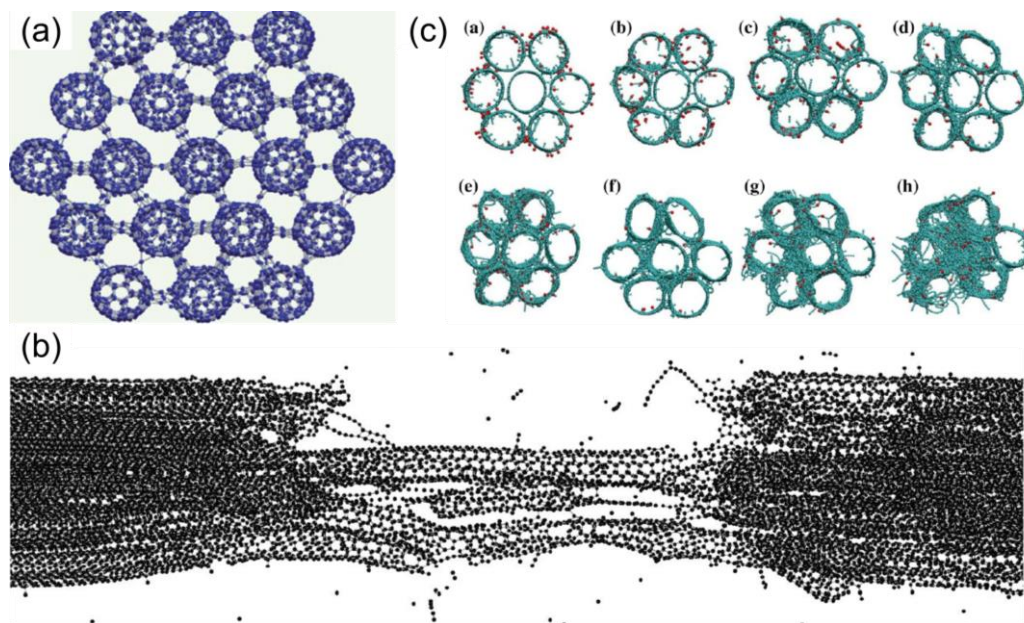
Fig. 1.10. Schematic representative of (a) directly cross-linked CNTs, (b) failure of the cross-linked CNT and (c) e-beam irradiated CNTs yarn. Reproduced with permission.[58, 63] Copyright 2011, AIP publishing and Copyright 2013, Elsevier.
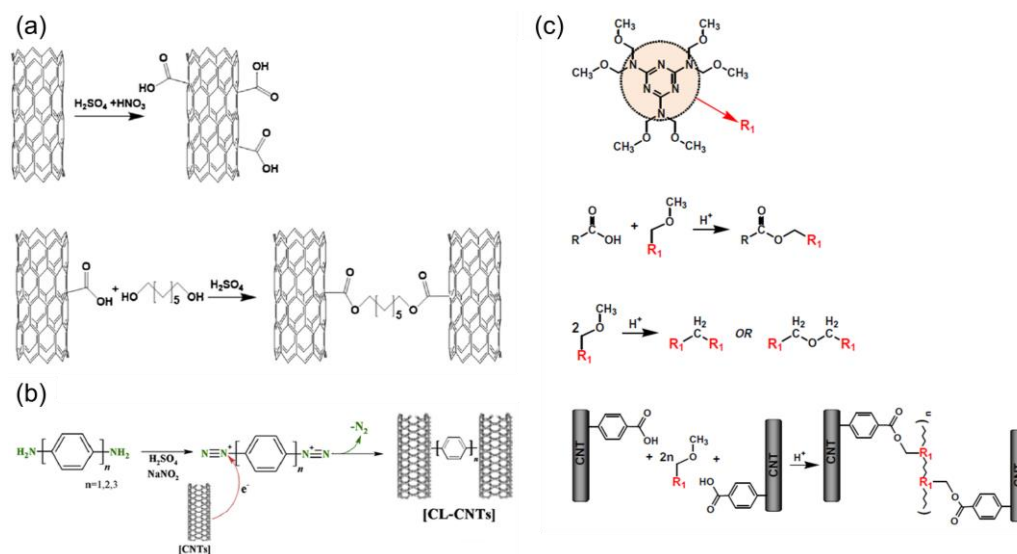
Fig. 1.11. CNT cross-linking by various chemical reagents. Reproduced with permission.[60-62] Copyright 2017, Elsevier, Copyright 2017, Elsevier and Copyright 2013, Elsevier.

27

1.4 Aim and scope of this study

The aim of this study is to design and fabricate ultra-high strength CNTY through both theoretical and empirical approaches based on structural factors and hierarchy of CNTYs. Though CNT is the most attractive material in the field of structural materials, CNT assembly shows relatively very low mechanical performance in macroscopic scale when compared to the strength of individual CNTs in nanoscale. Thus, in Part I, the state-of-the-art CNTY strength based on structural factors of CNT is analyzed. As discussed in state-of-the-art, previous works based on conventional yarn mechanics does not provide a guideline and insight for high strength CNTY. This study attempts to draw possible correlations between the intrinsic and extrinsic structural parameters of load-bearing elements and the specific strength of the resulting CNTYs.

In Part II, the method of maximizing the tensile strength of CNTY based on the theoretical derivation of CNTY strength with empirical verification is discussed. In Chapter 2, the theoretical approach related to the specific strength of CNTYs based on the load-bearing element will be considered. The actual load-bearing element, the CNT microbundle, of CNTY is determined based on the energy calculations. By revisiting the failure mechanism - slippage of load-bearing element - the equation describing the specific strength of CNTYs is derived based on the structural factors of the microbundle, which are the number and surface area fractions in contact with the length and interfacial shear strength of the microbundle relying on the intrinsic structure of CNTs. In particular, structural parameters such as length, diameter, and the number of tube walls are considered key factors affecting the microbundle to the specific strength of CNTYs. Thus, the relation between the specific strength of CNTYs and nanostructure of component CNT microbundle is discussed. In addition, the dependence of CNTY

strength on the CNT assembly structure and basic load-bearing element is dealt with. Finally, the ideal structure for high specific strength CNTY is proposed through the theoretical approach.

The reliability of the theoretical approach will be verified by comparing the specific strength of CNTYs made of various nanostructured CNTs in Chapters 3 and 4. In Chapter 3, the effect of the CNT microbundle microstructure is investigated through *in-situ* direct spinning to strengthen the CNTY. The specific strength of CNTYs with various bundle structures was analyzed according to the theory in Chapter 2 and the maximum strength possible through the *in-situ* direct spinning technique was predicted with our CNTs. Furthermore, the strength of fabricated, as-spun CNTY successfully reached 80% of the estimated maximum strength achievable. From the bundling and orientation behavior analysis of CNTs, the self-assembly behavior control was suggested as one of the most influential factors determining the specific strength of the resultant as-directly-spun CNTY.

In Chapter 4, a simplified model of crosslinked CNT yarn that predict the main factors influencing the strength of the yarn is suggested in function of the degree of reaction. To verify and realize the model, a simple method of crosslinking based on carbon surface chemistry, called cycloaddition, was hired. By giving variety to the linking reagent or degree of reaction and analyzing junction of the linking reagent and surface of CNT from the reaction, the developed model fit the experimental data well, giving basis to the model as well as insight to the strategy to strengthen CNTY. Consequently, the ultra-high strength CNTY was realized from the model.

Finally, in Part III, the method of maximizing the tensile strain and modulus of CNTY is discussed. In Chapter 5, a modified *in-situ* direct spinning, called the empirical

approach, is proposed to increase elongation and modulus of CNTY. Through self-assembly control during spinning, elongation specialized CNTY and modulus specialized CNTY are prepared and analyzed based on bundling and orientation properties.

1.5 References

[1] M.F. Yu, B.S. Files, S. Arepalli, R.S. Ruoff, Tensile loading of ropes of single wall carbon nanotubes and their mechanical properties, Phys. Rev. Lett. 84(24) (2000) 5552-5555.

[2] M.-F. Yu, O. Lourie, M.J. Dyer, K. Moloni, T.F. Kelly, R.S. Ruoff, Strength and Breaking Mechanism of Multiwalled Carbon Nanotubes Under Tensile Load, Science 287(5453) (2000) 637-640.

[3] H. Dai, E.W. Wong, C.M. Lieber, Probing electrical transport in nanomaterials: Conductivity of individual carbon nanotubes, Science 272(5261) (1996) 523-526.

[4] S.W. Kim, T. Kim, Y.S. Kim, H.S. Choi, H.J. Lim, S.J. Yang, C.R. Park, Surface modifications for the effective dispersion of carbon nanotubes in solvents and polymers, Carbon 50(1) (2012) 3-33.

[5] J.N. Coleman, U. Khan, W.J. Blau, Y.K. Gun'ko, Small but strong: A review of the mechanical properties of carbon nanotube–polymer composites, Carbon 44(9) (2006) 1624-1652.

[6] Z. Spitalsky, D. Tasis, K. Papagelis, C. Galiotis, Carbon nanotube–polymer composites: Chemistry, processing, mechanical and electrical properties, Prog. Polym. Sci. 35(3) (2010) 357-401.

[7] W. Bauhofer, J.Z. Kovacs, A review and analysis of electrical percolation in carbon nanotube polymer composites, Compos. Sci. Technol. 69(10) (2009) 1486-1498.

[8] F.H. Gojny, M.H.G. Wichmann, U. Köpke, B. Fiedler, K. Schulte, Carbon nanotube-reinforced epoxy-composites: enhanced stiffness and fracture toughness at low nanotube content, Compos. Sci. Technol. 64(15) (2004) 2363-2371.

[9] A. Allaoui, S. Bai, H.M. Cheng, J.B. Bai, Mechanical and electrical properties of a MWNT/epoxy composite, Compos. Sci. Technol. 62(15) (2002) 1993-1998.

[10] J.Y. Oh, S.J. Yang, J.Y. Park, T. Kim, K. Lee, Y.S. Kim, H.N. Han, C.R. Park, Easy Preparation of Self-Assembled High-Density Buckypaper with Enhanced Mechanical Properties, Nano Lett. 15(1) (2015) 190-197.

[11] J.Y. Oh, Y.S. Kim, Y. Jung, S.J. Yang, C.R. Park, Preparation and Exceptional Mechanical Properties of Bone-Mimicking Size-Tuned Graphene Oxide@Carbon Nanotube Hybrid Paper, ACS Nano 10(2) (2016) 2184-2192.

[12] J.Y. Oh, Y. Jung, Y.S. Cho, J. Choi, J.H. Youk, N. Fechler, S.J. Yang, C.R. Park, Metal–Phenolic Carbon Nanocomposites for Robust and Flexible Energy-Storage Devices, ChemSusChem 10(8) (2017) 1675-1682.

[13] J.Y. Oh, Y.S. Choi, S.J. Yang, J. Kim, H.S. Choi, G.D. Choi, C.H. Yun, B.K. Lee, C.R. Park, Effect of microstructure and morphological properties of carbon nanotubes on the length reduction during melt processing, Compos. Sci. and Technol. 112 (2015) 42-49.

[14] M. Zhang, K.R. Atkinson, R.H. Baughman, Multifunctional Carbon Nanotube Yarns by Downsizing an Ancient Technology, Science 306(5700) (2004) 1358-1361.

[15] J.J. Vilatela, J.A. Elliott, A.H. Windle, A Model for the Strength of Yarn-like Carbon Nanotube Fibers, ACS Nano 5(3) (2011) 1921-1927.

[16] J. Zhao, X. Zhang, J. Di, G. Xu, X. Yang, X. Liu, Z. Yong, M. Chen, Q. Li, Double-Peak Mechanical Properties of Carbon-Nanotube Fibers, Small 6(22) (2010) 2612-2617.

[17] M. Miao, The role of twist in dry spun carbon nanotube yarns, Carbon 96 (2016) 819-826.

[18] P.G. J. W. S. Hearle, Stanley Backer, Structural Mechanics of Fibers, Yarns, and Fabrics, Wiley, New York, 1969.

[19] N.G. Chopra, L.X. Benedict, V.H. Crespi, M.L. Cohen, S.G. Louie, A. Zettl, Fully collapsed carbon nanotubes, Nature 377(6545) (1995) 135-138.

[20] X. Zhang, Q. Li, Y. Tu, Y. Li, J.Y. Coulter, L. Zheng, Y. Zhao, Q. Jia, D.E. Peterson, Y. Zhu, Strong Carbon-Nanotube Fibers Spun from Long Carbon-Nanotube Arrays, Small 3(2) (2007) 244-248.

[21] Q.W. Li, X.F. Zhang, R.F. DePaula, L.X. Zheng, Y.H. Zhao, L. Stan, T.G. Holesinger, P.N. Arendt, D.E. Peterson, Y.T. Zhu, Sustained Growth of Ultralong Carbon Nanotube Arrays for Fiber Spinning, Adv. Mater. 18(23) (2006) 3160-3163.

[22] S. Zhang, L. Zhu, M. Minus, H. Chae, S. Jagannathan, C.-P. Wong, J. Kowalik, L. Roberson, S. Kumar, Solid-state spun fibers and yarns from 1-mm long carbon nanotube forests synthesized by water-assisted chemical vapor deposition, J. Mater. Sci. 43(13) (2008) 4356-4362.

[23] F.A. Hill, T.F. Havel, A.J. Hart, C. Livermore, Enhancing the tensile properties of continuous millimeter-scale carbon nanotube fibers by densification, ACS Appl. Mater. Interfaces 5(15) (2013) 7198-207.

[24] X. Zhang, Q. Li, T.G. Holesinger, P.N. Arendt, J. Huang, P.D. Kirven, T.G. Clapp, R.F. DePaula, X. Liao, Y. Zhao, L. Zheng, D.E. Peterson, Y. Zhu, Ultrastrong, Stiff, and Lightweight Carbon-Nanotube Fibers, Adv. Mater. 19(23) (2007) 4198-4201.

[25] W. Cho, M. Schulz, V. Shanov, Growth and characterization of vertically aligned centimeter long CNT arrays, Carbon 72 (2014) 264-273.

[26] A. Ghemes, Y. Minami, J. Muramatsu, M. Okada, H. Mimura, Y. Inoue, Fabrication and mechanical properties of carbon nanotube yarns spun from ultra-long multi-walled carbon nanotube arrays, Carbon 50(12) (2012) 4579-4587.

[27] J. Jia, J. Zhao, G. Xu, J. Di, Z. Yong, Y. Tao, C. Fang, Z. Zhang, X. Zhang, L. Zheng, Q. Li, A comparison of the mechanical properties of fibers spun from different carbon nanotubes, Carbon 49(4) (2011) 1333-1339.

[28] Y. Wei, B. Wang, J. Wu, R. Yang, M.L. Dunn, Bending rigidity and Gaussian

bending stiffness of single-layered graphene, Nano Lett. 13(1) (2013) 26-30.

[29] A. Kozbial, Z. Li, C. Conaway, R. McGinley, S. Dhingra, V. Vahdat, F. Zhou, B. D'Urso, H. Liu, L. Li, Study on the surface energy of graphene by contact angle measurements, Langmuir 30(28) (2014) 8598-606.

[30] B. Alemán, V. Reguero, B. Mas, J.J. Vilatela, Strong Carbon Nanotube Fibers by Drawing Inspiration from Polymer Fiber Spinning, ACS Nano 9(7) (2015) 7392-7398.

[31] K. Koziol, J. Vilatela, A. Moisala, M. Motta, P. Cunniff, M. Sennett, A. Windle, High-Performance Carbon Nanotube Fiber, Science 318(5858) (2007) 1892-1895.

[32] X.-H. Zhong, Y.-L. Li, Y.-K. Liu, X.-H. Qiao, Y. Feng, J. Liang, J. Jin, L. Zhu, F. Hou, J.-Y. Li, Continuous Multilayered Carbon Nanotube Yarns, Adv. Mater. 22(6) (2010) 692-696.

[33] Y. Jung, T. Kim, C.R. Park, Effect of polymer infiltration on structure and properties of carbon nanotube yarns, Carbon 88 (2015) 60-69.

[34] K. Liu, Y. Sun, X. Lin, R. Zhou, J. Wang, S. Fan, K. Jiang, Scratch-Resistant, Highly Conductive, and High-Strength Carbon Nanotube-Based Composite Yarns, ACS Nano 4(10) (2010) 5827-5834.

[35] S. Li, X. Zhang, J. Zhao, F. Meng, G. Xu, Z. Yong, J. Jia, Z. Zhang, Q. Li, Enhancement of carbon nanotube fibres using different solvents and polymers, Compos. Sci. Technol. 72(12) (2012) 1402-1407.

[36] L. Kai, S. Yinghui, Z. Ruifeng, Z. Hanyu, W. Jiaping, L. Liang, F. Shoushan, J. Kaili, Carbon nanotube yarns with high tensile strength made by a twisting and shrinking method, Nanotechnology 21(4) (2010) 045708.

[37] J.N. Wang, X.G. Luo, T. Wu, Y. Chen, High-strength carbon nanotube fibre-like ribbon with high ductility and high electrical conductivity, Nat Commun. 5 (2014) 3848.

[38] G. Hou, G. Wang, Y. Deng, J. Zhang, J.P. Nshimiyimana, X. Chi, X. Hu, W. Chu,

H. Dong, Z. Zhang, L. Liu, L. Sun, Effective enhancement of the mechanical properties of macroscopic single-walled carbon nanotube fibers by pressure treatment, RSC Adv. 6(99) (2016) 97012-97017.

[39] T.Q. Tran, Z. Fan, P. Liu, S.M. Myint, H.M. Duong, Super-strong and highly conductive carbon nanotube ribbons from post-treatment methods, Carbon 99 (2016) 407-415.

[40] W. Xu, Y. Chen, H. Zhan, J.N. Wang, High-Strength Carbon Nanotube Film from Improving Alignment and Densification, Nano Lett. 16(2) (2016) 946-952.

[41] W. Ma, L. Liu, Z. Zhang, R. Yang, G. Liu, T. Zhang, X. An, X. Yi, Y. Ren, Z. Niu, J. Li, H. Dong, W. Zhou, P.M. Ajayan, S. Xie, High-Strength Composite Fibers: Realizing True Potential of Carbon Nanotubes in Polymer Matrix through Continuous Reticulate Architecture and Molecular Level Couplings, Nano Lett. 9(8) (2009) 2855-2861.

[42] M.L. Wu, Y. Chen, L. Zhang, H. Zhan, L. Qiang, J.N. Wang, High-Performance Carbon Nanotube/Polymer Composite Fiber from Layer-by-Layer Deposition, ACS Appl. Mater. Interfaces 8(12) (2016) 8137-8144.

[43] W. keithleyLiu, X. Zhang, G. Xu, P.D. Bradford, X. Wang, H. Zhao, Y. Zhang, Q. Jia, F.-G. Yuan, Q. Li, Y. Qiu, Y. Zhu, Producing superior composites by winding carbon nanotubes onto a mandrel under a poly(vinyl alcohol) spray, Carbon 49(14) (2011) 4786-4791.

[44] S. Boncel, R.M. Sundaram, A.H. Windle, K.K.K. Koziol, Enhancement of the Mechanical Properties of Directly Spun CNT Fibers by Chemical Treatment, ACS Nano 5(12) (2011) 9339-9344.

[45] M. Zu, Q. Li, Y. Zhu, M. Dey, G. Wang, W. Lu, J.M. Deitzel, J.W. Gillespie Jr, J.-H. Byun, T.-W. Chou, The effective interfacial shear strength of carbon nanotube fibers

in an epoxy matrix characterized by a microdroplet test, Carbon 50(3) (2012) 1271-1279.

[46] S. Ryu, Y. Lee, J.-W. Hwang, S. Hong, C. Kim, T.G. Park, H. Lee, S.H. Hong, High-Strength Carbon Nanotube Fibers Fabricated by Infiltration and Curing of Mussel-Inspired Catecholamine Polymer, Adv. Mater. 23(17) (2011) 1971-1975.

[47] T.Q. Tran, Z. Fan, A. Mikhalchan, P. Liu, H.M. Duong, Post-Treatments for Multifunctional Property Enhancement of Carbon Nanotube Fibers from the Floating Catalyst Method, ACS Appl. Mater. Interfaces 8(12) (2016) 7948-7956.

[48] M.G. Hahm, J.-H. Lee, A.H.C. Hart, S.M. Song, J. Nam, H.Y. Jung, D.P. Hashim, B. Li, T.N. Narayanan, C.-D. Park, Y. Zhao, R. Vajtai, Y.A. Kim, T. Hayashi, B.-C. Ku, M. Endo, E. Barrera, Y.J. Jung, E.L. Thomas, P.M. Ajayan, Carbon Nanotube Core Graphitic Shell Hybrid Fibers, ACS Nano 7(12) (2013) 10971-10977.

[49] S. Ryu, J.B. Chou, K. Lee, D. Lee, S.H. Hong, R. Zhao, H. Lee, S.-g. Kim, Direct Insulation-to-Conduction Transformation of Adhesive Catecholamine for Simultaneous Increases of Electrical Conductivity and Mechanical Strength of CNT Fibers, Adv. Mater. 27(21) (2015) 3250-3255.

[50] Y.-M. Choi, H. Choo, H. Yeo, N.-H. You, D.S. Lee, B.-C. Ku, H.C. Kim, P.-H. Bong, Y. Jeong, M. Goh, Chemical Method for Improving Both the Electrical Conductivity and Mechanical Properties of Carbon Nanotube Yarn via Intramolecular Cross-Dehydrogenative Coupling, ACS Appl. Mater. Interfaces 5(16) (2013) 7726-7730.

[51] T.Q. Tran, R.J. Headrick, E.A. Bengio, S. Myo Myint, H. Khoshnevis, V. Jamali, H.M. Duong, M. Pasquali, Purification and Dissolution of Carbon Nanotube Fibers Spun from the Floating Catalyst Method, ACS Appl. Mater. Interfaces 9(42) (2017) 37112-37119.

[52] R.M. Sundaram, A.H. Windle, One-step purification of direct-spun CNT fibers by post-production sonication, Mater. Des. 126 (2017) 85-90.

[53] T.S. Gspann, F.R. Smail, A.H. Windle, FD173: Spinning of carbon nanotube fibres using the floating catalyst high temperature route: purity issues and the critical role of sulphur, Faraday Discuss. 173 (2014) 47-65.

[54] O.-K. Park, H.J. Kim, J.Y. Hwang, S.M. Kim, Y. Jeong, J.K. Lee, B.-C. Ku, Effects of nitrogen doping from pyrolyzed ionic liquid in carbon nanotube fibers: enhanced mechanical and electrical properties, Nanotechnology 26(7) (2015) 075706.

[55] S. Zhang, K.K.K. Koziol, I.A. Kinloch, A.H. Windle, Macroscopic Fibers of Well-Aligned Carbon Nanotubes by Wet Spinning, Small 4(8) (2008) 1217-1222.

[56] A.M. Beese, S. Sarkar, A. Nair, M. Naraghi, Z. An, A. Moravsky, R.O. Loutfy, M.J. Buehler, S.T. Nguyen, H.D. Espinosa, Bio-Inspired Carbon Nanotube–Polymer Composite Yarns with Hydrogen Bond-Mediated Lateral Interactions, ACS Nano 7(4) (2013) 3434-3446.

[57] M. Naraghi, G.H. Bratzel, T. Filleter, Z. An, X. Wei, S.T. Nguyen, M.J. Buehler, H.D. Espinosa, Atomistic Investigation of Load Transfer Between DWNT Bundles "Crosslinked" by PMMA Oligomers, Adv. Funct. Mater. 23(15) (2013) 1883-1892.

[58] C.F. Cornwell, C.R. Welch, Very-high-strength (60-GPa) carbon nanotube fiber design based on molecular dynamics simulations, J. Chem. Phys. 134(20) (2011) 204708.

[59] T. Filleter, R. Bernal, S. Li, H.D. Espinosa, Ultrahigh Strength and Stiffness in Cross-Linked Hierarchical Carbon Nanotube Bundles, Adv. Mater. 23(25) (2011) 2855-2860.

[60] Y.-O. Im, S.-H. Lee, T. Kim, J. Park, J. Lee, K.-H. Lee, Utilization of carboxylic functional groups generated during purification of carbon nanotube fiber for its strength improvement, Appl. Surf. Sci. 392 (2017) 342-349.

[61] O.-K. Park, H. Choi, H. Jeong, Y. Jung, J. Yu, J.K. Lee, J.Y. Hwang, S.M. Kim, Y. Jeong, C.R. Park, M. Endo, B.-C. Ku, High-modulus and strength carbon nanotube fibers

using molecular cross-linking, Carbon 118 (2017) 413-421.

[62] J. Min, J.Y. Cai, M. Sridhar, C.D. Easton, T. R. Gengenbach, J. McDonnell, W. Humphries, S. Lucas, High performance carbon nanotube spun yarns from a crosslinked network, Carbon 52 (2013) 520-527.

[63] N.P. O'Brien, M.A. McCarthy, W.A. Curtin, Improved inter-tube coupling in CNT bundles through carbon ion irradiation, Carbon 51 (2013) 173-184.

Part II. Maximization of tensile strength of carbon nanotube yarn

Chapter 2 Theoretical Consideration for High Tensile Strength of CNTY

2.0 Major symbols

n: *Number of walls of CNT*

τ: *Interfacial shear strength (MPa)*

σ_{CNTY}: *Specific strength of CNTY $(N/tex, GPa/(g \cdot cm^{-3}))$*

D_G: *Bending rigidity of graphene (J)*

D_n: *Bending rigidity of CNT with n walls (J)*

γ: *Surface energy of CNT (J/m^2)*

R_i: *Radius to i^{th} wall of CNT (m)*

r_i: *Radius of curvature to i^{th} wall of CNT (m)*

L_{CNT}: *Length of CNT (m)*

L_{eb}: *Length of elementary bundle (m)*

N: *Number of CNT layer in microbundle*

N': *Number of microbundle layer in macrobundle*

α: *Radius ratio of microbundle to CNT*

β: *Radius ratio of macrobundle to microbundle*

Ω_{CNT}: *Area fraction of CNT in contact with neighboring CNTs*

Ω_{eb}: *Area fraction of elementary bundle in contact* with neighboring bundles

d_0: *Diameter of microbundle*

D: *Diameter of CNTY*

d: *Diameter of macrobundle*

$d + \Delta d$: *Diameter of arbitrary CNT domain*

N_{domain}: *number of domain*

A_{total}: *cross sectional area of CNTY*

A_{CNT}: *cross sectional area of CNTs in CNTY*

A_{eff}: *effective cross sectional area*

m: *Weibull modulus, shape factor*

2.1   Theoretical consideration relevant to CNTY strength

There has been remarkable progress with regard to the fabrication of yarns based on high-performance CNTs. However, the theoretically predicted tensile strength of CNTs has yet to be realized in practical CNTYs. Although equation (1.1) and (1.2) is commonly used to predict the CNTY strength [1-3] and it suggests that the longer and thinner the elementary CNTs are the stronger the CNTY would be, this equation does not appear to be feasible when applied to a practical CNTY due to several factors. The most significant factor is the dimensional difference [4-6]. Indeed, in the equation, the elementary fibers with micron-sized diameters and lengths were considered as non-deformable cylinders of a uniformly specific volume with a circular cross-section, whereas actual CNTs with nanometer-sized diameter and length of a few tens of microns are deformable. Due to the dimensional difference, two factors are needed to be reconsidered; first, the structural hierarchy of CNTY and second, actual load bearing element.

Thus, to overcome the limitation of current equations, we developed a new theoretical approach which considered that the failure of CNTYs is governed by pull-out of load bearing element due to the weak interaction between CNTs and unique hierarchical structure of CNTY with the goal of finding rational routes based on fundamental theories to improve the tensile strength further and thus hopefully realize the theoretical tensile performance of CNTYs.

2.2 Modeling of CNTY structure

Many researchers attempted to develop CNTY model in order to predict the strength of yarn-like CNT fibers and explain the deformation behavior of CNTYs. Although they provided a helpful suggestion for favorable nanostructure of component CNTs to improve CNTY strength, the models showed the limitation to describe the strength of CNT bundle rather than the strength of CNTY. In general, smaller bundles are theoretically considered to take advantages for better CNTY strength but the most common empirical way of CNTY strengthening such as densification and compaction of CNTYs, that means bigger bundle makes stronger CNTYs implies contradictory results with theoretical suggestion. Thus, the hierarchical level of CNTY structure was tried to more properly described in this study unlike the previous simple model of hierarchical structure with three level, CNT-bundle-yarn, in order to resolve the contradiction between theoretical and empirical results.

The aim of CNTY structure modeling is to determine failure point, where mainly slippage occurs, and provide the guidelines for CNTY strengthening. Most natural fibers, such as cellulose fiber, consist of a four-level hierarchy of polymer (~2 nm) – microfibril (7~8 nm) – macrofibril (400 nm) - fibers as shown in Fig. 2.1. Previous studies have revealed the key mechanistic principle of such fiber and the strengthening role of microfibril, which is the load-bearing element. In this respect, mimicking the concept of natural fiber inspires a new approach toward the hierarchy of CNT yarn (Fig. 2.2). The balance between stabilization energy of the CNTs assembled in a bundle and van der Waals interaction of CNTs result in distinctive nanostructure, a primary CNT bundle, which named elementary bundle in this study. Every elementary CNT bundles in Fig. 2.3a is concentrated in form of reticulated structure considered as a secondary bundle.

43

Therefore, we classified the secondary bundle into three stages: CNT micro, meso and macrobundle (Fig. 2.3b). Since CNT nano-assemblies have been reported to have high strength, we regarded elementary bundle as the smallest load-bearing unit, indicating that load transfer occurs starts from slippage between secondary bundles and ends in form of slippage of CNT elementary bundles in the secondary bundle, which looks like brittle failure in macroscopic view.
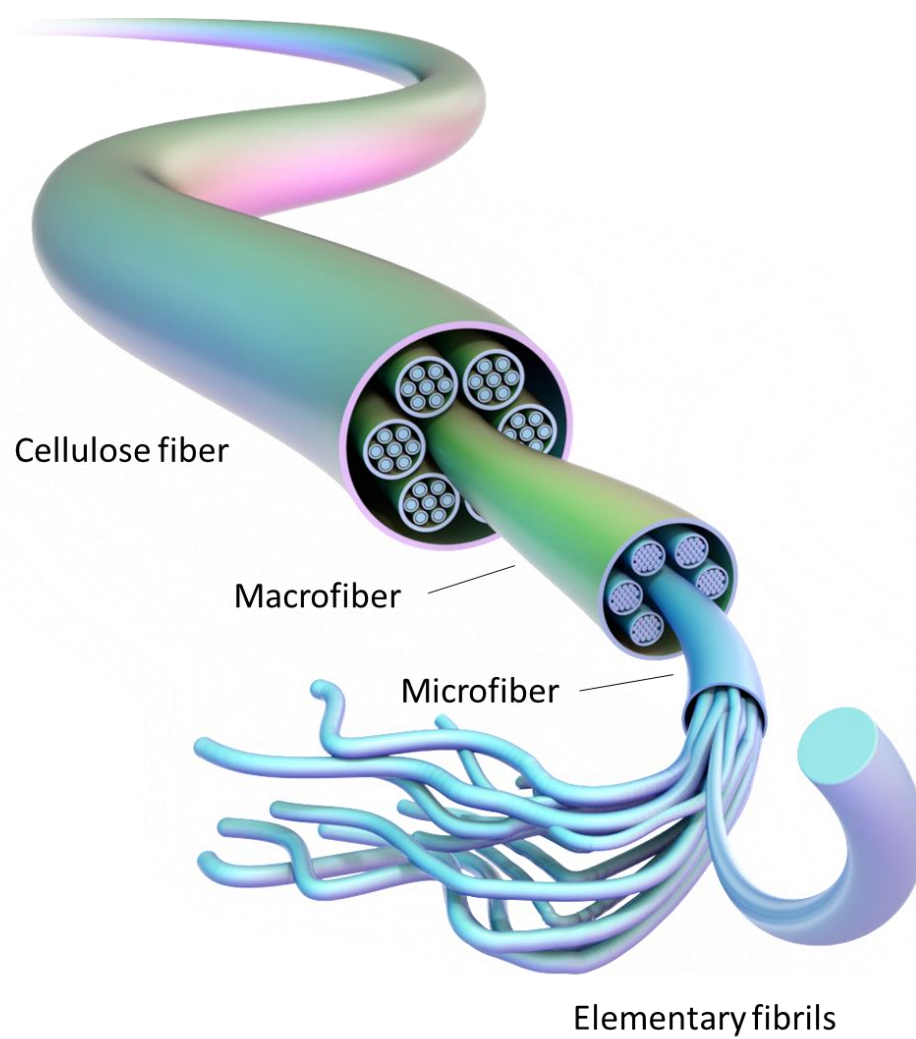
Fig. 2.1. Hierarchical structure of cellulose fiber.
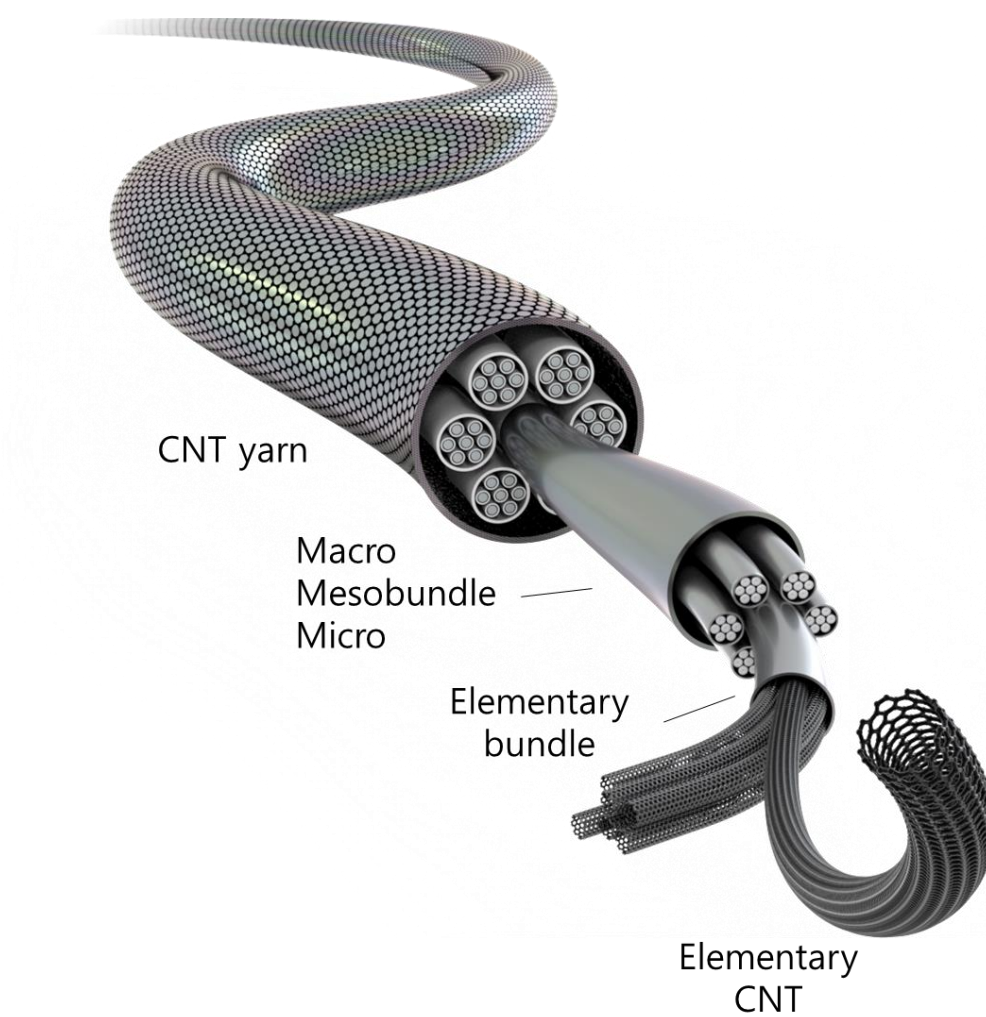
Fig. 2.2. Proposed hierarchical structure of CNTY.
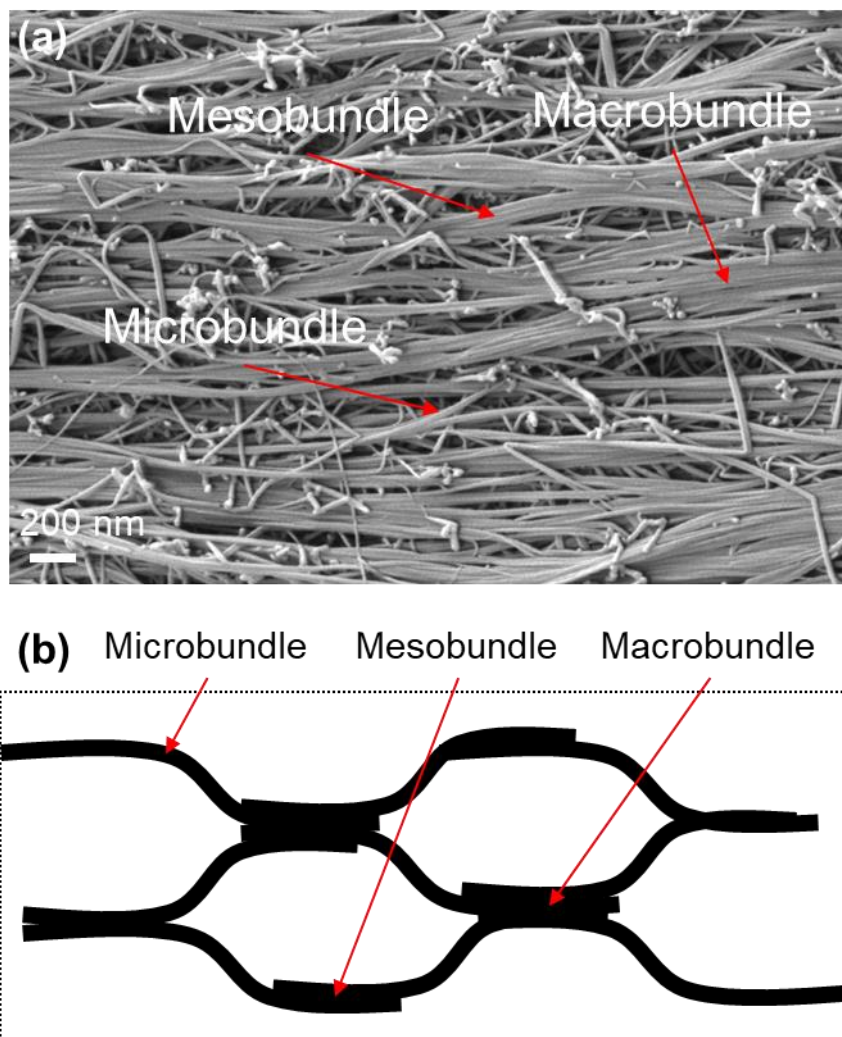
Fig. 2.3. (a) SEM image of as-prepared CNTY and (b) simple model of the hierarchical structure of CNT secondary bundle.

The failure section analysis of the CNTY was performed to identify the unit of the load-bearing element. Fig. 2.4a shows the SEM micrograph of a fracture section of CNTY. According to previous reports, the CNTY fails through slippage between CNTs or bundles. However, the fractography shown in Fig. 2.4a depicts the appearance of a ruptured CNT bundle. An additional analysis was performed at high magnification with the results shown in Fig. 2.4b-e. CNT bundles with a diameter of around 30 nm were found at most ends of the failure section. Since no CNT assembly structures with smaller diameters or individual CNTs were found at the fracture ends, the nanofibrillar bundle was identified to be a primary structure formed by a strong intertube interactions between in-situ growing CNTs. These results show that the load-bearing element is not a simple bundle or individual CNT, but an elementary bundle mentioned previously. CNTY failure occurs due to slippage between the elementary bundles, which has been appeared as a rupture of the CNT bundle from a macroscopic point of view.

Further, the bundle around brittle mode of CNTY shows diameter around 2-300 nm, whereas the bundle far from failure shows diameter over 500 nm as shown in Fig. 2.4a. Such result indicates the secondary bundles should also be classified according to diameter. Therefore, first, we defined elementary bundle according to nanomechanics with stabilization energy, and then classified secondary bundle according to classical mechanics such as Griffith theory. The theoretical consideration supported that CNTY has somehow a four-stage hierarchy of CNT-elementary bundle-secondary bundle-yarn, which is apparently very similar to the structural characteristics of cellulose fibers with the hierarchy of molecular chain-microfibril-macrofibril-cellulose fibers.
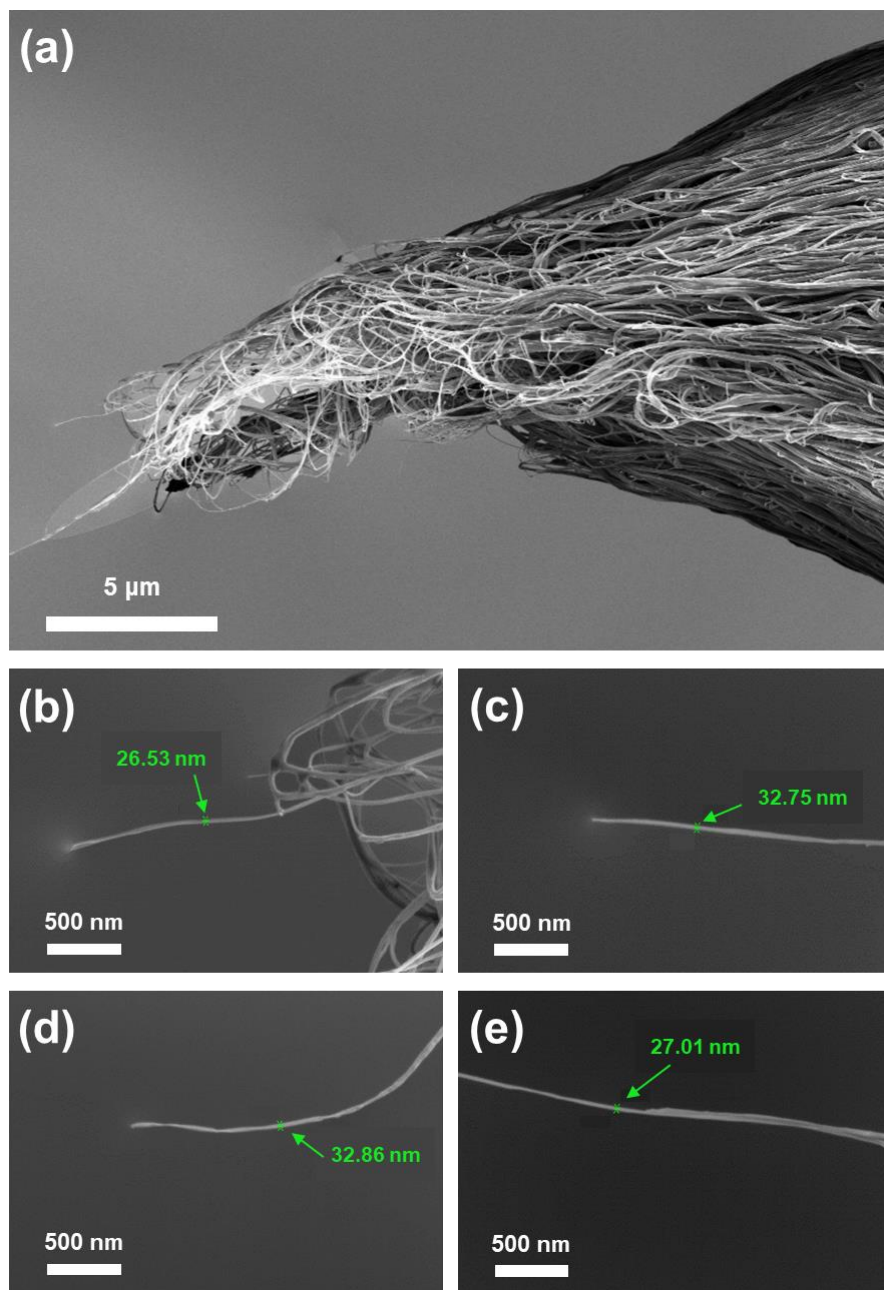
Fig. 2.4. SEM images of (a) a fracture section of as spun CNTY and (b-e) elementary bundles at the end of the fracture section.

In order to determine the size of elementary bundle, prediction through simplified modeling is required. The model of CNT bundle can be simplified into the fiber composed of a collection of parallel, rigid rods that can slide with respect to each other. However, considering the circular cross-section of CNTs, it is overestimating the total shear force because it is impossible for all surface area to be in contact each other so the fraction of tube surface area in contact should be considered to estimate precisely the specific strength of CNTYs. Hollow cylindrical structure of the nanotube allows it to be easily deformed in the radial direction rather than classical fibers. Through hexagonal packing model, Vilatela et al. [4] derived the proportion of CNT surface area in contact with neighboring CNTs, Ω, as expressed total energy of tubes per length with surface energy and curvature energy for non-contact area for round tubes and deformed tubes as shown in Fig. 2.5. The curvature energy is expressed as bending energy of graphene. Therefore, the total energy of deformed CNTs per unit length is given as equation (2.1).

$$E_{CNT} = 2\pi R_n \gamma (1 - \Omega) + D_n \times \sum_{i=1}^{n} \frac{2\pi R_n (1 - \Omega)}{2r_n^2} \qquad (2.1)$$

Also, the fraction of perimeter in contact can be expressed as follows:

$$\Omega = 1 - \frac{r_n}{R_n} \qquad (2.2)$$

where r is the radius of curvature.

Combining equations (2.1) and (2.2) leads to fraction value Ω_{CNT} as follows.

$$\Omega_{CNT} = 1 - \sqrt{\frac{D_n}{2\gamma R_n} \times \sum \frac{1}{R_i}} \left(\frac{dE_{CNT}}{d\Omega} = 0 \ when \ \Omega = \Omega_{CNT}\right) \tag{2.3}$$

Equation (2.3) implies that the fraction value Ω_{CNT} also relies on structural parameters, outer diameter and a number of walls because the surface energy and bending rigidity can be taken as constant values.

On the other hand, the total energy of undeformed CNTs per unit length is given as equation (2.4).

$$E_{CNT,0} = 2\pi R_n \gamma + D_n \times \sum_{i=1}^{n} \frac{2\pi R_i}{2R_i^2} \tag{2.4}$$

The stabilization energy of CNTs is the driving force in which isolated CNTs are gathered and hexagonally packed, expressed as the energy difference between the packed CNTs and the isolated CNTs from equation (2.1) and (2.4), respectively. The energy per unit length can be obtained by combining equations (2.1), (2.3) and (2.4) as follows.

$$\Delta E_{stab} = E_{CNT} - E_{CNT,0} = -2\pi \left[\sqrt{R_n \gamma} - \sqrt{D_n \times \sum_{i=1}^{n} \frac{1}{2R_i}}\right]^2 \tag{2.5}$$

Since Ω_{CNT} is positive fraction value, hexagonal packing model is applicable only when outer radius of CNT is large enough. Within a certain range of radius, Fig. 2.6 is presenting the stabilization energy against structural parameters of nanotubes taking surface energy (γ) and bending rigidity (D_G) as 0.0597 J/m^2 and 2.11 x 10^{-19} J respectively from the reference [7, 8]. For all CNTs with various number of walls, the stabilization energy from radial deformability of CNT gets larger as the radius of CNT increases.
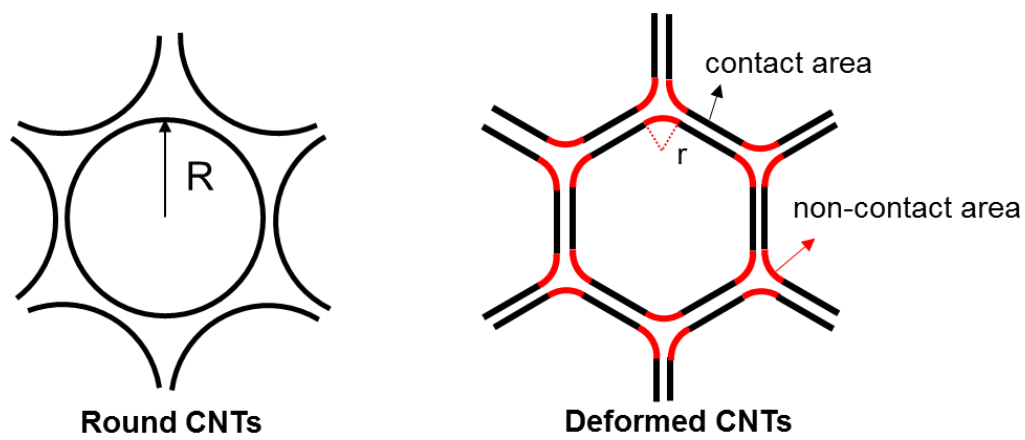
Fig. 2.5. Schematic of before and after radial deformation of CNTs.
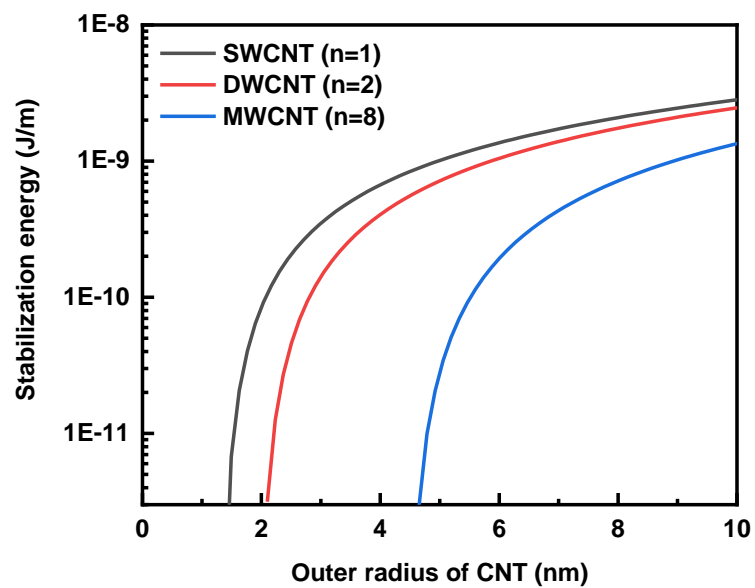
Fig. 2.6. Stabilization energy of hexagonally packed CNTs according to outer radius and number of walls.

Since the stabilization energy is always negative, if this energy is the only driving factor of the CNT assembly, the CNT bundle must be boundlessly large. However, since the results are different from actual reports, it can be seen that there is another driving factor in the formation of CNT assembly, that is, the van der Waals interaction between CNTs. Accordingly, the size of microfibril in cellulose fiber is determined by the equilibrium of hydrogen bonds and van der Waals force between molecules. At this juncture, the balance between stabilization energy of the CNTs assembled in a bundle and van der Waals interaction of CNTs result in distinctive nanostructure, the CNT elementary bundle.

In order to calculate the stabilization energy of CNT assembly, the model of CNT assembly is required. By hexagonal packing, the model is simply derived as function of CNT layers (N) as shown in Fig. 2.7. At given N, the total number of CNTs in the assembly is $3N^2-3N+1$, while the number of inner and outer CNTs are $3(N-1)^2$ and $3N-2$, respectively. Since stabilization only occurs on the inner CNTs, the grey area of Fig 2.6, the total stabilization energy is expressed as $3(N-1)^2\times\Delta E_{stab}$.
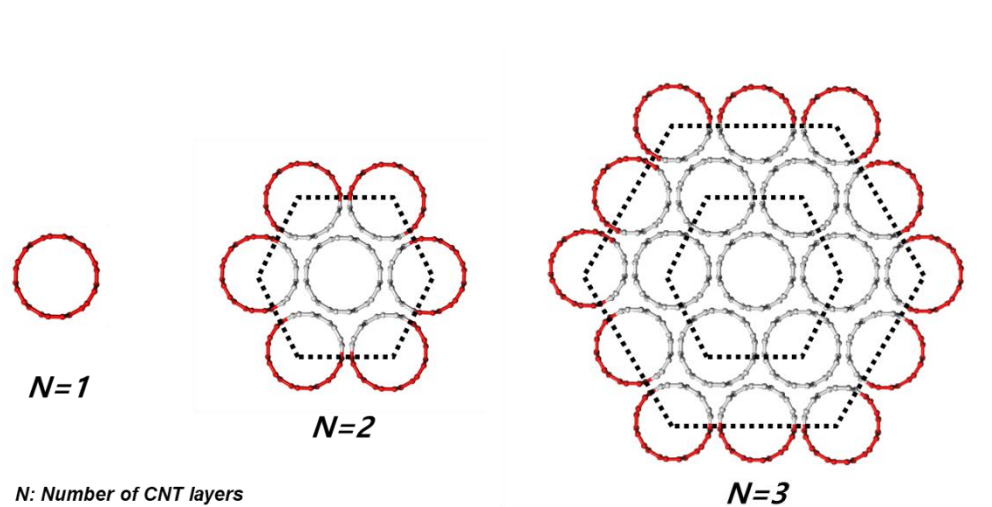
Fig. 2.7. Schematic image of hexagonal close-packed CNT assembly based on number of CNT layers.

The cohesive energy of CNTs from van der Waals interaction is also determined by structural factors of CNT such as outer radius and number of walls. With simulation and derivation from Lennard-Jones potential, Girifalco et al. [9] found out that cohesive energy of SWCNT is linear function of square root of radius of CNT. On the other hand, Zhao et al. [10] reported that cohesive energy of MWCNT is function of radius of CNT and number of walls. Combining both reports, the cohesive energy of CNT is given as equation (2.6)

$$\Delta E_{coh}(J/m) \approx -[0.5773 \times R_n(nm) - 0.0149] \times \sum_{i=1}^{n} \frac{R_n}{R_i} \times 10^{-9} \qquad (2.6)$$

Based on equation (2.6), Fig. 2.8 is presenting the cohesive energy against structural factors of nanotubes. For all CNTs with various number of walls, the cohesive energy of CNT gets larger as the radius of CNT increases.
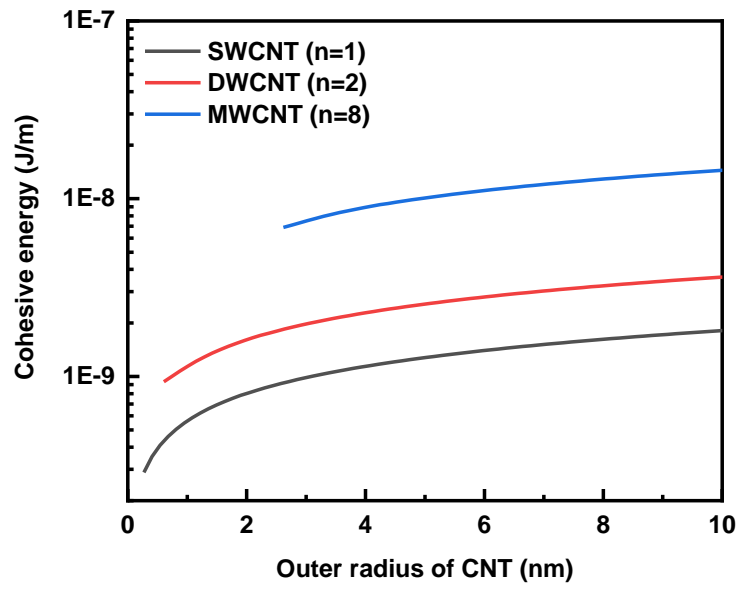
Fig. 2.8. Cohesive energy between CNTs according to outer radius and number of walls.

The balance between the stabilization energy of assembly and cohesive energy between CNTs occurs at number of CNT layers in elementary bundle. Through combining equation (2.5), (2.6) and the hexagonal model, the number of CNT layers is expressed as equation (2.7)

$$N = 1 + \sqrt{\frac{\Delta E_{coh}}{3\Delta E_{stab}}} \tag{2.7}$$

Also, the diameter of elementary bundle is expressed as $(2N\text{-}1)\times 2R_n$ or $2\alpha R_n$, where α indicates the radius ratio of elementary bundle to CNT, calculated as $2N\text{-}1$. Fig. 2.9 and 2.9 are presenting the number of CNT layers in elementary bundle and the diameter of elementary bundle against structural factors of nanotubes, respectively.

Since DWCNT which we experimentally used has a radius of 2.8 nm, the calculation was performed for a given CNT. The elementary bundle is composed of 3.6 layers of CNT, resulting elementary bundle with diameter of 34 nm. Such value well matches with the diameter of elementary bundle shown in Fig. 2.4., indicating model of elementary bundle is well-defined.
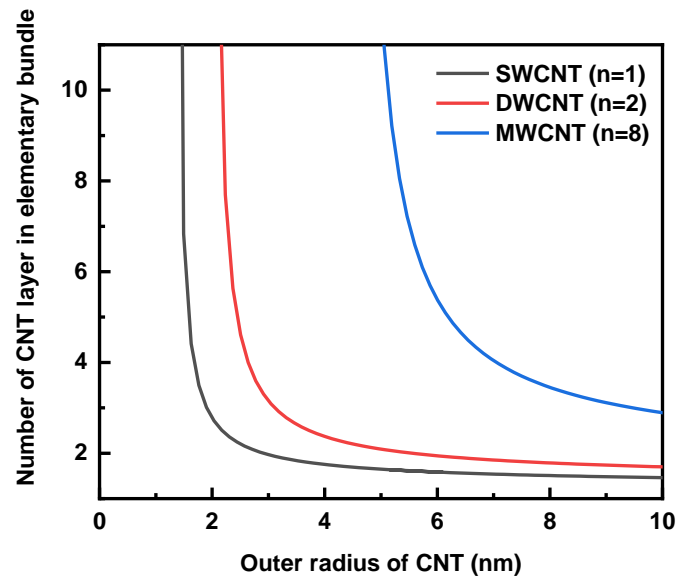
Fig. 2.9. Number of CNT layers in elementary bundle according to outer radius and number of walls of CNT.
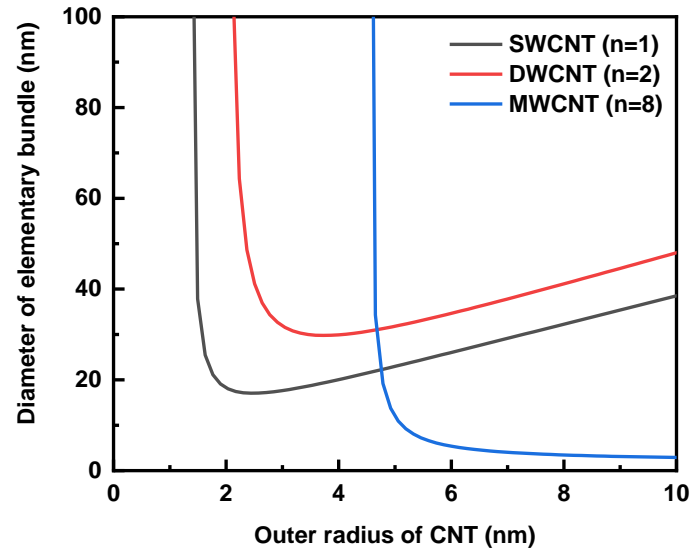
Fig. 2.10. Diameter of elementary bundle according to outer radius and number of walls of CNT.

2.3 Estimating CNTY strength

2.3.1 Strength function of CNTY in term of elementary bundle

CNTY has unique hierarchical structure. CNTYs are composed of elementary bundles and secondary bundles of CNTs. We assumed that load bearing mechanism of CNTY is based on slippage between elementary bundles with high strength comparable to CNT. As Vilatela et al. [4] reported that the strength of CNT bundle is function of length, surface fraction, interfacial shear strength and the number of CNT, we revisited the strength of CNTY (σ_{CNTY}) as a function of secondary bundle based on four factors of elementary bundle as equation (2.8),

$$\sigma_{CNTY} = f_{sb}(t_{eb}, L_{eb}, \Omega_{eb}, \tau_{eb}) \qquad (2.8)$$

where t_{eb}, L_{eb}, Ω_{eb} and τ_{eb} are number fraction in contact, length, surface area fraction in contact and interfacial shear strength of elementary bundle, respectively.

2.3.2 Number fraction of elementary bundle in contact

As we already know that the load-bearing mechanism of CNTY is based on the slippage between the load-bearing elements, the elementary bundles, the strength of CNTY would be proportional to the area where the elements are in contact with each other. To estimate the strength of CNTY, we considered a hexagonal array of load-bearing element similar to CNT assembly in Fig. 2.7. Only the inner area excludes the area in the perimeter of the array and contributes to the strength of CNTY. The specific strength, which represents the load over the linear density, will be proportional to the

ratio of the aforementioned region to the entire region of the array. This number ratio is also expressed as the load-bearing ratio (t_{eb}), which can be expressed as the number of elementary bundle layers in the secondary bundle (N_{eb}) as equation (2.9).

$$t = 1 - \frac{3N_{eb} - 2}{3N_{eb}^2 - 3N_{eb} + 1} \tag{2.9}$$

The dependency of the number fraction of elementary bundle in contact on the number of elementary bundle layers of assembly is shown in Fig. 2.11. When load-bearing elements are stacked in layers of five, 80% of the theoretically achievable strength can be reached. The diameter of secondary bundle recorded in previous report is around 50 nm based on CNTYs with specific strength around 1~2 N/tex [11]. If the load-bearing element had individual CNT, the number of layer is about 7 and reaches 90% of the maximum theoretical strength. However, previous reports with the strength of more than 3 N/tex [12-14] show that the load-bearing element cannot mathematically be an individual CNT. It should be noteworthy at this juncture that the results are mathematically well matched when the element is assumed to be elementary bundle.
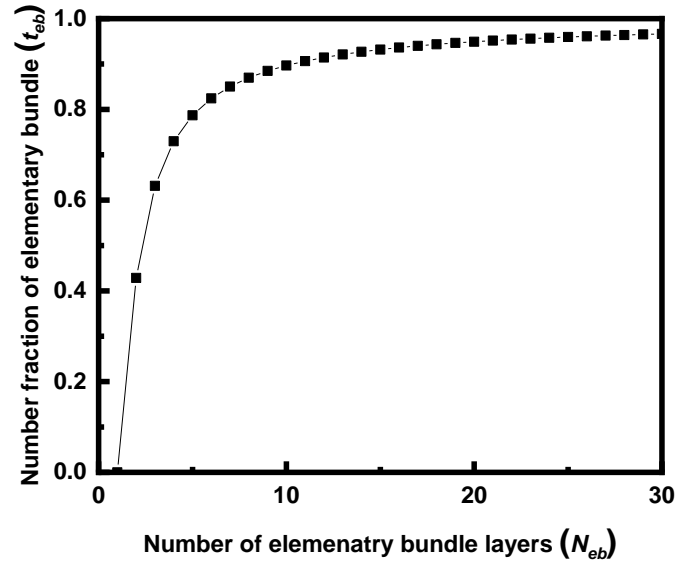
Fig. 2.11. Dependency of number fraction contacting each other in CNT assembly on a total number of CNTs in assembly.

As the packing density of CNTs in CNTY increases, it becomes difficult to determine the size of the secondary bundle. Therefore, t_{eb} must be expressed as a new factor. Defining the new factor β (= $2N_{eb}$-1) as the radius ratio of elementary bundle to secondary bundle, the load bearing ratio can be summarized and approximated as equation (2.10).

$$t = 1 - \frac{3N_{eb} - 2}{3N_{eb}^2 - 3N_{eb} + 1} = 1 - \frac{6\beta - 2}{3\beta^2 + 1} \approx \left(1 - \frac{1}{\beta}\right)^2 \qquad (2.10)$$

When CNTY is divided into arbitrary sections as a domain, the domain is composed of CNT elementary bundles and void (Fig. 2.12a). The area of CNTY cross section (A_{total}) can be expressed as the sum of these domain areas as equation (2.11),

$$A_{total} = \frac{1}{4}\pi D^2 = N_{domain} \times \frac{1}{4}\pi(d + \Delta d)^2 \qquad (2.11)$$

where D, d, $d+\Delta d$ and N_{domain} are diameter of CNTY, secondary bundle, domain and the number of CNT domain, respectively. In order to obtain the area of CNT (A_{CNT}) in the domain, a secondary bundle is rearranged by combining the elementary bundles that exist inside, represented as in Fig. 2.12b. Since the diameter of domain decreases by Δd and the number of domains is maintained, A_{CNT} is expressed as equation (2.12).

$$A_{CNT} = N_{domain} \times \frac{1}{4}\pi d^2 \tag{2.12}$$

The effective area ratio (A_{eff}), which indicates the ratio of the area occupied by CNTs in the entire cross section is defined as A_{CNT}/A_{total}. Substituting equation (2.11) and (2.12) into A_{eff} and introducing an approximation results equation (2.13) in a form similar to equation (2.10).

$$A_{eff} = \left(1 + \frac{\Delta d}{d}\right)^{-2} = \left(1 + \frac{\Delta d}{\beta d_0}\right)^{-2} \approx \left\{\left(1 - \frac{1}{\beta}\right)^2\right\}^{\Delta d/d_0} \tag{2.13}$$

where d_0 is the diameter of elementary bundle. In summary, the strength of CNTY is function of the effective area ratio as shown in equation (2.11).

$$\sigma_{CNTY} \propto t_{eb} \approx \left(A_{eff}\right)^{d_0/\Delta d} \tag{2.13}$$

The higher packing density of elementary bundle or larger secondary bundle leads to higher mechanical properties of CNTY by fully utilizing surface for load-bearing.
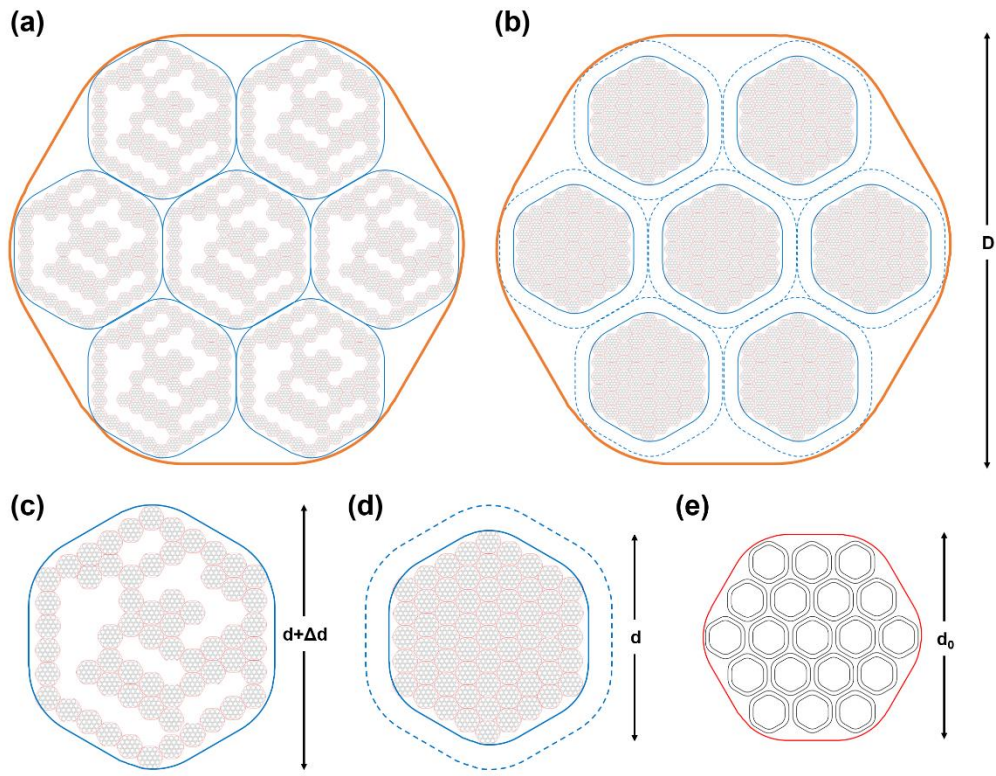
Fig. 2.12. Schematic cross-sectional image of (a) CNTY with domains (b) CNTY with rearranged domains (c) CNT domain (d) CNT secondary bundle (rearranged domain) and (e) CNT elementary bundle.

2.3.3 Length of elementary bundle

From classical mechanics, we already know that the strength of yarn is function of length of fiber. Among theories reported to date, the weakest link theory based on the Weibull model is known to best establish the relation between yarn strength and fiber length [15]. The model is based on fragmentation model, which is based on multiple breakage of fiber. To be specific, the yarn breaks when the average length of fiber (l_f) gets lower than the critical length (l_c) as shown in Fig. 2.13. Though the model is applicable to three-tiered hierarchy of fiber-bundle-yarn, with reinterpretation based on elementary bundle, the model is applicable to CNTY with four-tiered hierarchy of CNT-elementary bundle-secondary bundle-CNTY.

According to Weibull model, the probability (P) of yarn failure at given tensile load (σ) is described as equation (2.14),

$$P(\sigma) = 1 - exp\left\{-\left(\frac{\sigma}{\sigma_s}\right)^m\right\} \qquad (2.14)$$

where σ_s is scale factor and m is shape factor. The shape factor describes the dispersion of fiber strength along a fiber length. In general, if the shape factor is 2~4, the fiber is known as brittle material, whereas if the shape factor is 20, the fiber is known as ductile and uniform material. Since CNT belongs to the latter, it can be it can be easily inferred that the shape factor of CNTY is around 20.

The strength ratio of bundle and fiber is expressed by the Coleman factor (Ψ), which is function of shape factor. Applying fiber to CNT and bundle to elementary bundle, the strength ratio of CNT (σ_{CNT}) to elementary bundle (σ_{eb}) is expressed as equation (2.15).

$$\frac{\sigma_{CNT}}{\sigma_{mib}} = \Psi = m^{1/m} e^{1/m} \Gamma\left(1 + \frac{1}{m}\right) \tag{2.15}$$

Fig. 2.14 is presenting the Coleman factor against shape factor. For ductile materials, the Coleman factor converge to 1, indicating the strength of elementary bundle is comparable to the strength of CNT. Since elementary bundle can be assumed as unbreakable fibril, the hierarchy of CNTY applied to Weibull model is should be considered as elementary bundle-secondary bundle-CNTY (three-tiered hierarchy).

Applying secondary bundle to bundle of Weibull model, the strength ratio of yarn to bundle is calculated as that of CNTY to secondary bundle (σ_{sb}). The ratio is expressed as equation (2.16),

$$\frac{\sigma_{CNTY}}{\sigma_{sb}} = \left(\frac{L_{eb}}{L_c}\right)^{1/m} V_f \eta_q \tag{2.16}$$

where L_{eb}, L_c, V_f and η_q are length of elementary bundle, critical length, volume fraction of elementary bundle and orientation factor, respectively. Since t_{eb} is the strength ratio of secondary bundle to elementary bundle, the strength of CNTY is expressed as

equation (2.17),

$$\sigma_{CNTY} \propto \left(\frac{L_{eb}}{L_c}\right)^{1/m} \left(A_{eff}\right)^{d_0/\Delta d} \tag{2.17}$$

The formula contains both the bundling property and the length property. According to equation (2.17), the strength of CNTY can be increased by dense packing of longer elementary bundle.
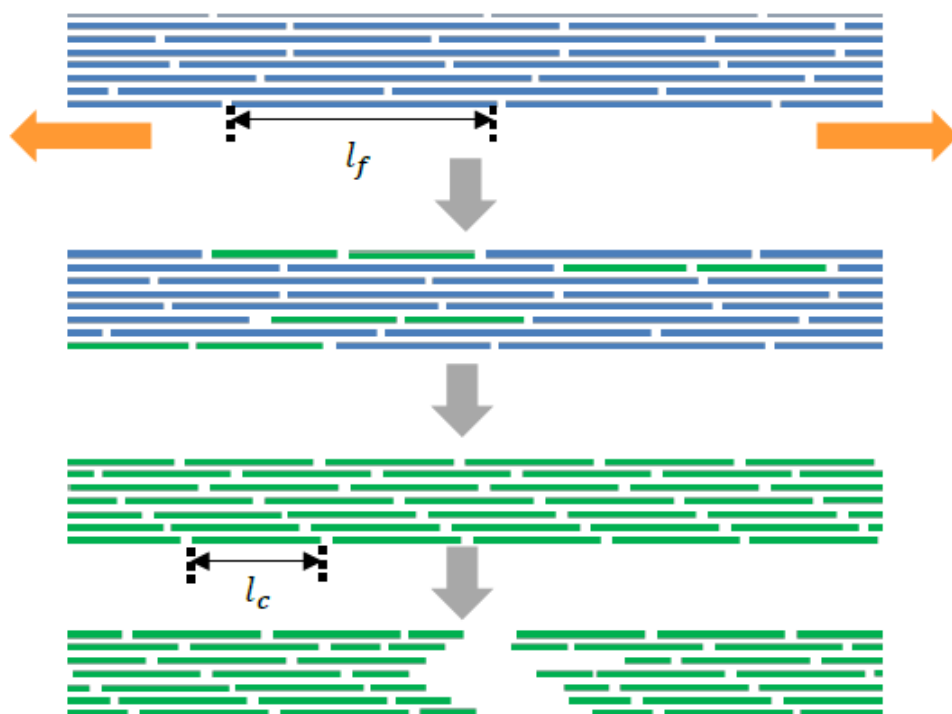
Fig. 2.13. Schematic image of model of fragmentation mechanism.
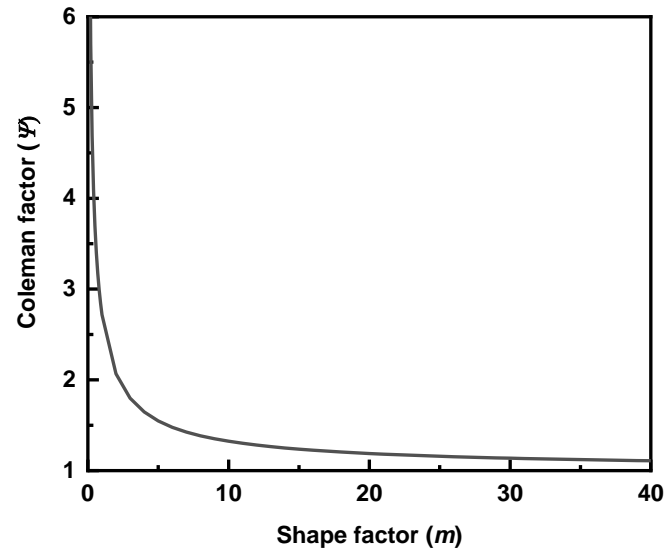
Fig. 2.14. Dependency of Coleman factor on shape factor.

2.3.4 Surface area fraction of elementary bundle

It was confirmed through the Weibull model that the elementary bundle is as high as CNT in strength, so the elementary bundle can be assumed to be one huge imaginary MWCNT. Assuming that the layer of CNT is a wall of MWCNT shown in Fig. 2.15, the energy of the elementary bundle can be inferred by modifying the equation suggested by vilatela et al. as shown in equation (2.17),

$$E_{eb} = 2\pi R_n(3N-2)\gamma(1-\Omega) \ + 2\pi D_n \times \sum_{j=1}^{N} \frac{1}{2(2j-1)R_n(1-\Omega)}$$

$$\approx 2\pi R_n(3N-2)\gamma(1-\Omega) + 2\pi D_n \times \int_{1}^{N} \frac{dj}{2(2j-1)R_n(1-\Omega)}$$

$$(2.17)$$

where D_n is bending rigidity of CNT in elementary bundle. The surface energy of elementary bundle is described as total surface energy of outer CNT in elementary bundle. For curvature energy, the term R_i is rescaled as $(2i\text{-}1)R_n$ whereas bending rigidity of graphene is replaced by that of CNT since the actual wall of imaginary MWCNT is composed of CNT. Pantano et al. [16, 17] derived D_n as a function of structural factors of CNT such as number of walls and innermost radius, described as equation (2.18). In the case of N obtained earlier, it is mainly calculated in a non-integer form, which is difficult to substitute into the sigma function. Therefore, the curvature energy was approximated in an integral form. As a result, the surface area fraction (Ω_{eb}) of elementary bundle is expressed as equation (2.19).

$$D_n \approx D_G \times n \times \left[1 + \frac{3(n-1)}{2} \left(\frac{0.335 \, nm}{R_1} \right) \right.$$

$$+ \frac{(n-1)(2n-1)}{2} \left(\frac{0.335 \, nm}{R_1} \right)^2 \tag{2.18}$$

$$\left. + \frac{n(n-1)^2}{4} \left(\frac{0.335 \, nm}{R_1} \right)^3 \right]$$

$$\Omega_{eb} = 1 - \sqrt{\frac{D_n}{2\gamma R_n^2} \times \frac{ln(2N-1)}{3N-2}} = 1 - \sqrt{\frac{D_n}{2\gamma R_n^2} \times \frac{2 \, ln \, \alpha}{3\alpha-1}} \tag{2.19}$$

$$\left(\frac{dE}{d\Omega} = 0 \ when \ \Omega = \Omega_{eb} \right)$$

Based on equation (2.18) and (2.19), Fig. 2.16 is presenting the surface fraction of elementary bundle in contact against structural factors of nanotubes. For all CNTs with various number of walls, the radial deformability of elementary bundle gets larger as the radius of CNT increases. Combining equation (2.17) with Ω_{eb}, the strength of CNTY is expressed as equation (2.20).

$$\sigma_{CNTY} \propto \Omega_{eb} \left(\frac{L_{eb}}{L_c} \right)^{1/m} \left(A_{eff} \right)^{d_0/\Delta d} \tag{2.20}$$

The formula additionally contains the property of surface area of elementary bundle. According to equation (2.20), the strength of CNTY can be increased by using CNT with less number of wall and large outer radius.
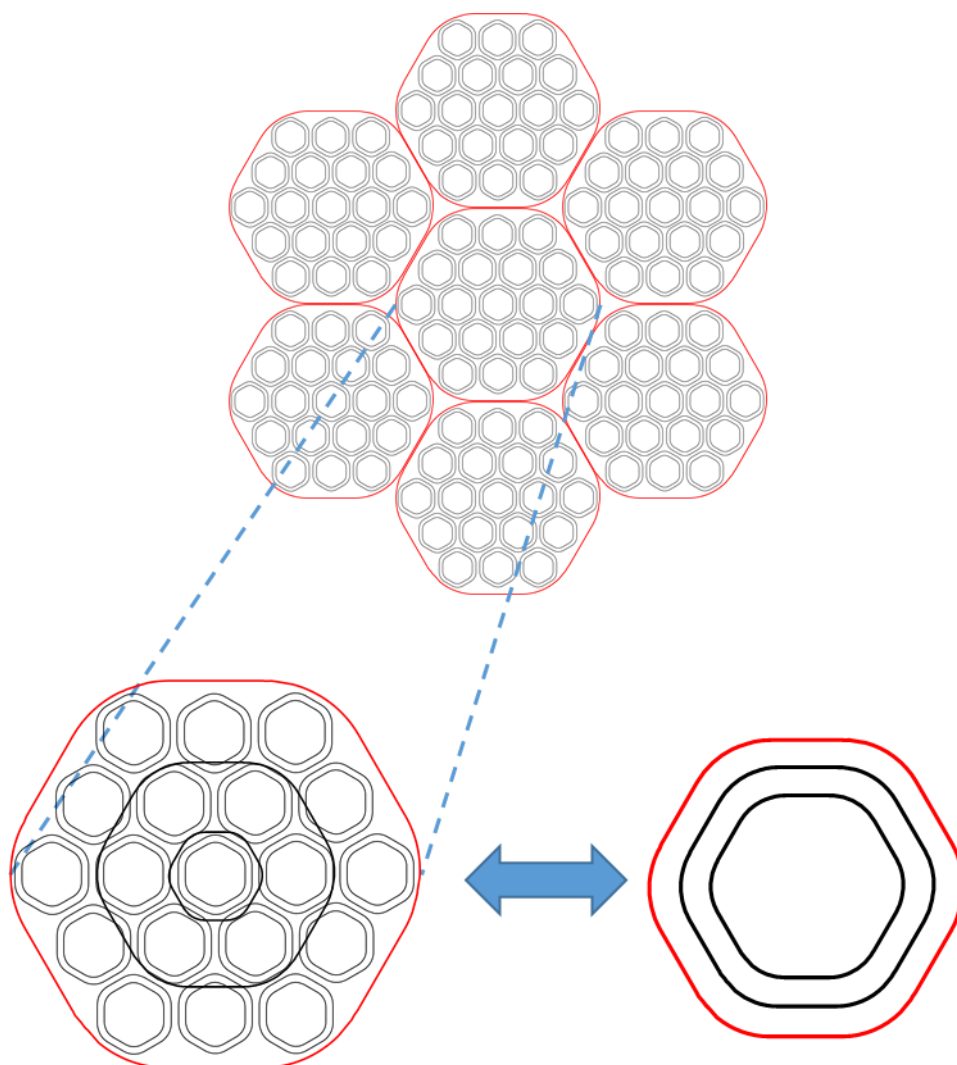
Fig. 2.15. Schematic image of elementary bundle assuming as single huge imaginary MWCNT.
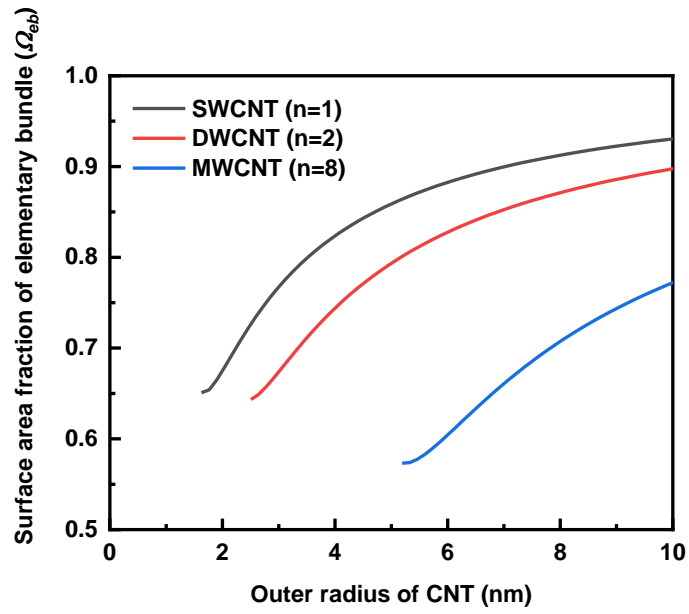
Fig. 2.16. Surface area fraction of elementary bundle in contact according to outer radius and number of walls of CNT.

2.3.5 Interfacial shear strength of elementary bundle

It is well known through the classical mechanics that the strength of yarn is proportional to interfacial shear strength of load-bearing element due to slippage of the element. At this juncture, it can be inferred that the strength of CNTY is proportional to the interfacial shear strength of elementary bundle as shown in equation (2.21), where k is proportional constant.

$$\sigma_{CNTY} = k\Omega_{eb}\tau_{eb}\left(\frac{L_{eb}}{L_c}\right)^{1/m}\left(A_{eff}\right)^{d_0/\Delta d} \tag{2.21}$$

In general, interfacial shear strength is affected by the surface nature of CNTs, stating its value does not change significantly. In case of post-treatment on CNTY, surface nature changes and both surface fraction and interfacial shear strength are influenced. Due to the characteristics of the elementary bundle model developed so far, the surface modification is applied only to the outermost wall of the CNT at the outermost part of the elementary bundle. The energy of the surface-modified elementary bundle (E_ω) is expressed as equation (2.22),

$$E_\omega = 2\pi R_n(3N-2)(1-\Omega)(\gamma+\omega\Delta\gamma) + \frac{2\pi}{2R_n(1-\Omega)} \\ \times\left\{\int_1^{N-1}\frac{D_n dj}{2j-1} + \int_{N-1}^{N}\frac{(D_n+\omega\Delta D_G)dj}{2j-1}\right\} \tag{2.22}$$

where ω is area fraction of chemically modified region. In the case of total surface energy, only the outermost CNTs are already applied, stating there is no change in the number of CNT. Rather, only γ value is replaced by $\gamma+\omega\Delta\gamma$. On the other hand, in the case of

curvature energy, since the chemical modification occurs only in the outermost layer of CNT in elementary bundle, the integral form is separated. Also, since the chemical modification is applied only to the outermost wall of the CNT, D_n was replaced with $D_n + \omega \Delta D_G$. As a result, the surface area fraction (Ω_ω) of surface modified elementary bundle is expressed as equation (2.23).

$$\Omega_\omega = 1 - (1 - \Omega_{eb}) \sqrt{\frac{1 + \frac{\Delta D_G}{D_n}\left(1 - \frac{ln(\alpha - 2)}{ln\,\alpha}\right)\omega}{1 + \frac{\Delta\gamma}{\gamma}\omega}} \qquad (2.23)$$

Through the surface modification, the interfacial shear strength, τ_{eb}, is replaced with τ_ω ($=\tau_{eb}+\omega\Delta\tau$). Since only surface area fraction and interfacial shear strength is modified by surface treatment, the strength ratio of surface treated CNTY (σ_ω) to pristine CNTY (σ_0) is calculated as ($\Omega_\omega\tau_\omega$)/($\Omega_{eb}\tau_{eb}$). Combining with equation (2.23), the strength ratio is expressed as equation (2.24).

$$\frac{\sigma_\omega}{\sigma_0} = \frac{1}{\Omega_{eb}} \times \left[1 - (1 - \Omega_{eb}) \sqrt{\frac{1 + \frac{\Delta D_G}{D_n}\left(1 - \frac{ln(\alpha - 2)}{ln\,\alpha}\right)\omega}{1 + \frac{\Delta\gamma}{\gamma}\omega}}\right] \times \left(1 + \frac{\Delta\tau}{\tau_{eb}}\omega\right) \quad (2.24)$$

According to equation (2.23), among factors influencing specific strength, surface treatment, especially chemical crosslinking, increases the interfacial shear strength while decreases the contact between elementary bundles. Since strength-decreasing factor comes from Ω, main factors influencing strength are ΔD_G and $\Delta\gamma$. From the material point

of view, low surface energy and high bending rigidity prevent elementary bundle to dense packing, which is unfavorable for high strength CNTY. On the other hand, in case of crosslinking, $\varDelta\gamma$ indicates the covalent bond energy of linking reagent. Since the weakest point of linking reagent is normally single-bond between two atoms, the bond energy can be considered to be constant, about 300 to 400 kJ/mol. Expanding this perspective further, a new factor, K ($=\sigma_0\times\varDelta\tau/\tau_{eb}$), which excludes the structural factor of CNTY by multiplying the initial strength of CNTY and rate of change in interfacial shear strength, is also related to the covalent bond energy. The factor K can be also considered as constant. Therefore, since $\varDelta\tau$ is not an adjustable variable, in order to fabricate higher strength CNTY, decreasing $\varDelta D_G$ as well as increasing $\varDelta\gamma$ is required by employing suitable linking reagent.

2.3.6 Interfacial shear strength of elementary bundle

If the elementary bundles in the CNTY are ideally evenly distributed, the equation (2.21) will be satisfied. However, in reality, there is a non-ideal point, which causes an error. The non-ideal point is the part where the endpoints of the elementary bundle that exist in the secondary bundle are concentrated. Such point acts as a flaw in the CNTY and cause brittle failure. Therefore, it is necessary to revise the equation (2.21) using a weakest point theory based on Griffith theory.

Griffith theory predicts the ultimate strength through the balance between the atomic bond energy and strain release energy applied to the flaw of a brittle material. Even if the CNTY showed a brittle mode through the rupture of the secondary bundle, the covalent bond in the CNT is not destroyed, indicating the shear energy of the elementary bundle should be used instead of the atomic bond energy. Since the smallest flaw is an elementary bundle, the shear energy can be expressed in the form of $2\gamma\Omega_{eb}t_{eb}\times(3N_{eb}^2-$

$3N_{eb}+1)\times 2\pi R_{eb}L_{eb}$. On the other hand, the strain release energy is defined as toughness of secondary bundle multiplied by the volume of elementary bundle ($=\pi R_{eb}^2 L_{eb}$). The classification of secondary bundles is determined depending on whether toughness represents only elastic energy or includes plastic energy, which can be summarized in the Table 2.1.

In Fig. 2.4a, the failure of CNTY includes two brittle modes and one slipping mode. Since the shear energy of the microbundle is lower than the elastic strain energy, the shear between the microbundles does not contribute to the load transfer in the plastic region. As a result, it appears mainly at the very end of brittle failure or just before the elementary bundle emerges. The mesobundle, whose shear energy is larger than the elastic strain energy, contributes a lot to load transfer through slippage in the plastic region. Since the shear energy is smaller than the plastic strain energy, it contributes to the brittle mode and appears mainly between the failure part of the CNTY and the body part. The macrobundle, whose shear energy is greater than the plastic strain energy, contributes to load transfer through slippage in all areas. As a result, the elongation of the CNTY is improved by revealing the plastic instability or exhibiting a slipping mode in failure. However, since the final strength is mainly determined by the brittle mode, it can be inferred that the highest strength can be achieved when the CNTY consists of one macrobundle.

According to Y. Bai et al. [18] the elastic strain energy of elementary bundle is 0.9 GJ/m^3, where the plastic strain energy is 3.6 GJ/m^3. Based on the two energies, with assumption of ideally compacted structure ($t_{eb}=1$), the classification of secondary bundles according to the unit CNT can be known by finding the N_{eb}. The diameter of micro, meso and macrobundle accordingly can be expressed as ($2N_{eb}-1)\times 2R_{eb}$ (Fig. 2.17). In particular, the plot results for DWCNT shown in Fig. 2.17 states that the boundaries

of the diameter of secondary bundle for micro-mesobundle and meso-macrobundle are 390nm and 790nm, respectively. Such result corresponds well with fractography of Fig. 2.4a, indicating our classification of secondary bundle is reasonable to predict the load transferring mechanism of CNTY.

In the above work, the standard of the secondary bundle was set as an ideal case with a minimum flaw of an elementary bundle. Therefore, a more realistic situation should be reflected in the strength thereafter. In most cases, a flaw is a misoriented microbundle, and the strength of the CNTY should be predicted by reflecting this. In the case of microbundle, since it is involved in elastic strain energy, toughness can be expressed as $\sigma^2/2E$ where and σ are E (≈ 0.7 TPa [18]) strength and Young's modulus, respectively. On the other hand, the shear energy of microbundel can be expressed as $2\gamma\Omega_{eb}t_{eb}\times(3N_{eb}^2-3N_{eb}+1)\times2\pi(2N_{eb}-1)R_{eb}L_{eb}$. Through the condition in which the shear energy and the elastic strain energy are balanced, strength of CNTY is expressed by equation (2.25).

$$\sigma_{CNTY} = \sqrt{\frac{8\Omega_{eb}\gamma\left(A_{eff}\right)^{d_0/\Delta d} \times E}{R_{eb}} \times \frac{3N_{eb}^2 - 3N_{eb} + 1}{2N_{eb} - 1}} \qquad (2.25)$$

If the diameter of the microbundle is known, the actual strength of the CNTY can be predicted using equation (2.25). In the case of CNTY with an effective area ratio of 0.9 and a specific strength of 4.0 N/tex, it has an internal structure as shown in Fig. 2.18 and the diameter of the microbundle does not exceed 200nm. When the strength is predicted by reflecting such a case in equation (2.25), it is expressed as a plot as shown in Fig. 2.19, well matched with the actual strength. Furthermore, as long as the microbundle exists inside the CNTY, in case of DWCNT, the specific strength of the CNTY can reach

up to 7 N/tex. Such result states that modified Griffith theory based on brittle failure is effective for estimation of strength in reality.

Table 2.1. Classification of secondary bundle based on energy comparison.

Secondary bundle	Energy
Microbundle	Shear energy < Elastic strain energy
Mesobundle	Elastic strain energy < Shear energy < Plastic strain energy
Macrobundle	Plastic strain energy < Shear energy
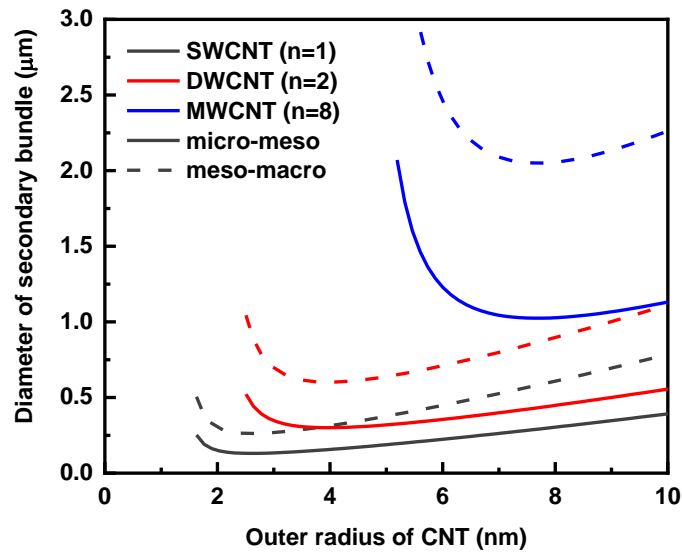
Fig. 2.17. Diameter of secondary bundle according to outer radius and number of walls of CNT. (Solid line and dashed line indicates the boundary of micro-meso and meso-macrobundle, respectively.)
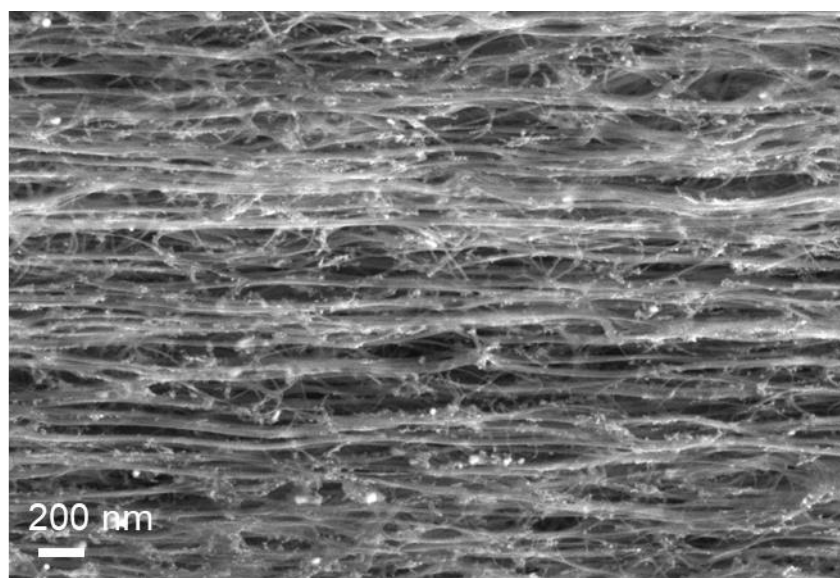
Fig. 2.18. SEM image of internal structure of as-spun CNTY.
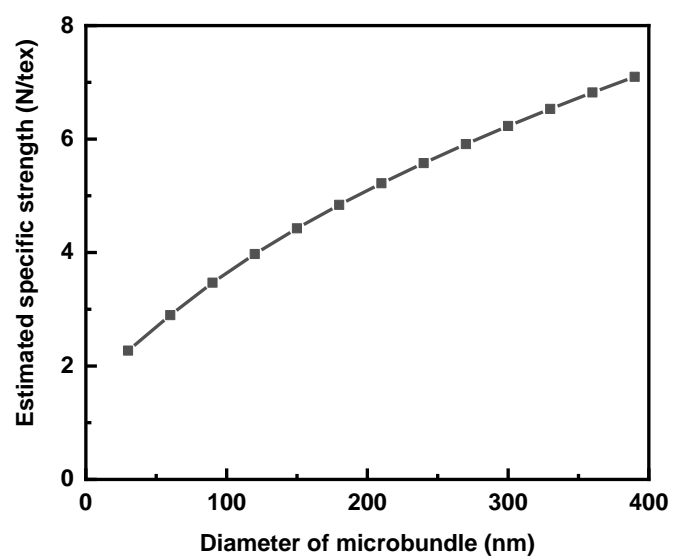
Fig. 2.19. Estimated strength of CNTY according to diameter of microbundle.

2.4 Conclusion

The unique nanostructure, CNT elementary bundle, is determined by the stabilization energy of CNTs in assembly and cohesive energy between CNTs. Since the strength of elementary bundle is estimated to be comparable to that of CNT, CNTYs show typical yarn failure breaking by slippage between CNT elementary bundles. Therefore, specific strength of CNTYs can be estimated by number and surface area fraction in contact, length and interfacial shear strength of elementary bundle that were determined from structural parameters such as diameter and number of walls. The contact area is the key to calculate the total shear force and predict the specific strength of CNTYs. The deformability of elementary bundles in radial direction is highly related with the fraction of surface area in contact with neighboring elementary bundles, derived from the total energy of elementary bundle. Also, the total number of elementary bundles composing CNT assembly, which is secondary bundle, should be applied to determine contact area. Furthermore, the effect of surface treatment on surface area fraction and interfacial shear strength should be considered. As a result, the maximum specific strength is expressed as following equation (2.26).

$$\sigma_{est} = \frac{1}{\Omega_{eb}} \left[1 - (1 - \Omega_{eb}) \sqrt{\frac{1 + \frac{\Delta D_G}{D_n}\left(1 - \frac{ln(\alpha - 2)}{ln\,\alpha}\right) \times \omega}{1 + \frac{\Delta \gamma}{\gamma} \times \omega}} \right. \\ \left. \times \left(k\Omega_{eb}\tau_{eb}(L_{eb})^{1/m}\left(A_{eff}\right)^{d_0/\Delta d} + K\omega \right) \right] \tag{2.26}$$

Larger assembly of elementary bundle from CNT of large diameter and less number of wall crosslinked by polar linking reagent is favorable to fully utilize CNT surface for load-bearing, resulting to higher mechanical properties of CNTYs. Furthermore, the actual strength of CNTY can be estimated as equation (2.25), stating larger microbundle leads to higher strength of CNTY.

2.5 Reference

[1] M. Zhang, K.R. Atkinson, R.H. Baughman, Multifunctional Carbon Nanotube Yarns by Downsizing an Ancient Technology, Science 306(5700) (2004) 1358-1361.

[2] J. Zhao, X. Zhang, J. Di, G. Xu, X. Yang, X. Liu, Z. Yong, M. Chen, Q. Li, Double-Peak Mechanical Properties of Carbon-Nanotube Fibers, Small 6(22) (2010) 2612-2617.

[3] M. Miao, The role of twist in dry spun carbon nanotube yarns, Carbon 96 (2016) 819-826.

[4] J.J. Vilatela, J.A. Elliott, A.H. Windle, A Model for the Strength of Yarn-like Carbon Nanotube Fibers, ACS Nano 5(3) (2011) 1921-1927.

[5] J.A. Elliott, J.K.W. Sandler, A.H. Windle, R.J. Young, M.S.P. Shaffer, Collapse of Single-Wall Carbon Nanotubes is Diameter Dependent, Phys. Rev. Lett. 92(9) (2004) 095501.

[6] J. Tang, L.-C. Qin, T. Sasaki, M. Yudasaka, A. Matsushita, S. Iijima, Compressibility and Polygonization of Single-Walled Carbon Nanotubes under Hydrostatic Pressure, Phys. Rev. Lett. 85(9) (2000) 1887-1889.

[7] Y. Wei, B. Wang, J. Wu, R. Yang, M.L. Dunn, Bending rigidity and Gaussian bending stiffness of single-layered graphene, Nano Lett. 13(1) (2013) 26-30.

[8] A. Kozbial, Z. Li, C. Conaway, R. McGinley, S. Dhingra, V. Vahdat, F. Zhou, B. D'Urso, H. Liu, L. Li, Study on the surface energy of graphene by contact angle measurements, Langmuir 30(28) (2014) 8598-606.

[9] L.A. Girifalco, M. Hodak, R.S. Lee, Carbon nanotubes, buckyballs, ropes, and a universal graphitic potential, Phys. Rev. B 62(19) (2000) 13104-13110.

[10] J. Zhao, Y. Jia, N. Wei, T. Rabczuk, Binding energy and mechanical stability of two parallel and crossing carbon nanotubes, Proc. R. Soc. A 471(2180) (2015) 20150229.

[11] Y. Jung, T. Kim, C.R. Park, Effect of polymer infiltration on structure and properties

of carbon nanotube yarns, Carbon 88 (2015) 60-69.

[12] O.-K. Park, H. Choi, H. Jeong, Y. Jung, J. Yu, J.K. Lee, J.Y. Hwang, S.M. Kim, Y. Jeong, C.R. Park, M. Endo, B.-C. Ku, High-modulus and strength carbon nanotube fibers using molecular cross-linking, Carbon 118 (2017) 413-421.

[13] J. Lee, D.M. Lee, Y. Jung, J. Park, H.S. Lee, Y.K. Kim, C.R. Park, H.S. Jeong, S.M. Kim, Direct spinning and densification method for high-performance carbon nanotube fibers, Nat. Commun. 10(1) (2019) 2962.

[14] E. Oh, H. Cho, J. Kim, J.E. Kim, Y. Yi, J. Choi, H. Lee, Y.H. Im, K.H. Lee, W.J. Lee, Super-Strong Carbon Nanotube Fibers Achieved by Engineering Gas Flow and Postsynthesis Treatment, ACS Appl. Mater. Interfaces 12(11) (2020) 13107-13115.

[15] N. Pan, T. Hua, Y. Qiu, Relationship Between Fiber and Yarn Strength, Tex. Res. J. 71(11) (2001) 960-964.

[16] A. Pantano, M.C. Boyce, D.M. Parks, Nonlinear Structural Mechanics Based Modeling of Carbon Nanotube Deformation, Phys. Rev. Lett. 91(14) (2003) 145504.

[17] A. Pantano, D. M. Parks, M.C. Boyce, Mechanics of deformation of single- and multi-wall carbon nanotubes, J. Mech. Phys. Solids 52(4) (2004) 789-821.

[18] Y. Bai, R. Zhang, X. Ye, Z. Zhu, H. Xie, B. Shen, D. Cai, B. Liu, C. Zhang, Z. Jia, S. Zhang, X. Li, F. Wei, Carbon nanotube bundles with tensile strength over 80 GPa, Nat. Nanotechnol. 13(7) (2018) 589-595.

Chapter 3 Relationship between Self-Assembly Characteristics of CNT Microbundles and Tensile Strength of CNTYs

3.1　Introduction

A CNT yarn (CNTY) [1], a one-dimensional assembly of CNTs, is known to have strength equivalent to a few percent of individual CNTs. A fiber implementing the mechanical properties of CNT have not yet been reported. The most ideal approach to overcoming discrepancies in mechanical properties between individual CNT and CNTY are to synthesize unlimitedly long CNTs so that failure would arise from CNT breakage instead of slippage between CNTs [2], which is the main failure mechanism of CNTY. Even though few research groups have reported on the growth of centimeter scale-long CNT through control over the catalyst lifetime and optimization of the synthesis conditions [3, 4], unexpected drawbacks have occurred. These include long synthesis times as essential prerequisites [5, 6], stating that the suggested methods are not practical for commercially available CNTYs.

Accordingly, recent advances in CNTYs have been directed toward strengthening the interaction between CNTs, which determines the performance of CNTY. The tensile strength of CNTY scales with the aspect ratio of constituent CNTs as long as the intertube friction dominantly determines the strength of CNTY [7-10]. The theoretical

calculation has predicted that the achievable strength of CNTY could be comparable to that of CNT if the constituent CNTs are longer than a certain length and perfectly dense along the yarn axis [11]. Although the tensile strength of 5.5 N/tex is the currently achievable maximum strengths [12], they had to go through tedious, complicated and environmentally unfriendly processes in order to reach the goal [12-16].

In this chapter, we report a possible route to enhancing the specific tensile strength of CNTY closely to its theoretical maximum strength through the *in-situ* direct spinning method, which is fast, simple, and ecologically friendly. The specific strength of CNTYs with various bundle structures was analyzed according to the theory in chapter 2 and the maximum strength possible through the *in-situ* direct spinning technique was predicted to be 5.6 N/tex with our CNTs. Furthermore, we successfully fabricated as-spun CNTY with an average specific strength of 4.5 N/tex, which is 80% of the estimated maximum strength achievable, exceeding that of previously ever-reported as-spun CNTY. From the bundling and orientation behavior analysis of CNTs, the self-assembly behavior control was suggested to be one of the most influential factors determining the specific strength of the resultant as-directly-spun CNTY.

3.2 Experimental

Synthesis of DWCNTs and DWCNT yarns

A DWCNT yarn was synthesized by a floating catalyst chemical vapor deposition method using a vertical alumina tube reactor that had inner diameter of 85mm and length of 1800 mm. Ferrocene, thiophene, and methane were used as the catalyst precursor, promoter, and carbon source, respectively, for the CNT synthesis at 1200 °C. Ferrocene and thiophene were purchased from Sigma Aldrich (South Korea) and used as received without any further purification. For synthesis conditions, the flow rate of H_2 (99.999%), CH_4 (99.999%), and Ar (99.999%) are fixed at 1200 sccm, 60 sccm, and 500 sccm, respectively. The temperatures of the ferrocene container and the thiophene bubbler were fixed at 80 °C and −20 °C, respectively. Both catalyst precursors were supplied as H_2 flowing into the system at a rate of 0.5 mg/min and 3.6 mg/min, respectively. The total H_2 flow rate was maintained at 1200 sccm by adjusting the additional H_2 flow rate. The CNTY was spun on a bobbin after passing through water at the bottom of the vertical furnace at a spinning rate of 6 m/min. For the drawing, the yarn passed through the guide roller and reached the bobbin. Consequently, the guide roller was located 8cm above the bobbin and 8cm sideways.

Characterization of CNT yarns

The nanostructure of CNTs was characterized by HR-TEM (JEM-2100F, JEOL) and Raman spectroscopy (RAMANplus, Nanophoton) using 532 nm laser. The thermal gravimetric analysis (TGA; SDT-Q600, TA Instruments) was used to measure the purity of CNTs in air atmosphere. The nanostructures of CNT were observed through field-

emission transmission electron microscopy (JEM-3000F, JEOL, Japan). The internal structures of the CNT yarn were observed through field-emission scanning electron microscopy (SUPRA 55VP, Carl Zeiss, Germany) after cutting with a focused ion beam (FIB; Helios 650, FEI). Furthermore, the specific strength was calculated by linear density, which was determined by weighing 15 m-long CNT yarn, divided into a measured load of a single yarn with tensile stage (TST350, Linkam) at a gauge length of 10 mm and strain rate of 3 mm min^{-1}. In the case of the *in-situ* Raman analysis, the tensile stage for which the sample was set at a gauge length of 30 mm was placed in a Raman device and measured when strain is applied to CNTY.

3.3 Result and discussion

Double-walled CNTs (DWCNT) are synthesized through floating catalyst chemical vapor deposition (FCCVD) as previous reports [16-20]. To control the self-assembly behavior of CNT, the synthesized aerogel-like CNT assembly with highly connected network structure is spun as a continuous fiber by passing through water at the bottom of the vertical furnace followed by drawing at the guide roller, as shown in Fig. 3.1. The guide roller was located 8cm above the winding roller and 8cm sideways while the synthesized as-spun CNTY was drawn at the winding rate of 5 to 9 m/min without any additional treatments. CNTY was named the DW-SA-X, where X indicates the winding rate.

As a result of analyzing DW-SA-6 as the representative, CNTY with a diameter of 20 μm (Fig. 3.2a) and DWCNT with an outer diameter of about 5.5 nm (Fig. 3.2b) were obtained. According to the TGA thermogram in Fig. 3.2c, 79.2 wt% of CNTY is composed of DWCNT while 11.2 wt% and 9.2 wt% of the yarn are amorphous carbon and residual Fe, respectively [21]. A high amount of load-bearing unit, which is proportional to the amount of DWCNT, contributes to the mechanical performance. According to the Raman analysis, the intensity ratio of the D-band to G-band (I_D/I_G) was approximately 0.038 ± 0.009 (Fig. 3.2d), confirming that the DWCNT is highly crystalline. Furthermore, the polarized Raman intensity factor ($I_{GII}/I_{G\perp}$, ratio of G peak intensity parallel to the Raman laser to one in the vertical direction) which shows the degree of CNT orientation [18, 22] was 8.89 ± 1.09, high enough for linear load transfer.
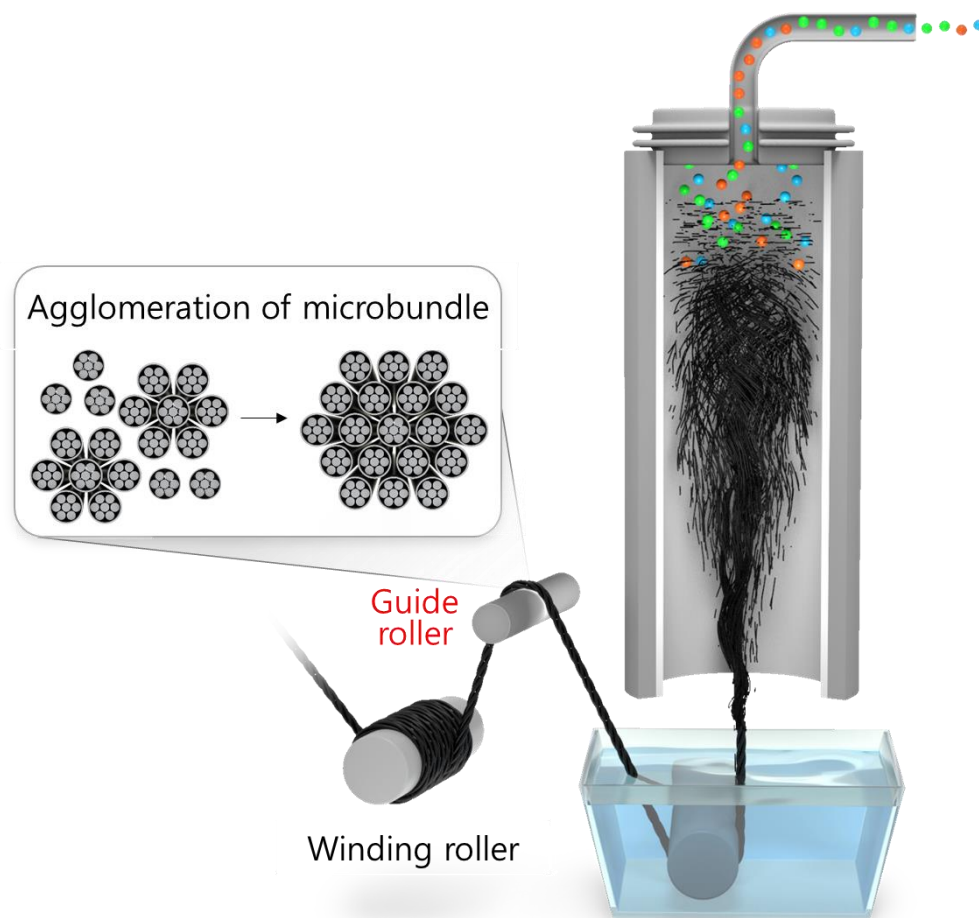
Fig. 3.1. Schematic image of the *in-situ* direct spinning process
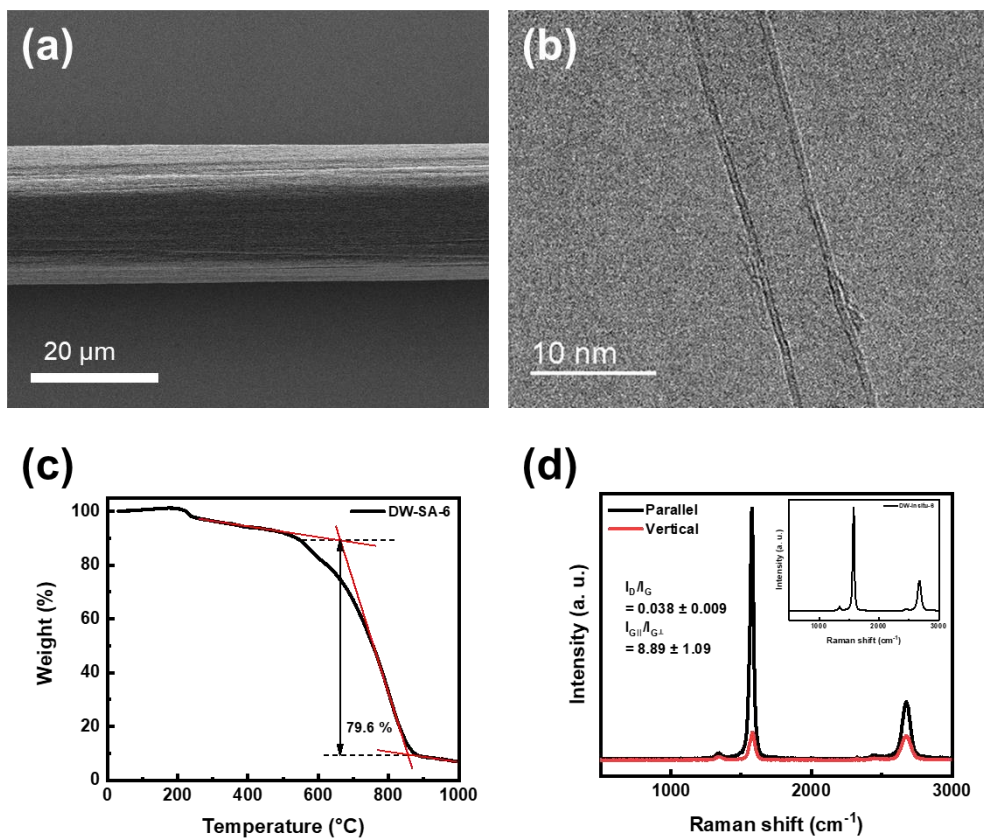
Fig. 3.2. (a) SEM micrograph, (b) TEM micrograph, (c) TGA thermogram, and (d) Polarized Raman spectra (inset: normal Raman spectrum) of as-spun CNTY.

3.3.1 Empirical verification of microbundle theory

3.3.1.1 Bundling property: Effective area ratio

The FIB analysis for DW-SA-5~9 was performed to confirm the correlation between bundling behavior and strength (Fig. 3.3). When the spinning rate was 6 m/min, the specific strength reached the optimal point. As the rate increased, the specific strength decreased, which matches the bundling behavior. As shown in Fig. 3.3a-e, it becomes impossible to measure the diameter of the mesobundle or macrobundle as CNT aggregation takes place. Thus, from equation (2.3), we derived equation (3.1) to linearly fit the effective area ratio (A_{eff}) to strength of CNTY in logarithmic scale.

$$\log \sigma_{CNTY} = \frac{d_0}{\Delta d} \log A_{eff} + y_{intercept} \tag{3.1}$$

Since the slope and y-intercept are empirical factors, A_{eff} and σ_{CNTY} of Fig. 3.3a-e were plotted on a logarithmic scale to confirm the equation (Fig. 3.3f). The graph clearly shows that the equation linearly fits well to experimental data, resulting in a slope of 2.3 and intercept of 0.74. This supports the assumption that the load-bearing element of the CNT yarn proposed previously was correct. The intercept indicates the logarithm of maximum specific strength is achievable through CNT bundling when the intrinsic property of CNT is determined. The maximum specific strength of the CNTY that can be achieved with CNT synthesized under the same conditions was 5.6 GPa/(g cm^{-3}).
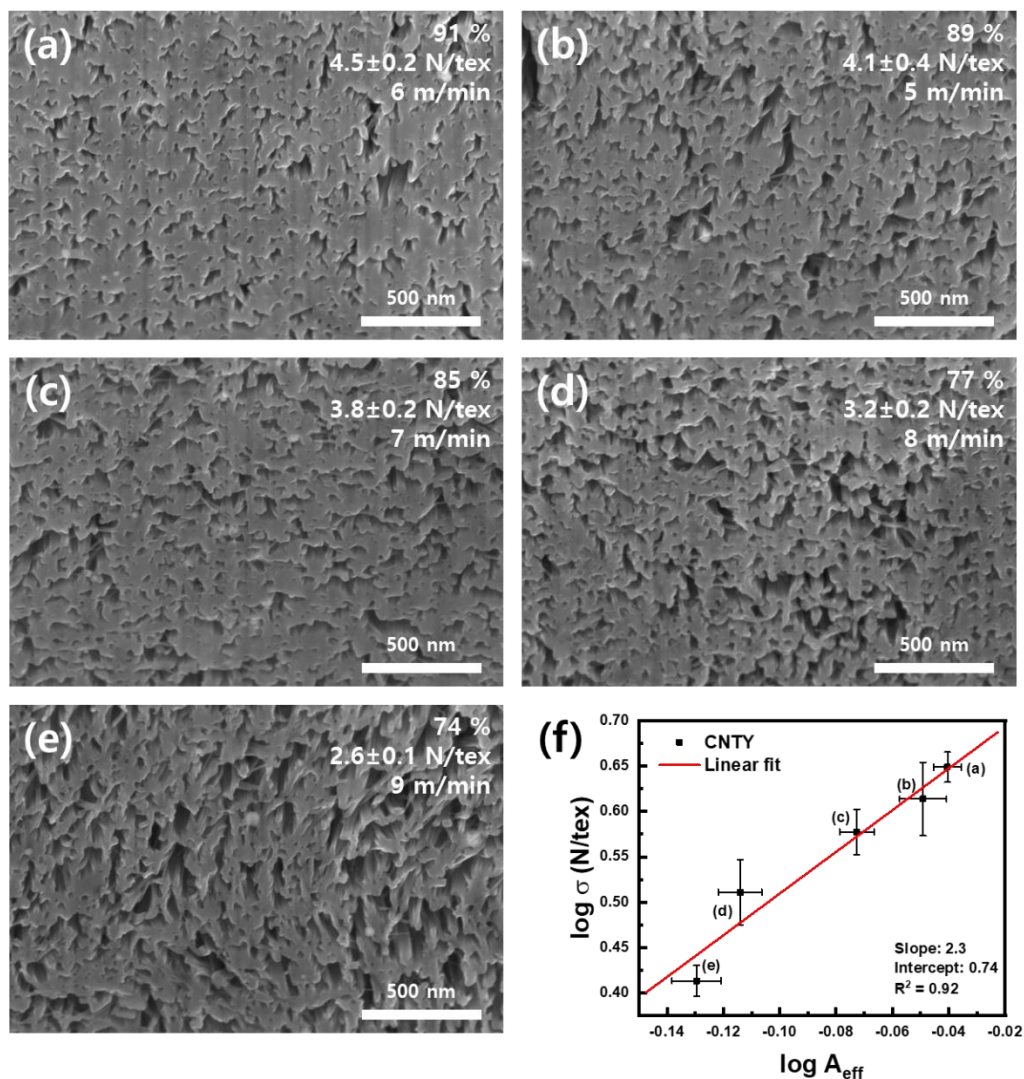
Fig. 3.3. (a-e) SEM micrographs of radial cross sections of FIB cuts of DWCNT yarns with effective area ratios, specific strengths, and spinning rates in the upper right of the image. (f) The log-log plot of specific strength (σ) and effective area ratio (A_{eff}) are based on FIB data (a-e).

3.3.1.2 Length property: Weibull analysis

The Weibull analysis for DW-SA-5~9 was performed to confirm structural factors of CNTY. From equation (2.14), equation (3.1) was derived to linearly fit the strength (σ) to the probability (P) of yarn failure at given tensile load in logarithmic scale where σ_s is scale factor and m is shape factor.

$$ln\{-ln(1 - P)\} = mln(\sigma) - mln(\sigma_s) \tag{3.2}$$

As described in chapter 2, the shape factor describes the dispersion of fiber strength along a fiber length. The fiber known as ductile and uniform material is known to have high shape factor. Fig. 3.4 is presenting the plot of DW-SA-5~9 and Table 3.1 is summarizing the analysis based on equation (3.2). Every yarn group showed shape factor around or over 10. Such values are high enough to get Coleman factor around 1. Thus, the strength of microbundles in DW-SA-5~9 is comparable to the strength of CNT, indicating the assumption on chapter 2 is applicable. Therefore, according to equation (2.17), the strength of CNTY is proportional to 0.1 power of length of microbundle.

However, in DW-SA-5~9, the spinning method has changed, but the synthesis conditions have not changed. Thus, it can be assumed that the length of the microbundle is the same in all samples. According to previous reports, it is known that the length of the microbundle reaches several hundred μm. The difficulty in measurement states that further research is required.
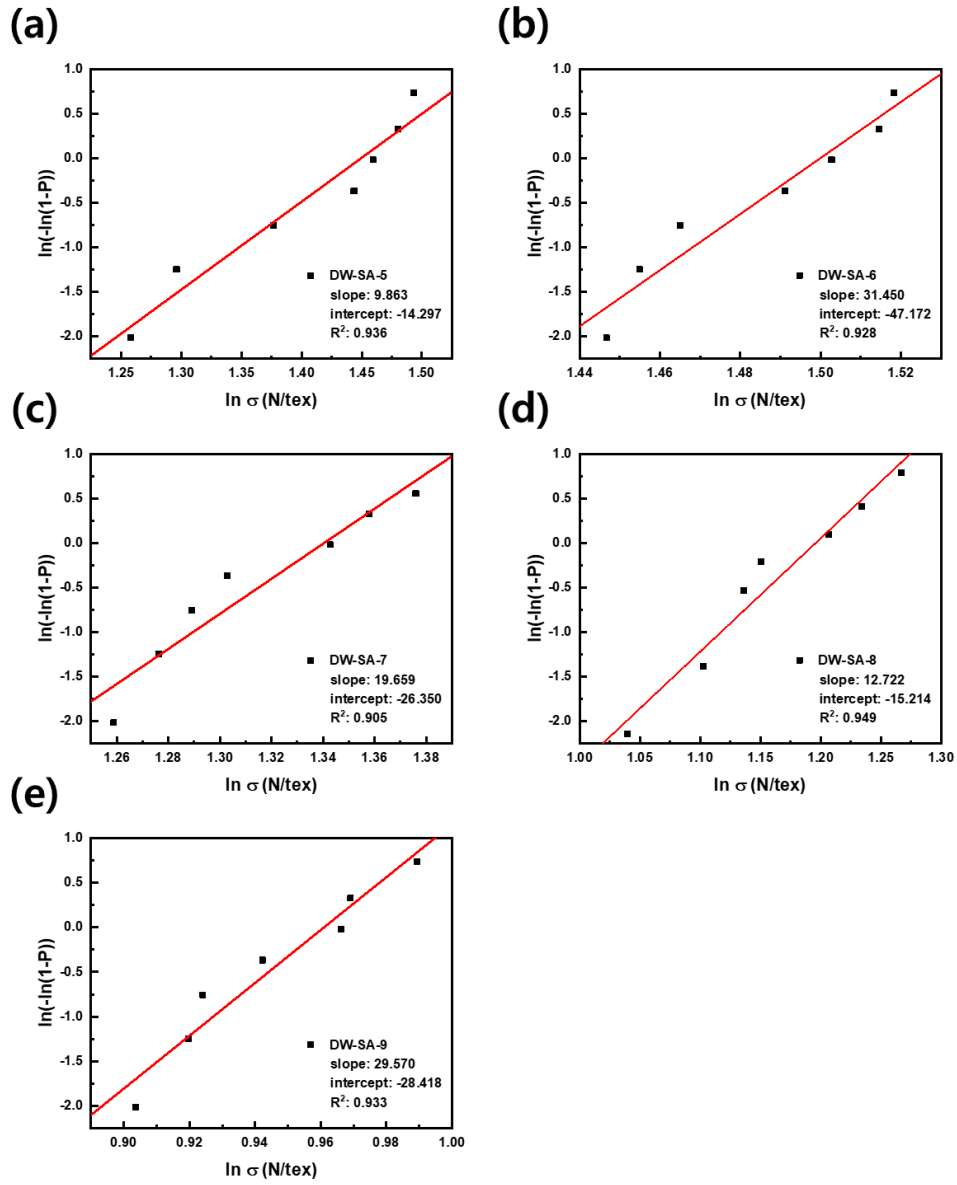
Fig. 3.4. Plot of Weibull analysis on group of (a) DW-SA-5, (b) DW-SA-6, (c) DW-SA-7, (d) DW-SA-8 and (e) DW-SA-9.

Table 3.1. Weibull analysis on group of DW-SA-5~9.

Sample	$\sigma_{average}$ (N/tex)	σ_s (N/tex) (scale)	m (shape)	R^2	Ψ (Coleman)
DW-SA-5	4.12	4.26	9.86	0.936	1.33
DW-SA-6	4.46	4.48	31.49	0.928	1.13
DW-SA-7	3.79	3.82	19.66	0.905	1.19
DW-SA-8	3.24	3.31	12.72	0.949	1.27
DW-SA-9	2.60	2.61	29.57	0.933	1.14

3.3.2 Mechanical property from self-assembly behavior

3.3.2.1 Mechanical properties of *in-situ* directly spun CNTYs

Among in-situ as-directly-spun CNTYs, we experimentally achieved specific strength of 4.5±0.2 N/tex with specific stiffness of 141.1±9.9 N/tex through DW-SA-6 (Fig. 3.5a). (Fractography of DW-SA-6 is described in chapter 2 with Fig 2.4.) Our results reached 80% of the theoretically predicted maximum specific strength, which surpassed the carbon fiber T1100 (~3.9 N/tex), known as one of the strongest fibers in recent times. In order to examine the in-situ self-assembly, CNTY was fabricated by general direct spinning without the guide roller. In comparison, CNTY was manufactured with a winding rate of 6 m/min and called DW-Raw-6. The specific strength of DW-Raw-6 was 3.0±0.1 N/tex with specific stiffness of 140.6±22.0 N/tex (Fig. 3.5b). The results state that the specific strength of the CNTY was increased by 48% through *in-situ* self-assembly.

This is also effective for the post treatment on DW-Raw-6. Consequently, post treatment was carried out in an *ex-situ* self-assembly method in which DW-Raw-6 was released after a specific strain was applied for 10 seconds. The strain was applied up to 0.5~2.5% and the specific strength of CNTY to which strain was applied was shown in Fig. 3.5c. Until the applied strain reached 2%, the specific strength steadily increased and showed a maximum value of 4.4±0.1 N/tex. After 2%, the specific strength showed a decreasing trend. The maximum value is almost the same as when the *in-situ* direct spinning indicates a self-assembly of about 2% strain was applied to CNTY in the *in-situ* direct spinning. Such result well matches with the strength of DW-SA samples. As the spinning rate increases, the strain applied during self-assembly increases. The strength of DW-SA sample is optimized at spinning rate of 6 m/min, which matches with

strain of 2%. (Spinning rate of 7~9 m/min matches with strain over 2%, whereas 5 m/min matches with strain under 2%.)
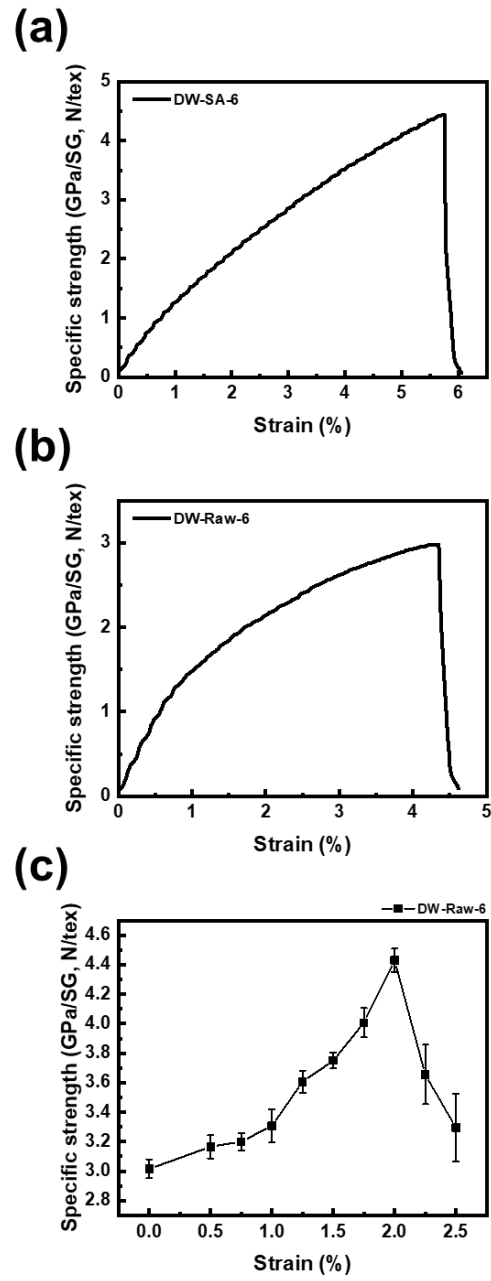
Fig. 3.5. The stress-strain curve of (a) DW-SA-6 and (b) DW-Raw-6, (c) the specific strength of DW-Raw-6 after *ex-situ* self-assembly.

3.3.2.2   Self-assembly behavior of CNTs in yarn: bundling

The mechanical properties of CNTY are determined by the assembly of CNTs due to the characteristics of the load-bearing mechanism. Each CNTY was analyzed according to the assembly classification, which are bundling and orientation behavior. First, the bundling behavior of microbundles in CNTY in the static state (Fig. 3.6a) and the dynamic state (Fig. 3.6b and c) was analyzed using Raman spectroscopy. The key factor for the total area of shear failure depends on the extent of bundling of the CNT microbundles. The Raman band is strongly resonant under deformation of CNTs and the down shift rate of the G' peak implies load transfer efficiency between CNT with neighboring CNTs [23, 24]. In addition, the higher load transfer efficiency guarantees effective dissipation of applied energy. Since the applied energy in CNTY dissipates by slippage between CNT microbundles in a mesobundle, a larger mesobundle indicates higher efficiency of load transfer with the larger down shift of the G' peak. The Raman G' peak of DWCNT yarns with Lorentzian fitting are provided in Fig. 3.6a. Since the orthogonal electronic dispersion occurs when CNTs are in contact with each other and the G' peaks shift to lower energies, the G' peak shift is reflecting the inter-nanotube contact area. The G' peak shifted from 2674.4 cm^{-1} of DW-Raw-6 to 2666.7 cm^{-1} of DW-SA-6 through *in-situ* self-assembly so that dense packing was already achieved from the initial static state.

To further analyze the load-bearing mechanism of CNTY, DW-Raw-6 (Fig. 3.6b) and DW-SA-6 (Fig. 3.6c) were analyzed through *in-situ* Raman spectroscopy during tensile strain. In both cases, the deformation behavior of CNTY was shown to have 4 zones. In Zone I, which is the elastic region, individual CNT microbundles or mesobundles are aggregated and reoriented to form larger, reversible bundle. Zones II to IV were the plastic region. In Zone II (yielding zone), mesobundles that have already increased in

105

size in the elastic region are merged further with nearby bundles. As bundles get stretched in Zone III (slipping zone), slippage occurs between CNT microbundles in and around the mesobundle. Finally, in Zone IV (failing zone), partial failure occurs.

The transfer efficiency of DW-SA-6 was -13.65 cm^{-1}/% whereas that of DW-Raw-6 was -13.62 cm^{-1}/% in Zone I. The load transfer efficiency did not show a significant difference and matched the modulus of DWCNT yarns. On the other hand, a significant difference was found in Zone II. The widened Zone II of DW-SA-6 states the assembly of CNT in DW-SA-6 was able to withstand more yielding due to the enhanced bundling. This is also consistent with the results of Fig. 3.5c, which improved the specific strength by applying strain to Zone II of DW-Raw-6. The static and dynamic analysis indicates that as bundling behavior conditions where CNTs could aggregate were formed, it became possible to withstand a larger load and improve the specific strength of CNTY.
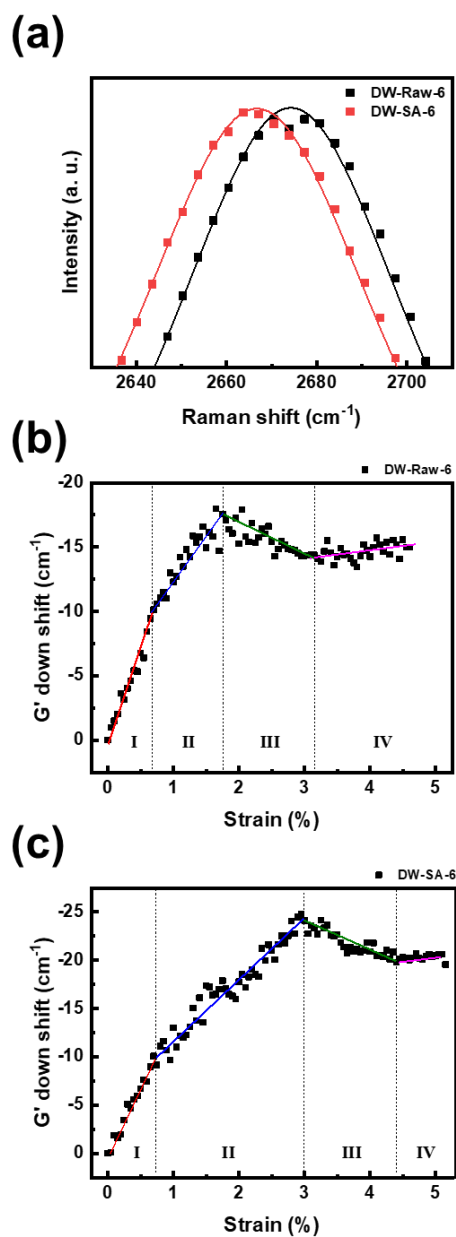
Fig. 3.6. (a) Raman spectra of the G' peak (symbol) that is fitted using a Lorentzian function (solid line) of DWCNT yarns. The down shift rate of the G' peak of (b) DW-Raw-6 and (c) DW-SA-6 during tensile loading.

3.3.2.3 Self-assembly behavior of CNTs in yarn: orientation

The orientation behavior of CNTY in the static state (Fig. 3.4d and 3.7a) and dynamic state (Fig. 3.7b and c) was analyzed using polarized Raman spectroscopy. At the initial state, the intensity factor ($I_{GII}/I_{G\perp}$) of DW-Raw-6 was 8.56 ± 1.24 (Fig. 3.7a), showing negligible difference to that of DW-SA-6. Rather, the difference between both yarns appeared in the dynamic state under tensile strain. For DW-Raw-6, the orientation was changed according to the bundling behavior and was involved in the load transfer (Fig. 3.7b). Particularly in Zone II, the orientation behavior was compromised as the microbundles abandon the previous oriented form and aggregates to the surrounding mesobundles grown through elastic deformation (In Zone III, orientation increased by stretching the bundle). As the bundling and orientation behaviors were reversed, efficient load transfer could not be achieved. On the other hand, the orientation of CNTs in DW-SA-6 was constant regardless of strain (Fig 3.7c). Since dense packing between bundles has already been made in an aligned form in DW-SA-6, the orientation behavior that did not interfere with bundling led to an efficient load transfer. This self-assembly control of CNT was the key to improving the specific strength of CNTY through *in-situ* self-assembly.

Fig. 3.8 summarizes the load bearing mechanism of CNTY based on the Raman analysis result and the load transferring mechanism of semicrystalline polymer. The amorphous region and the misoriented crystallite of the polymer correspond to the microbundle of the CNTY, whereas remaining crystallite of the polymer corresponds to mesobundle (or macrobundle) of the CNTY. Considering bundling and orientation behavior, at Zone I, the microbundle mainly contributes to load transfer. As amorphous region and misoriented crystallite form oriented crystallite, microbundles agglomerates to mesobundle in oriented form. At Zone II, as crystallites form larger crystallites,

mesobundles aggregates into larger bundle corresponding to the macrobundle. In this process, the orientation of microbundles, which is connecting mesobundles, is distorted due to rearrangement between mesobundles. Then, at Zone III, as crystallite forms a fibrillar structure through slip or twinning, slippage occurs between mesobundles or microbundles. Finally, at Zone IV, partial failure of mesobundle occurs in CNTY.
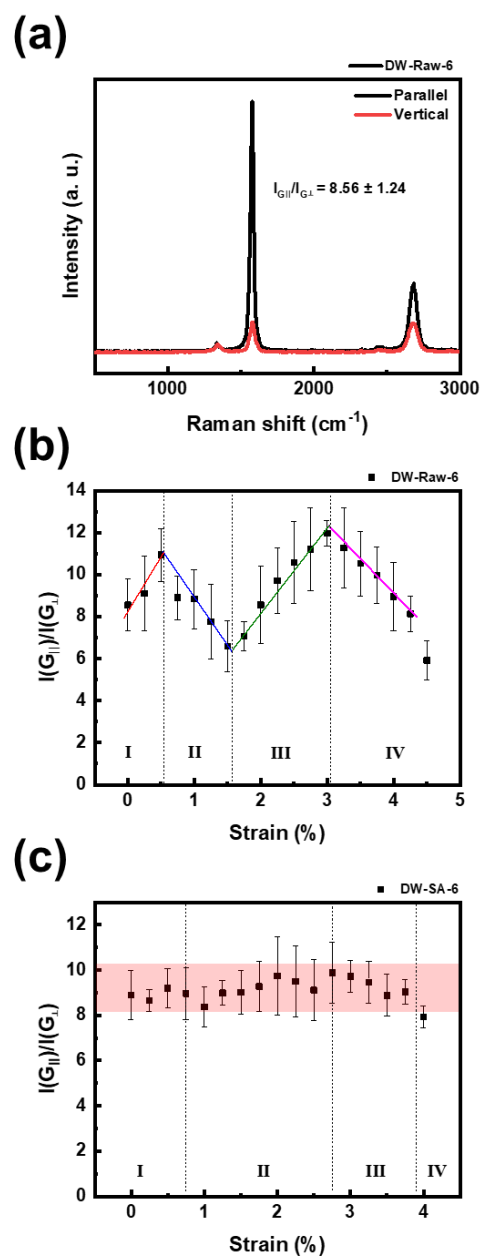
Fig. 3.7. (a) The polarized Raman spectrum of DW-Raw-6 as well as polarized Raman intensity factor of (b) DW-Raw-6 and (c) DW-SA-6 during tensile loading.
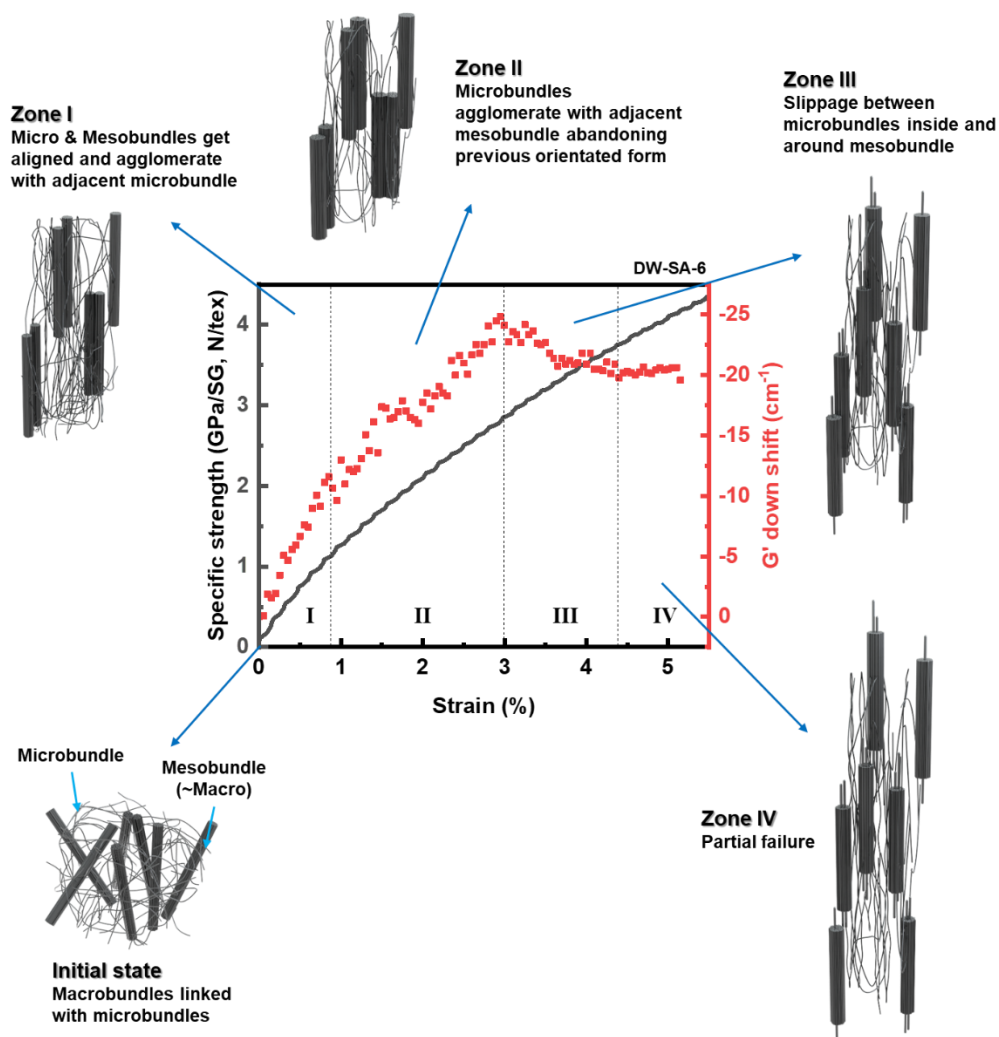
Fig. 3.8. Suggested load bearing mechanism of the CNTY.

The specific strength, specific stiffness, and elongation of CNTYs were compared with those of various state-of-the-art high-performance fibers and metals from industry (Fig. 3.9). Even the commercialized state-of-the-art materials do not possess both high specific tensile strength and elongation. Our CNTY has high-average specific tensile strength (4.5 N/tex) as well as high-elongation (6.3 %) with superfiber class modulus (141 N/tex).
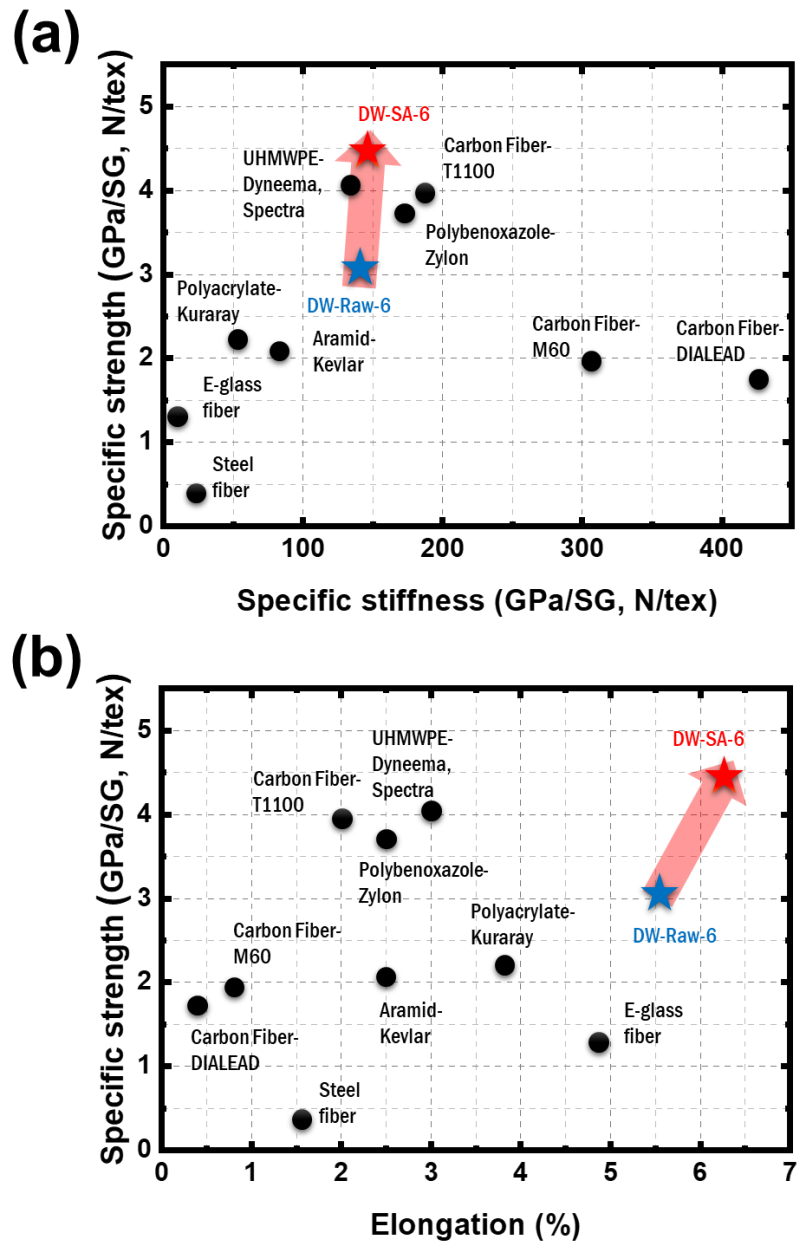
Fig. 3.9. Ashby plot of specific strength versus (a) specific stiffness and (b) elongation of various fibers (circle) with CNTY from this work (star).

3.4 Conclusion

We proposed an *in-situ* direct spinning technique to fabricate CNTYs with comparable or even superior properties to commercialized state-of-the-art fibers and engineering metals. Our findings showed that the theoretical maximum strength of the as-directly-spun CNTY is clarified by the suggested model system, followed by the best ever reported specific strength of the as-directly-spun experimental CNTY. These results highlighted the suitability of appropriate self-assembly engineering with a simple *in-situ* direct spinning technique for achieving ultra-strong CNTYs. Consequently, we opened a new possibility of enhancing the specific strength of CNTY by adopting a couple of post-treatment processes.

3.5 Reference

[1] Y.-L. Li, I.A. Kinloch, A.H. Windle, Direct Spinning of Carbon Nanotube Fibers from Chemical Vapor Deposition Synthesis, Science 304(5668) (2004) 276-278.

[2] Y. Bai, R. Zhang, X. Ye, Z. Zhu, H. Xie, B. Shen, D. Cai, B. Liu, C. Zhang, Z. Jia, S. Zhang, X. Li, F. Wei, Carbon nanotube bundles with tensile strength over 80 GPa, Nat. Nanotechnol. 13(7) (2018) 589-595.

[3] J. Lee, E. Oh, T. Kim, J.-H. Sa, S.-H. Lee, J. Park, D. Moon, I.S. Kang, M.J. Kim, S.M. Kim, K.-H. Lee, The influence of boundary layer on the growth kinetics of carbon nanotube forests, Carbon 93 (2015) 217-225.

[4] C.-H. Lee, S. Park, W.B. Kim, H. Lee, S.-H. Lee, K.-H. Lee, Effect of carbonaceous impurities released from regenerated quartz tubes on the growth of ultra-long carbon nanotube forests, Carbon 167 (2020) 181-187.

[5] J. Lee, E. Oh, H.-J. Kim, S. Cho, T. Kim, S. Lee, J. Park, H. Kim, K.-H. Lee, The reason for an upper limit to the height of spinnable carbon nanotube forests, Journal of Materials Science 48(20) (2013) 6897-6904.

[6] C.-H. Lee, J. Lee, J. Park, E. Lee, S.M. Kim, K.-H. Lee, Rationally designed catalyst layers toward "immortal" growth of carbon nanotube forests: Fe-ion implanted substrates, Carbon 152 (2019) 482-488.

[7] X. Zhang, Q. Li, Y. Tu, Y. Li, J.Y. Coulter, L. Zheng, Y. Zhao, Q. Jia, D.E. Peterson, Y. Zhu, Strong Carbon-Nanotube Fibers Spun from Long Carbon-Nanotube Arrays, Small 3(2) (2007) 244-248.

[8] J. {Ghemes, Jingjing, J. Zhao, G. Xu, J. Di, Z. Yong, Y. Tao, C. Fang, Z. Zhang, X. Zhang, L. Zheng, Q. Li, A comparison of the mechanical properties of fibers spun from different carbon nanotubes, Carbon 49(4) (2011) 1333-1339.

[9] J.J. Vilatela, J.A. Elliott, A.H. Windle, A Model for the Strength of Yarn-like Carbon

Nanotube Fibers, ACS Nano 5(3) (2011) 1921-1927.

[10] A. Ghemes, Y. Minami, J. Muramatsu, M. Okada, H. Mimura, Y. Inoue, Fabrication and mechanical properties of carbon nanotube yarns spun from ultra-long multi-walled carbon nanotube arrays, Carbon 50(12) (2012) 4579-4587.

[11] B.I. Yakobson, G. Samsonidze, G.G. Samsonidze, Atomistic theory of mechanical relaxation in fullerene nanotubes, Carbon 38(11–12) (2000) 1675-1680.

[12] E. Oh, H. Cho, J. Kim, J.E. Kim, Y. Yi, J. Choi, H. Lee, Y.H. Im, K.H. Lee, W.J. Lee, Super-Strong Carbon Nanotube Fibers Achieved by Engineering Gas Flow and Postsynthesis Treatment, ACS Appl. Mater. Interfaces 12(11) (2020) 13107-13115.

[13] L.M. Ericson, H. Fan, H. Peng, V.A. Davis, W. Zhou, J. Sulpizio, Y. Wang, R. Booker, J. Vavro, C. Guthy, A.N.G. Parra-Vasquez, M.J. Kim, S. Ramesh, R.K. Saini, C. Kittrell, G. Lavin, H. Schmidt, W.W. Adams, W.E. Billups, M. Pasquali, W.-F. Hwang, R.H. Hauge, J.E. Fischer, R.E. Smalley, Macroscopic, Neat, Single-Walled Carbon Nanotube Fibers, Science 305(5689) (2004) 1447.

[14] N. Behabtu, C.C. Young, D.E. Tsentalovich, O. Kleinerman, X. Wang, A.W.K. Ma, E.A. Bengio, R.F. ter Waarbeek, J.J. de Jong, R.E. Hoogerwerf, S.B. Fairchild, J.B. Ferguson, B. Maruyama, J. Kono, Y. Talmon, Y. Cohen, M.J. Otto, M. Pasquali, Strong, Light, Multifunctional Fibers of Carbon Nanotubes with Ultrahigh Conductivity, Science 339(6116) (2013) 182.

[15] H. Cho, H. Lee, E. Oh, S.-H. Lee, J. Park, H.J. Park, S.-B. Yoon, C.-H. Lee, G.-H. Kwak, W.J. Lee, J. Kim, J.E. Kim, K.-H. Lee, Hierarchical structure of carbon nanotube fibers, and the change of structure during densification by wet stretching, Carbon 136 (2018) 409-416.

[16] J. Lee, D.M. Lee, Y. Jung, J. Park, H.S. Lee, Y.K. Kim, C.R. Park, H.S. Jeong, S.M. Kim, Direct spinning and densification method for high-performance carbon nanotube

fibers, Nat. Commun. 10(1) (2019) 2962.

[17] Y. Jung, Y.C. Jeong, J.H. Kim, Y.S. Kim, T. Kim, Y.S. Cho, S.J. Yang, C.R. Park, One step preparation and excellent performance of CNT yarn based flexible micro lithium ion batteries, Energy Storage Mater. 5 (2016) 1-7.

[18] J. Choi, Y. Jung, S.J. Yang, J.Y. Oh, J. Oh, K. Jo, J.G. Son, S.E. Moon, C.R. Park, H. Kim, Flexible and Robust Thermoelectric Generators Based on All-Carbon Nanotube Yarn without Metal Electrodes, ACS Nano 11(8) (2017) 7608-7614.

[19] O.-K. Park, H. Choi, H. Jeong, Y. Jung, J. Yu, J.K. Lee, J.Y. Hwang, S.M. Kim, Y. Jeong, C.R. Park, M. Endo, B.-C. Ku, High-modulus and strength carbon nanotube fibers using molecular cross-linking, Carbon 118 (2017) 413-421.

[20] Y.S. Cho, H. Kim, M. Byeon, D.Y. Kim, H. Park, Y. Jung, Y. Bae, M. Kim, D. Lee, J. Park, K. Kang, D. Im, C.R. Park, Enhancing the cycle stability of Li–O2 batteries via functionalized carbon nanotube-based electrodes, J. Mater. Chem. A 8(8) (2020) 4263-4273.

[21] P.-X. Hou, B. Yu, Y. Su, C. Shi, L.-L. Zhang, C. Liu, S. Li, J.-H. Du, H.-M. Cheng, Double-wall carbon nanotube transparent conductive films with excellent performance, J. Mater. Chem. A 2(4) (2014) 1159-1164.

[22] K. Koziol, J. Vilatela, A. Moisala, M. Motta, P. Cunniff, M. Sennett, A. Windle, High-Performance Carbon Nanotube Fiber, Science 318(5858) (2007) 1892-1895.

[23] M.S. Dresselhaus, G. Dresselhaus, R. Saito, A. Jorio, Raman spectroscopy of carbon nanotubes, Phys. Rep. 409(2) (2005) 47-99.

[24] A.C. Ferrari, J.C. Meyer, V. Scardaci, C. Casiraghi, M. Lazzeri, F. Mauri, S. Piscanec, D. Jiang, K.S. Novoselov, S. Roth, A.K. Geim, Raman Spectrum of Graphene and Graphene Layers, Phys. Rev. Lett. 97(18) (2006) 187401.

Chapter 4 Effect of Crosslinking on Surface Nature of CNT Elementary bundles and Tensile Strength of CNTYs

4.1 Introduction

It has generally been understood that the mechanical properties of CNTY [1] highly depend on intrinsic surface nature of CNTs. CNTYs with high strength are thought to require void-free and defect-free materials with a high degree of alignment. However, CNT yarns produced through variety of methods have exhibited significantly poorer mechanical properties [2-11] than those of individual CNTs, which exhibit modulus as high as 1 TPa, strengths as high as 60 GPa [12, 13]. A variety of attempts has been made to minimize the discrepancy of mechanical properties between individual CNTs and CNT yarn through control of nanostructure, including properties of individual CNT such as number of walls, diameter [14] and length [15-19], as well as microstructural control, including bundling [20-24] and orientation [25] of CNT. Despite the variety of structural approaches, pristine CNT yarns still show poor properties due to interfacial slippage among CNTs.

The majority of recent progress are focusing on overcoming the weak interfacial interaction between CNTs for strengthening CNT yarn. Therefore, methods of improving interfacial strength by chemical crosslinking between CNTs were introduced [26-28]. This method introduces stronger interaction than van der Waals interaction between CNTs, expected to result in improved mechanical properties [29]. However,

such methods reported limited strength increment without revealing the main cause of results. Therefore, it is highly desirable to investigate on the influential parameters in order to define the correlation between the effect of crosslinking and the mechanical properties of CNT yarn.

In this chapter, we suggest a simplified model of crosslinked CNT yarn to predict the main factors influencing the strength of the yarn. Based on the model assuming strength as a function of contact area of CNT and interfacial shear strength of CNT, we transformed such model into function of degree of reaction, resulting main factor influencing strength as bending rigidity from curvature energy and surface energy changed by linking reagent. To verify the model, simple method of crosslinking was hired, based on carbon surface chemistry. By giving variety to linking reagent or degree of reaction and analyzing junction of linking reagent and surface of CNT from reaction, we found out developed model fitted well to experimental data, giving basis to the model as well as insight to the strategy to strengthen CNTY. Applying the model, finally, we found crosslinking by 1,3-dipolar cycloaddition reaction strengthened CNTY up to 5.4 N/tex with 20% increment from DW-SA-6 of chapter 3, which is 93% of estimated maximum strength achievable.

4.2 Experimental

Materials

Ferrocene, thiophene, maleic anhydride, 2,2′-(ethylenedioxy)bis(ethylamine), 4,7,10-trioxa-1,13-tridecanediamine, ethylene glycol (EG) and diiodomethane (DIM) were purchased from Sigma-Aldrich. Dimethyl sulfoxide (DMSO), acetone and ethylenediamine were purchased from Daejung Chemical and Metals. 1,5-diaminopentane was purchased from Alfa Aesar. N,N'-dimethyl-1,3-propanediamine and pyrrole-2-carboxaldehyde were purchased from Tokyo Chemical Industry Co., Ltd. All materials were used as received without further purification.

Synthesis of DWCNTs and DWCNT yarns

CNT yarns were fabricated through a direct spinning method as our previous report [21, 27, 30-33]. Diels-Alder cycloaddition reaction of CNT yarns were proceeded by soaking CNT yarns in primary diamines (0.5~50 mM) and maleic anhydride (two equiv.) dissolved 110 ml of DMSO solution at 180 °C for 24 h. 1,3-dipolar cycloaddition reaction of CNT yarns were proceeded by soaking CNT yarns in N,N'-dimethyl-1,3-propanediamine (10~200 mM) and pyrrole-2-carboxaldehyde (two equiv.) dissolved 100 ml of DMSO solution at 120 °C for 24 h. Then CNT yarns were washed with acetone for several times to remove unreacted and adsorbed reagents.

Characterization of CNT yarns

The nanostructure of CNTs was characterized with HR-TEM (JEM-2100F, JEOL) and Raman spectroscopy (RAMANplus, Nanophoton) using 532 nm laser. Thermal gravimetric analysis (TGA; SDT-Q600, TA Instruments) was used to measure degree of reaction in N2 atmosphere and the purity of CNTs in air atmosphere. Chemical characteristic was evaluated by X-ray photoelectron spectroscopy (XPS; AXIS-HSi, KRATOS) and elemental analyzer (Flash EA 1112, Thermo Electron Corporation). Contact angle measurement (SmartDrop plus, Femtobiomed) was used to measure surface energy of CNT. The internal structures of the CNT yarn were observed after cutting with a focused ion beam (FIB; Helios 650, FEI). Specific strength was calculated by linear density, which was determined by weighing 15 m long-CNT yarn, divides into a measured load of a single yarn with tensile stage (TST350, Linkam) at a gauge length of 10 mm and strain rate of 3 mm min^{-1}.

Computation details

Monte Carlo (MC) simulations of linking reagents and CNT adsorptions were performed to calculate the preferential adsorption site and the interaction energy on various CNTs: SWCNT, DWCNT and MWCNT of which the number of wall is 8. All CNTs had their innermost wall as (30, 30) armchair type. Prior to MC simulations, each adsorbent structure was fully optimized by Forcite module in a Material Studio 8.0 platform. COMPASS (condensed phase optimized molecular potentials for atomistic simulation studies) forcefield was applied in all the calculations. The interaction energy for the adsorbates were identified by the simulated annealing algorithm.

4.3 Result and discussion

CNTs were synthesized by floating catalyst chemical vapor deposition (FCCVD) as previous method in chapter 3. Single-walled (SW), double-walled (DW) and multi-walled (MW) CNT were synthesized to identify the effect of crosslinking. According to the TGA thermogram in Fig. 4.1a, c and e, each CNTY is composed of 40 wt% SWCNT, 70 wt% DWCNT and 80 wt% MWCNT [34]. From TEM analysis in Fig. 4.1b, d and f, the outer radius of SWCNT, DWCNT and MWCNT was 2.58 nm, 2.78 nm and 5.19 nm, respectively. (The number of wall of MWCNT was around 8.)

The strength of synthesized CNT yarn mainly depends on CNT-CNT interaction (shear strength). In order to strengthen the yarn, the degree of crosslinking should be considered. Since CNT is reported as inert material due to aromaticity, appropriate chemical reaction should be employed. Normally, the molecular structure of CNT is expressed as clar representation form as shown in Fig 4.2. Since the structure consists of resonance form, there are mainly two more molecular structure that presents the chemical character of CNT; diene and dienophile form. Also, since there is no hydrogen on CNT to balance charge during reaction, electrophilic aromatic substitution is unsuitable. Therefore, such interpretations indicate that suitable chemical reaction for CNT involves diene or dienophile without charge, which is cycloaddition reaction [35, 36].

To quantify the reaction, Degree of reaction (x) was defined as equation (4.1), where v is linear density of yarn and M is molecular weight of linking reagent.

$$x = \frac{\Delta v}{v} \times \frac{1}{M} \tag{4.1}$$

For comparison under same conditions, number of linking reagents grafted on surface of CNT should be controlled. Since all linking reagents from crosslinking reaction are designed to contain nitrogen atom, N/C ratio shows amount of linking reagent reacted with CNT surface. Since degree of reaction showed linear relationship N/C ratio from elemental analysis shown in Fig. 4.3, degree of reaction is suitable for independent variable.

$$\frac{\sigma_x}{\sigma_0} = \frac{1}{\Omega_{mib}} \times \left[1 - (1 - \Omega_{mib}) \sqrt{\frac{1 + Cx}{1 + Bx}} \right] \times (1 + Dx) \tag{4.2}$$

Since crosslinking is performed between elementary bundles in microbundle due to the size of the linking reagent, it should be analyzed based on equation (2.24), which expresses the behavior of the elementary bundle. Considering the term ω is proportional to degree of reaction (x), equation (2.24) is simplified into equation (4.2). The difference in linear density (Δv) of yarn after crosslinking is not large enough, the influence of Δv on is σ_x neglected. According to the equation, the coefficient B, C and D indicate $\Delta\gamma$, ΔD_G and $\Delta\tau$, respectively.

In order to find out the criterion to determine whether crosslinking reaction results in monotone increasing strength in function of degree of reaction, equation 10 was

differentiated by degree of reaction. To achieve monotone increasing function, differentiated form should be greater than 0 for any x. In case of ideally strengthened CNT yarn, its strength will be increasing even at infinite x given as following equation.

$$\lim_{x \to \infty} \frac{d}{dx}\left(\frac{\sigma_x}{\sigma_0}\right) \geq 0; \quad \frac{B}{(1 - \Omega_0)^2} - C \geq 0 \tag{4.3}$$

Equation (4.3) indicates the criterion to achieve high strength CNT yarn; decreasing ΔD_G as well as increasing $\Delta\gamma$ is required. In terms of material and reaction factor, high $\Delta\gamma$ can be achieved by linking reagent with high polar character, while low ΔD_G can be achieved by junction between CNT and linking reagent with low distortion energy loaded on the surface of CNT from crosslinking reaction.
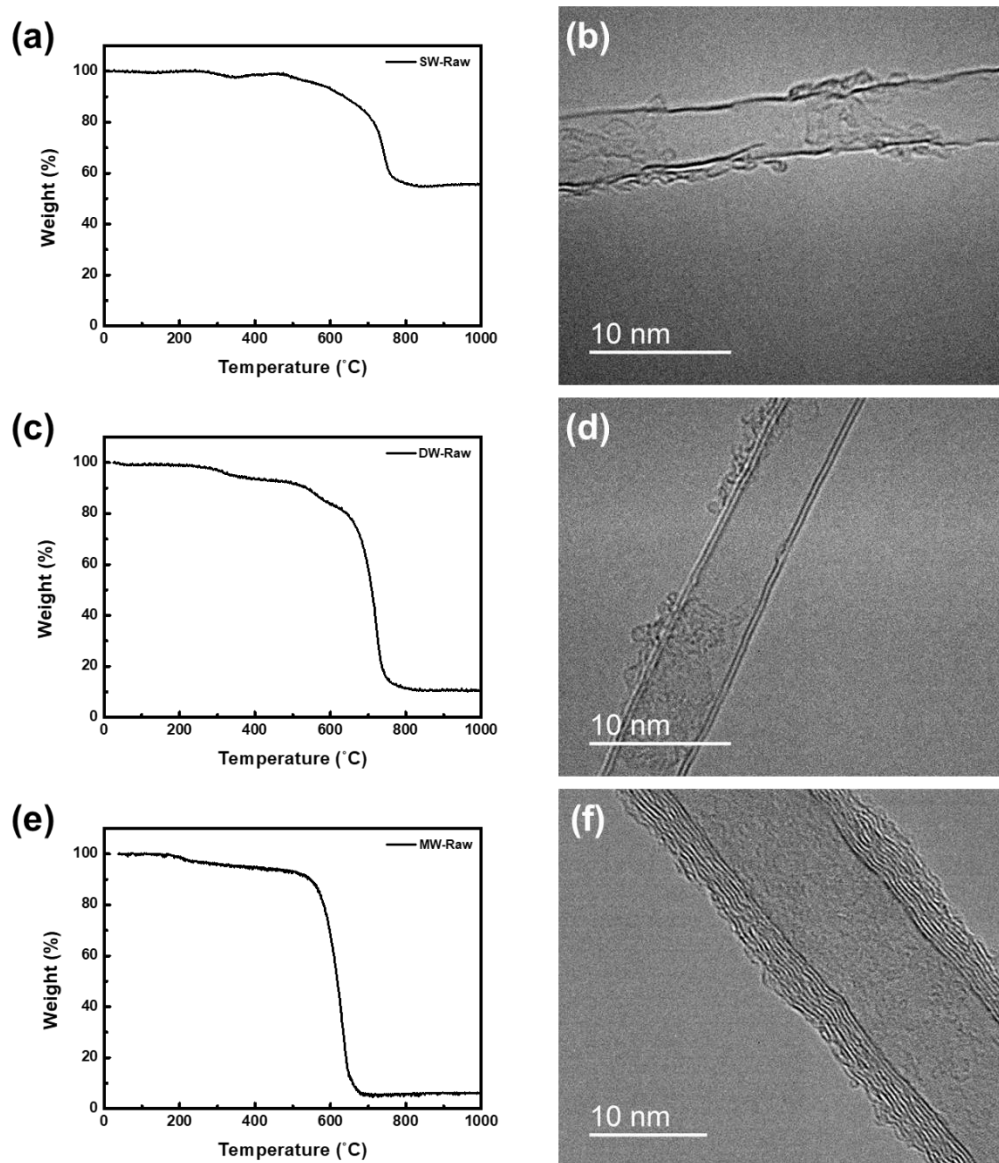
Fig. 4.1. (a, c, e) TGA thermogram and (b, d, f) TEM micrograph of (a, b) SWCNT, (c, d) DWCNT and (e, f) MWCNT.

<Diene>   **<Clar>**   **<Dienophile>**
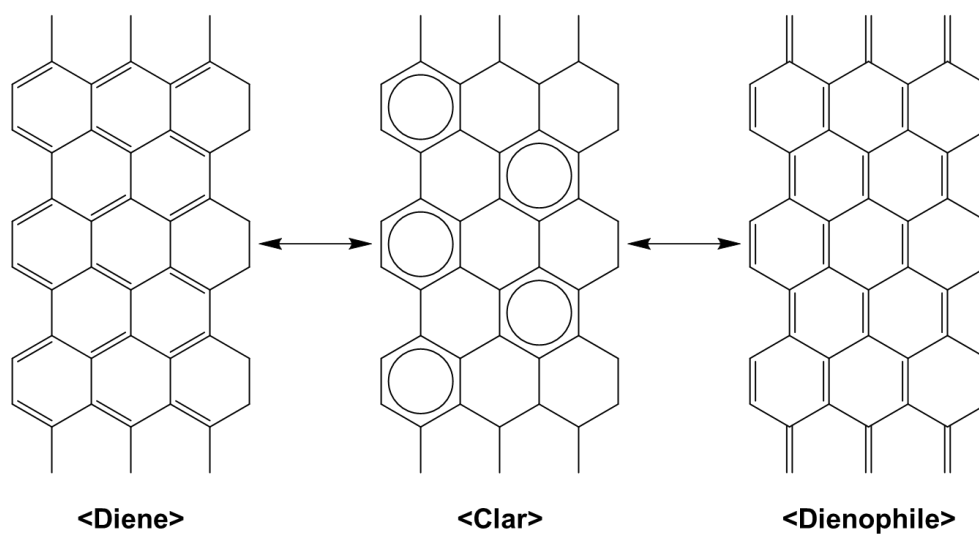
Fig. 4.2. Carnonical resonance structures of graphene.
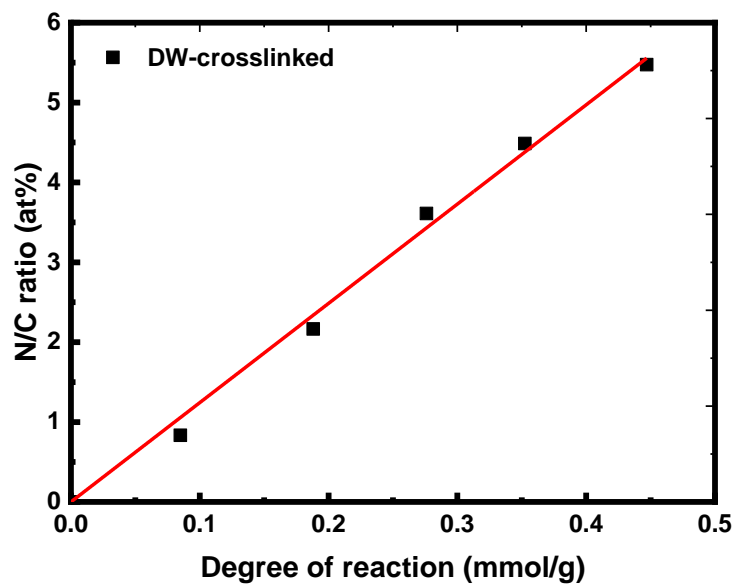
Fig. 4.3. N/C ratio versus degree of reaction for crosslinked DWCNT yarn.

4.3.1 Empirical verification of crosslinking theory

In order to identify the effect of surface energy, we designed crosslinking reaction based on Diels-Alder cycloaddition, which is known to be favorable reaction with π-conjugated system according to carbon surface chemistry. The detailed mechanism of reaction is presented in Fig 4.4a. First, linking reagents were vitalized by forming bisimide complex from diamine molecule with two equivalents of maleic anhydride. Then, covalent bonds between CNT surface and bisimide complex were formed through cycloaddition. As shown in Fig 4.4b-i, bisimide complex from ethylenediamine, 1,5-diaminopentane, 2,2′-(ethylenedioxy)bis(ethylamine) and 4,7,10-trioxa-1,13-tridecanediamine were named A2, A5, A8 and A13 respectively. CNT yarn crosslinked by such complex was named (SW, DW, MW)-(A2, A5, A8, A13). For example, DWCNT yarn crosslinked by A2 was named DW-A2. Pristine CNT yarns were named (SW, DW, MW)-Raw.

XPS analysis was performed to obtain the information of chemical nature of DWCNT yarns as a representative of other samples. Various forms of carbon atoms quantitatively calculated from C 1s and spectral deconvolution provided in Fig 4.5a-c. The ratio of oxidative carbon atoms related to linking reagent, C-O/C-N, C=O and COOH/imide, increased in DW-A2 compared to DW-Raw. As cycloaddition reaction proceeds, ratio of sp3 carbon increases with oxidative carbons due to reaction mechanism. In addition, spectral deconvolution N 1s peak provides formation of imide functional groups that only appear in vitalized linking reagent by forming bisimide complex. Such analysis indicates both imide formation and crosslinking by cycloaddition are well proceeded.

According to come preceding studies, imide derivative functional groups get decomposed starting at approximately 300 ˚C [33, 37], indicating that the reduction in mass is from crosslinking on CNTs. Based on mass reduction, the degree of reaction

could be calculated as 0.32 mmol/g for DW-A2, which fits well to the result (0.35 mmol/g) calculated from equation (4.1).
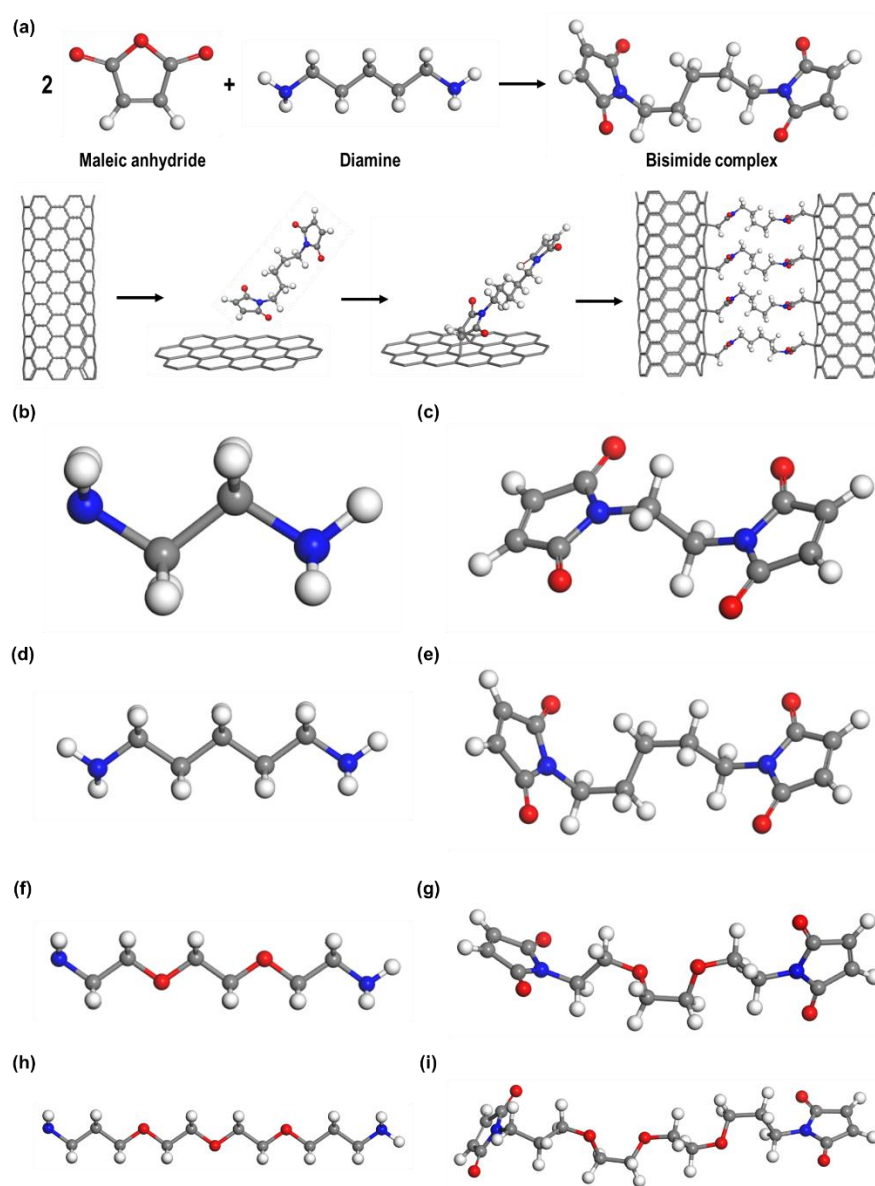
Fig. 4.4. Schematic image of (a) mechanism of formation of bisimide complex with Diels-Alder cycloaddition on the surface of CNTs, (b) ethylenediamine, (c) A2, (d) 1,5-diaminopentane, (e) A5, (f) 2,2′-(ethylenedioxy)bis(ethylamine), (g) A8, (h) 4,7,10-trioxa-1,13-tridecanediamine and (i) A13.
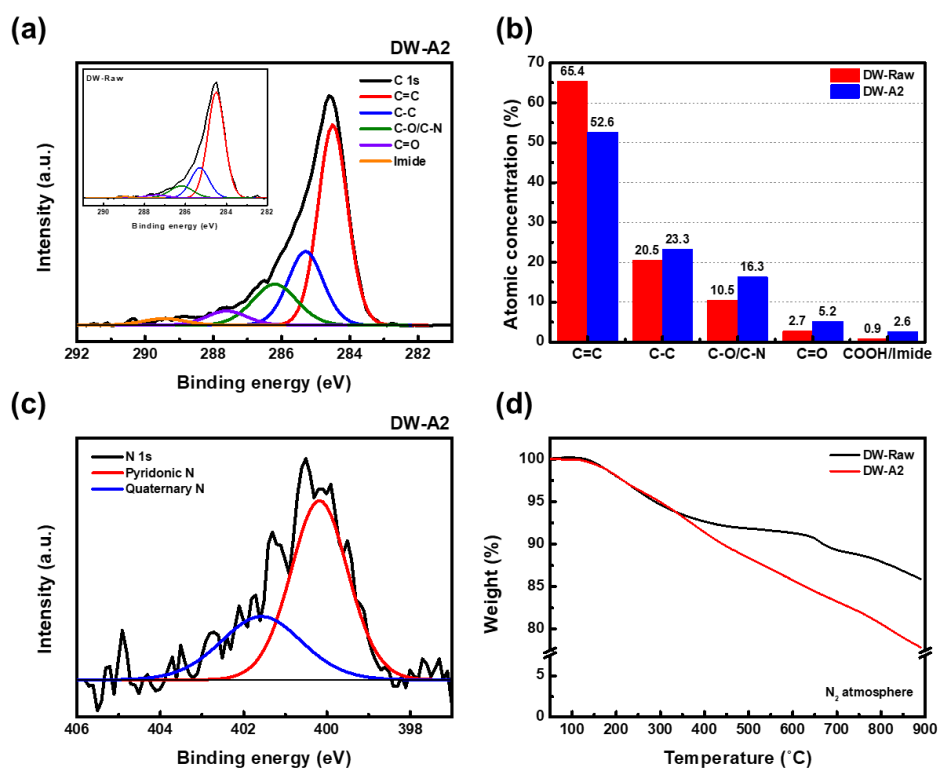
Fig. 4.5. XPS spectra of (a) C 1s of DW-A2 (inset: C 1s of DW-Raw), (b) Quantitative analysis of carbon forms by XPS and (c) N 1s of DW-A2. (d) TGA data of DW-Raw and DW-A2 at N_2 atmosphere.

4.3.1.1　　Surface area fraction of elementary bundle in contact

Under same degree of reaction of 0.35 mmol/g, among various linking reagents, A5 for SW, MWCNT yarn and A2 for DWCNT yarn showed highest mechanical strength. In Fig 4.6a-f, SW-A5, DW-A2 and MW-A5 displayed 1.55, 2.41 and 2.17 N/tex of specific strength from that of SW, DW and MW-Raw which are 0.77, 0.97 and 0.96 N/tex, respectively. Each crosslinked yarn showed increment of 101%, 148% and 134% from pristine yarn, indicating effect of crosslinking. To verify that the model is well grounded, equation (4.2) was applied to experimental values of strength ratio for each sample as shown in Fig. 4.6g-i. The strength of yarn was normalized in consideration of linear density change. The graph shows clearly that the equation fits well to experimental data, resulting coefficient values in Table 4.1. The empirical Ω_{mib} of SWCNT, DWCNT and MWCNT yarn was 0.83, 0.67 and 0.53, respectively. We also calculated the theoretical Ω_{mib} from equation (2.19) by applying structure values of CNTs we used. As a result, the area fractions of SWCNT, DWCNT and MWCNT yarn were 0.73, 0.66 and 0.57, respectively. Since empirical Ω_{mib} of CNTY well fitted with the theoretical Ω_{mib} as shown in Table 4.1, it is suitable to analyze CNTY with model from equation (4.2).
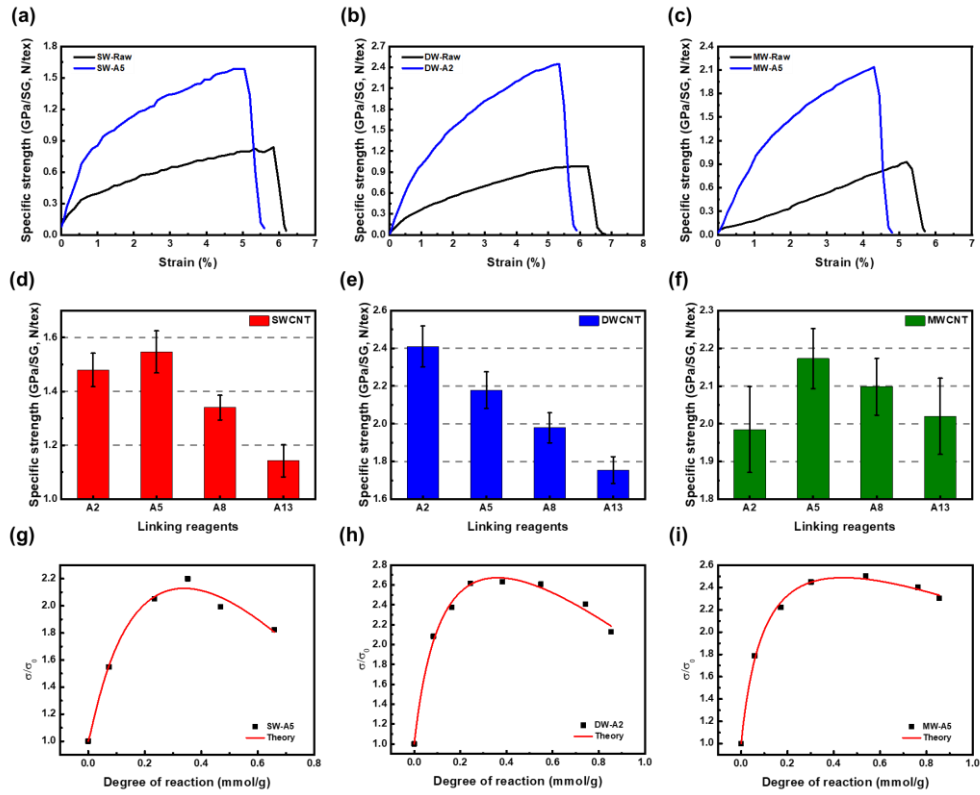
Fig. 4.6. Stress-strain curve of (a) SW-A5, (b) DW-A2 and (c) MW-A5. Mechanical properties of (d) SWCNT, (e) DWCNT and (f) MWCNT yarn. Comparison of theoretical and experimental values of strength ration versus degree of reaction for (g) SW-A5, (h) DW-A2 and (i) MW-A5.

Table 4.1. Theoretically calculated Ω_{mib} with coefficient values of equation (4.2).

Sample	Ω_{mib} (Theoretical)	Ω_{mib} (Experimental)	B (g/mmol)	C (g/mmol)	D (g/mmol)
SW-A5	0.73	0.83	2.2	100	19
DW-A2	0.66	0.67	4.8	48	32
MW-A5	0.57	0.53	7.1	32	32

4.3.1.2 Coefficient *B*: surface energy (*Δγ*)

For prediction of high strength CNTY, investigation of each factor is required. First, to find out how coefficient *B*, which indicates *Δγ*, affects the strength, surface energies of DW-Raw and DW-A2 were calculated through Owen-Wendt method [38]. According to Owen-Wendt method, surface energy is divided into dispersion (γ^D) and polar (γ^P) component. From the contact angle (*θ*) between solid and probe liquid, the surface energy of solid (γ^s) can be determined by the surface energy of solid(γ^l) with following equation (4.4).

$$\frac{\gamma_l(cos\theta + 1)}{2\sqrt{\gamma_l^D}} = \sqrt{\gamma_s^P}\left(\frac{\sqrt{\gamma_l^P}}{\sqrt{\gamma_l^D}}\right) + \sqrt{\gamma_s^D} \tag{4.4}$$

When the square root of polar (γ_s^P) and dispersion (γ_s^D) component of the surface energy of solid on the right side are taken as slope and intercept, respectively, the equation (4.4) has the linear form in terms of surface energy of probe liquids and contact angle. Water, EG, DMSO and DIM were used as probe liquid for containing contact angles. Detailed information of surface energy of each liquid is shown in Table 4.2.

Fig. 4.7a-h shows the images of contact angle of probe liquids deposited on CNT films; DW-Raw (*x* = 0 mmol/g) and DW-A2 (*x* = 0.54 mmol/g). Since EG and water were used as the polar component dominant probe, as crosslinking reaction proceeds, the contact angle decreases due to increment of polar surface energy of CNT film. It is clearly shown in Fig. 4.7i-j and Table 4.2 that polar component as increased by 3.9 times. According to

135

equation (4.2), the term $(1+Bx)$ indicates the surface energy ratio of after to before reaction. By applying x to 0.54 mmol/g and B to 4.8 g/mmol from Table 4.1, the calculated surface energy ratio is 3.6, which fits well to actual ratio of polar component of DW-A2 to that of DW-Raw. The functional groups in crosslinking reagent works as mechanical locker by dissipating energy from external load. Since the functional groups shows polar character rather than dispersive character, the dissipated energy is related to polar component of surface energy, indicating the term $(\Delta\gamma/\gamma)_{graphene}$ in equation (2.24) should be $(\Delta\gamma_{polar}/\gamma_{polar})_{CNT}$ in specific.
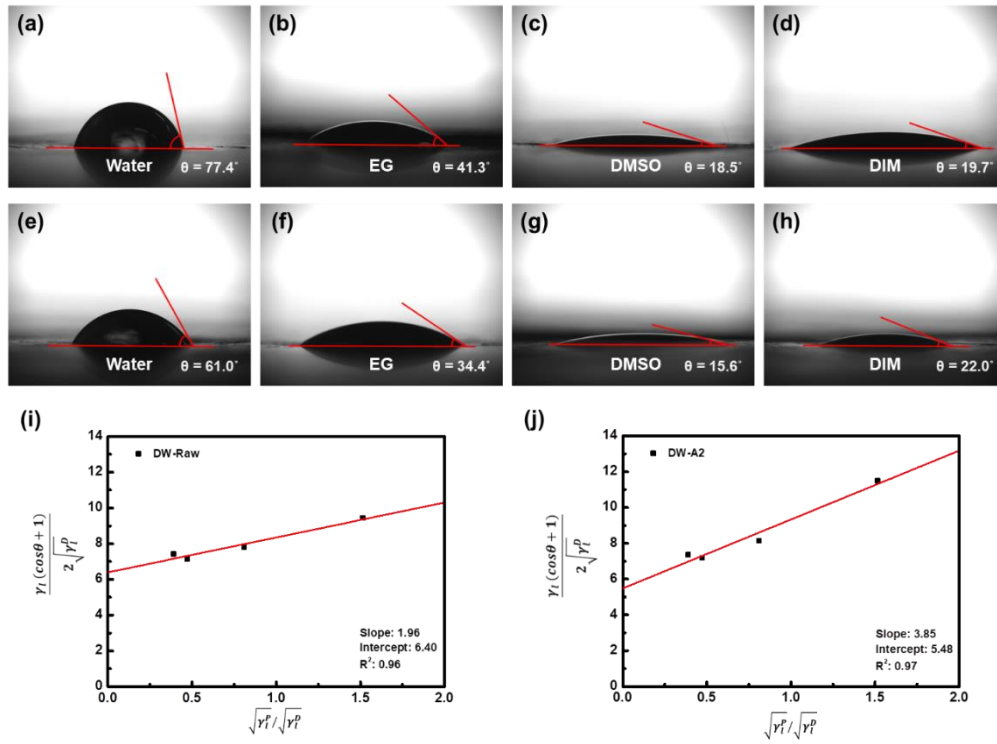
Fig. 4.7. Contact angle of probe liquid droplets deposited on (a-d) DW-Raw and (e-h) DW-A2 film. Owen-Wendt plot of (i) DW-Raw and (j) DW-A2 film.

Table 4.2. Surface energies of CNT films (unit: mJ/m^2).

Sample	Dispersion	Polar	Total
DW-Raw	40.9	3.8	44.7
DW-A2	30.1	14.8	44.9

To specify which factors could influence $\Delta\gamma_{polar}$, linking reagents with various interaction energy to pristine CNT were hired to analyze their relation to strength of crosslinked CNTY. Adsorption energy was calculated by probability density function (Figure S3) from COMPASS forcefield. As shown in Fig. 4.8a-c, strength and affinity between CNT and linking reagent showed similar tendency. When magnitude of adsorption energy of linking reagent to CNT decreases, strength of the fiber increases. Such phenomena can be explained by following equation (4.5).

$$\Delta\gamma = \Delta\gamma_{defect} + \Delta\gamma_{adsorption} \qquad (4.5)$$

Variation of surface energy after reaction can be mainly described as sum of two terms; increase term from defect formation and decrease term from interaction between linking reagent and surface of CNT. Since all reactions are equivalent, same Diels-Alder cycloaddition and same degree of reaction, $\Delta\gamma_{defect}$ term is expected to show little difference. Therefore, second term $\Delta\gamma_{adsorption}$ is mainly determining $\Delta\gamma$ and strength of the yarn. Smaller magnitude of $\Delta\gamma_{adsorption}$ leads to higher value of $\Delta\gamma$ and the strength. It also indicates that surface of CNT is stabilized through interaction with linking reagents. They drive force to make contact between CNTs smaller, leading to lower value of Ω_x. Furthermore, Raman peak shifts of DWCNT yarn crosslinked with various linking reagents are provided in Fig. 4.8d. Raman peak shift is reflecting the inter-nanotube interaction and contact area. Orthogonal electronic dispersion occurs when CNTs are in contact each other and peaks shift to lower energy [39-41]. To be specific, DW-A2, which showed highest strength among other samples, showed Raman G' peak shift from

138

2697.1 cm^{-1} of DW-Raw to 2680.8 cm^{-1}. It is much lower value compare with DW-A5, 8 and 13. G' peak shift of Raman spectra reveals DW-A2 has larger contact area between CNTs, in good agreement with the relation between adsorption energy of linking reagent to CNT and the strength of the CNTY.
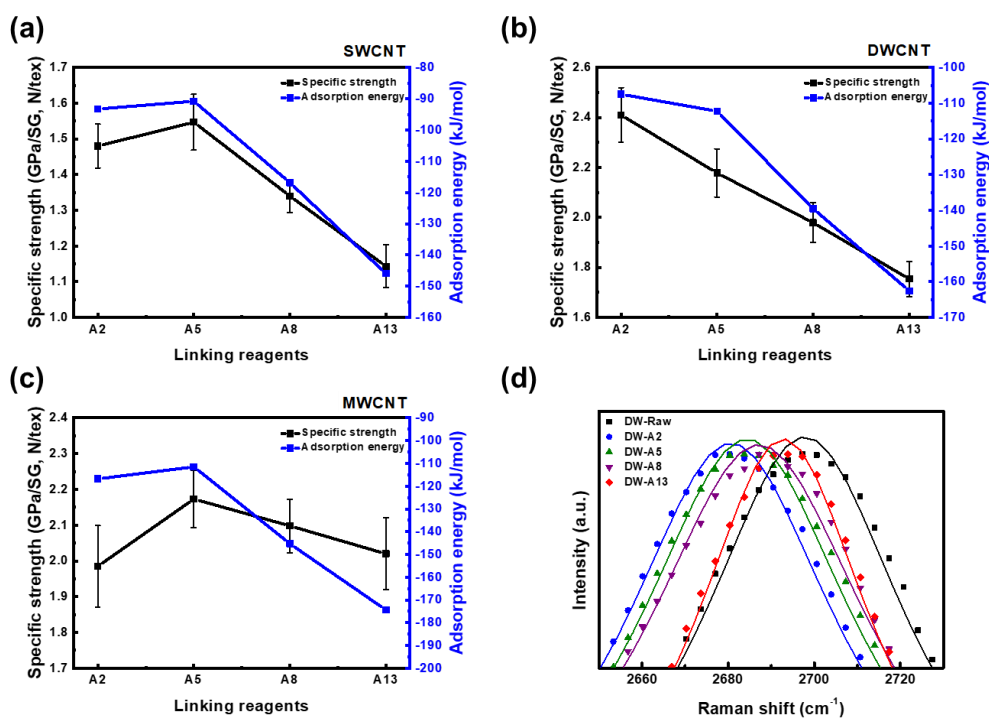
Fig. 4.8. Comparison of specific strength of CNTY strengthened by various linking reagents at degree of reaction of 0.3 mmol/g and adsorption energy of linking reagent to CNT: (a) SWCNT, (b) DWCNT and (c) MWCNT. (d) Raman spectra of G' peak (symbol) and fitted using a Lorentzian function (solid line) of DWCNT yarn crosslinked with various linking reagents.

4.3.1.3   Coefficient C: curvature energy (ΔD_G)

Another term of the equation (2.24), ΔD_G, is determined by type of reaction. According to Table 4.1, coefficient C is much higher than other coefficients in every sample, indicating it is most critical factor determining the form of graph. Since bending rigidity is resistance offered by a structure while undergoing bending, the junction type of linking reagent and surface of CNT is another key factor determining the intensity of coefficient C and strength of the CNTY. To verify the term affecting coefficient C, we selected representative junctions that CNTs and linking reagents could have based on carbon surface chemistry, and calculated the distortion energy generated when the junctions were given to CNTs.

As shown in Fig. 4.9 and Table 4.3, we calculated the distortion energy applied to the CNTs when several ring type junctions were formed on the CNT surface through forcite module. The distortion energy from point type junction showed the lowest value (149.3 kJ/mol) among junctions. Cycloaddition reaction inevitably forms ring composed of sp^3 carbon. Such ring structure is similar to structure of diamond, which is reported to have infinitely higher curvature energy compared to graphene. Although such ring forming cycloaddition reaction is favorable to react with chemically inert π-conjugated system composed of sp^2 carbon according to carbon surface chemistry, bending rigidity from ring type junction is inevitably larger than that from point type junction. The coefficient C of crosslinked CNTY of which junction was trapezoid type was about 30~100, while the largest distortion energy came from trapezoid type (673.8 kJ/mol), 4.5 times larger than that of point type. Such calculation results support why the specific strength of crosslinked CNT yarn eventually decreases as the degree of reaction increases.
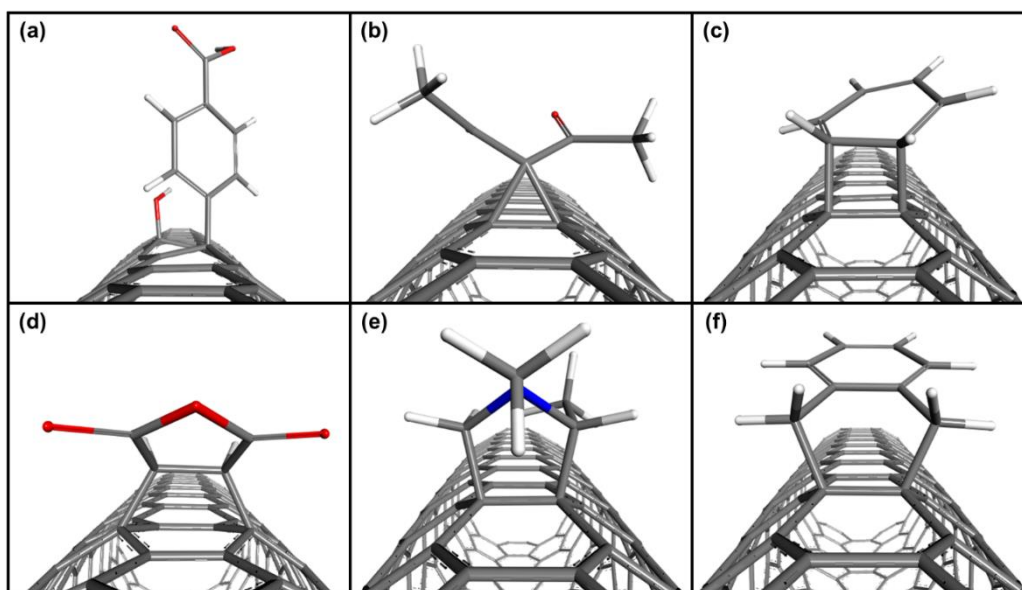
Fig. 4.9. Schematic illustration of junction type: (a) point, (b) triangle, (c) tetragon, (d) trapezoid, (e) pentagon and (f) hexagon.

Table 4.3. Distortion energy on CNT given by various types of junctions.

Junction type		CNT distortion energy (kJ/mol)
Point	(a)	149.3
Triangle	(b)	621.8
Tetragon	(c)	296.9
Trapezoid	(d)	673.8
Pentagon	(e)	194.7
Hexagon	(f)	187.5

4.3.2   Fabrication of high strength CNTY

4.3.2.1   Determination of crosslinking reaction and linking reagent

According to verification of model, the linking reagent requires polar character with chemical ability to form pentagonal or hexagonal junction with CNT. Thus, we adapted 1,3-dipolar cycloaddition reaction, which is one of favorable for reaction with π-conjugated system. The detailed mechanism of reaction is presented in Fig. 4.10. First, linking reagents were vitalized by forming dipolar complex from secondary diamine molecule with two equivalents of aldehyde. Then, covalent bonds between CNT surface and dipolar complex were formed through 1,3-dipolar cycloaddition. We selected N,N'-dimethyl-1,3-propanediamine as secondary diamine molecule while pyrrole-2-carboxaldehyde was selected as aldehyde since such molecule is able to stabilize dipolar complex by π-conjugation with its polar character. The crosslinked DWCNT yarn was named DW'-B3. Pristine CNT yarns were named DW'-Raw. For comparison with the previous reaction, the strength of pristine CNTY was adjusted to a similar scale.

As shown in Fig. 4.11a, the specific strength of DW'-Raw was 1.67±0.11 N/tex while the specific strength of DW'-B3 was 4.43±0.21 N/tex at the degree of reaction of 0.44 mmol/g. The crosslinking was done until the solubility limit of the linking reagent. Through the designed crosslinking, the specific strength showed increment of 165% from pristine yarn. The specific strength of our work even surpassed that of carbon fiber T1100 (~3.9 GPa/(g cm^{-3})), which is known as one of the strongest fiber recently.

XPS analysis was performed to obtain the information of chemical nature of DWCNT yarns in Fig 4.11c. Spectral deconvolution N 1s peak provides formation of pyrrolic N and tertiary amine with the residual peak of pyridinic N. Pyridinic N is formed when linking reagent is activated by forming dipolar complex and converts to tertiary amine

when the linking reagent reacts with the CNT surface. Since the pyrrolic N and tertiary amine peak account for 93.5% of N1s peak while pyridinic N account for 6.5%, such analysis indicates that both ends of most linking reagents reacted with CNTs and crosslinking by cycloaddition are well proceeded. TEM image of DW'-B3 is shown in Fig. 4.11d, after chemical modification. After 1,3-dipolar cycloaddition reaction, organic layer was deposited on the surface of CNT, indicating grafting of linking reagents.

Furthermore, change in deformation behavior of CNTs after reaction was analyzed through in situ Raman spectroscopy during tensile strain to confirm crosslinking. Raman band is strongly resonant under deformation of CNTs and down shift rate of G' peak implies load transfer efficiency between CNT with neighboring CNTs [39, 42]. Higher load transfer efficiency guarantees effective dissipation of applied stress and interferes breakage of CNT yarn by stress concentration through linking reagent. In Fig. 4.11e-f, the results of downshift rate exhibited DW'-B3 showed load transfer efficiency as high as -21.9 cm^{-1}/%, almost twice higher than that of DW'-Raw. It implies DW'-B3 has mechanically more favorable structure since it successfully dissipated applied stress evenly through crosslinked regions.

Also, to verify that the model is well grounded even with the change of chemical reaction, equation (4.2) and (4.3) were applied to experimental values of strength ratio as shown in Fig. 4.11b. The graph shows clearly that the equation fits well to experimental data, resulting coefficient values in Table 4.4. The empirical Ω_{mib} of DW'-B3 yarn was 0.68, well matched with empirical Ω_{mib} of DW-A2 and theoretical Ω_{mib} of DWCNT of given structure values. Due to pentagon type junction from the 1,3-dipolar cycloaddition reaction, less distortion energy was loaded to CNT, leading to less increase in bending rigidity (coefficient C). Furthermore, with N based functional groups and

charge on dipolar complex, its polar character led to CNT-phobic nature with sufficient increase in surface energy (coefficient B). As a result, criterion of DW'-B3 from equation (4.3) was positive value, indicating the specific strength of DW'-B3 monotonically increases as degree of reaction increases.
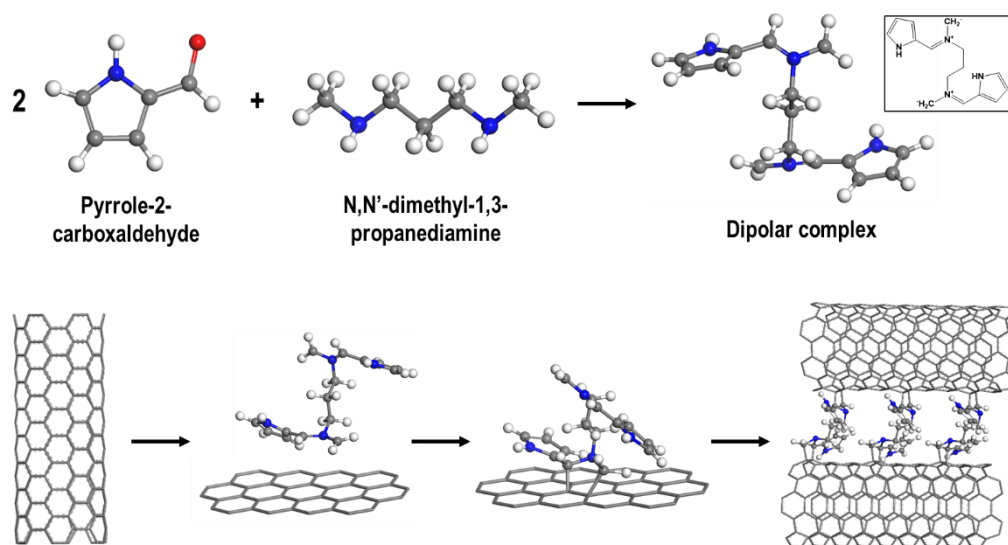
Fig. 4.10. Schematic image of mechanism of formation of dipolar complex with 1,3-dipolar cycloaddition on the surface of CNTs.
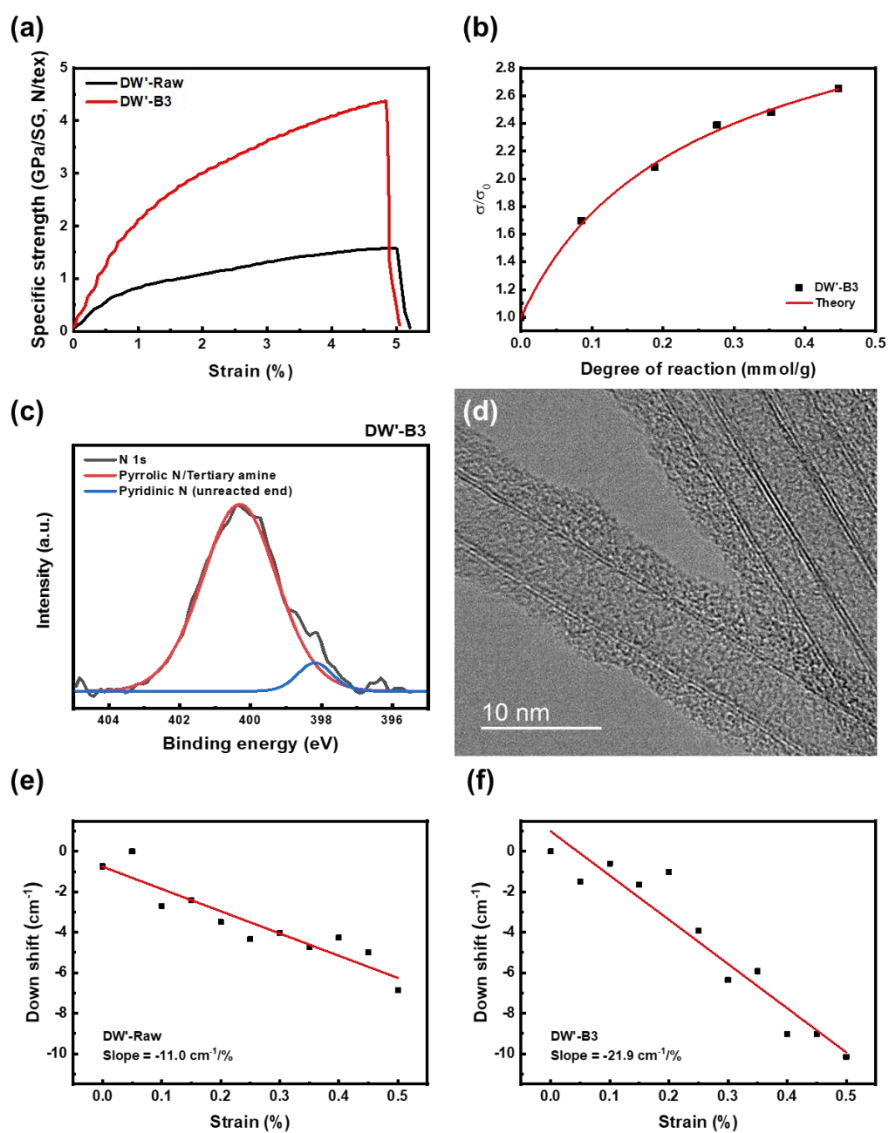
Fig. 4.11. (a) Stress-strain curve of DW'-Raw and DW'-B3. (b) Specific strength increase ratio. (c) XPS spectra of N 1s of DW'-B3. (d) TEM image of DW'-B3. Down shift rate of G' peak of (e) DW-Raw and (f) DW-A2 during tensile loading (Symbols and red solid lines are raw data and linear fitting).

Table 4.4. Coefficient values of equation (4.2) and criterion equation (4.3) for DW-A2 and DW'-B3.

Sample	Ω_{mib} (Experimental)	B (g/mmol)	C (g/mmol)	D (g/mmol)	$\dfrac{B}{(1-\Omega_0)^2} - C$
DW-A2	0.67	4.8	48	32	<0
DW'-B3	0.68	3.8	35	19	>0

4.3.2.2   Ultra-high strength crosslinked CNTY

Through the previous analysis, the possibility of fabrication of ultra-high strength fibers through 1,3-dipolar cycloaddition reaction was confirmed. Thus, we crosslinked DW-SA-6 from chapter 3 by dipolar complex same as DW'-B3. At the degree of reaction of 0.45 mmol/g, crosslinked CNTY, which will be named as DW-X-6, showed specific strength of 5.4±0.1 N/tex with specific stiffness of 225.7±34.4 N/tex (Fig. 4.12). Our results reached the previously reported maximum specific strength [43], which surpassed the carbon fiber T1100 (~3.9 N/tex), known as one of the strongest fibers in recent times. The results state that the specific strength of the CNTY was increased by 20% through designed crosslinking reaction. Also, the specific stiffness of CNTY was increased by 60%, well matched with *in-situ* Raman analysis of Fig 4.11e-f.

For crosslinked yarn, external load should exceed the bond energy of covalent bonds in the linking reagent to reach failure. Even if the linking reagent consists of aromatic ring, the molecular structure is bound to have single bond where the final failure occurs. Therefore, regardless of the type of linking reagent, covalent bond energy hardly makes any difference, indicating $\Delta\tau$ should be approximated as a fixed value. If the number of wall of CNT is same, the multiplication between specific strength of as-spun yarn (σ_0) and coefficient D would be a fixed value. Based on DW'-B3, DW-A2, SW-A5 and MW-A5, $\sigma_0 D$ of CNTY converged to 31. Applying calculation to equation (4.2), empirically estimated value of strength of crosslinked yarn can be given as equation (4.6).

$$\sigma_{x=0.45} = \frac{1}{\Omega_{mib}} \left[1 - (1 - \Omega_{mib}) \sqrt{\frac{1 + Cx}{1 + Bx}} \right] \{\sigma_0 + (\sigma_0 D)x\} \tag{4.6}$$

$$\approx 0.29\sigma_0 + 4.1$$

When the crosslinking reaction, which is 1,3-dipolar cycloaddition, is applied with degree of reaction of 0.45 mmol/g, the estimated strength becomes linear function of strength of as-spun yarn. The maximum strength (σ_{max}) is determined when σ_0 becomes equal to $\sigma_{x=0.45}$. Through the 1,3-dipolar cycloaddition, σ_{max} achievable is calculated as 5.8 N/tex. Though our result has achieved up to 93 % of the maximum value, with stronger CNTY would have reached even closer value to maximum strength.

$$\sigma_{est} = \frac{1}{0.32} \left[1 - 0.68 \times \sqrt{\frac{1 + 35x}{1 + 3.8x}} \right] (\sigma_0 + 31x) \tag{4.7}$$

Furthermore, by applying calculated coefficients to modified equation (2.24) and (4.2), we empirically derived universal equation (4.7) of strength of DWCNT yarn against initial strength and degree of reaction. To verify that the equation is well grounded, strength of DW-X series and DW'-B3 series were applied to theoretically estimated strength as shown in Fig. 4.13. The graph shows clearly that the equation fits well to experimental data. Such results states that upper limit of strength will be higher as the initial strength increases.

The specific strength, specific stiffness, and elongation of CNTYs were compared with those of various state-of-the-art high-performance fibers and metals from industry (Fig. 4.14). Even the commercialized state-of-the-art materials do not possess both high specific tensile strength and elongation. Our CNTY has high-average specific tensile strength (5.4 N/tex) as well as high-elongation (5.8 %) with superfiber class modulus (226 N/tex).

However, our results show that the efficiency of the reaction is somewhat inferior. Therefore, for higher maximum specific strength, according to our theory, new crosslinking reaction inducing point junction with high degree of reaction as well as linking reagent with low affinity to CNT will be required.
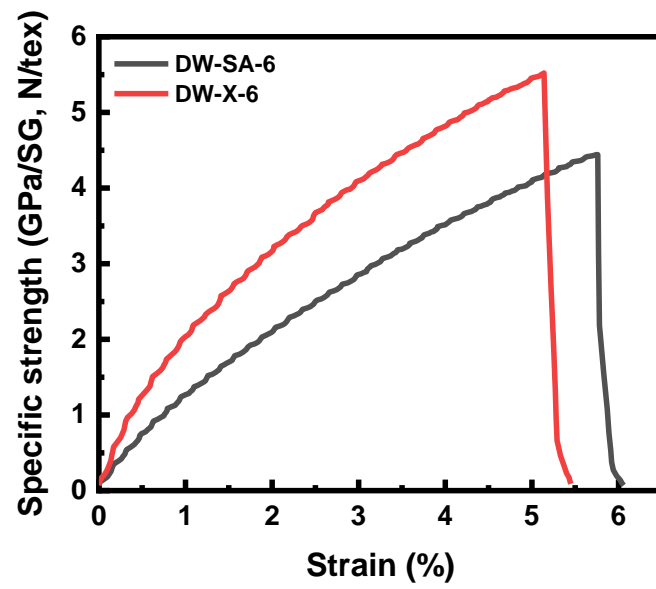
Fig. 4.12. The stress-strain curve of DW-SA-6 and DW-X-6.
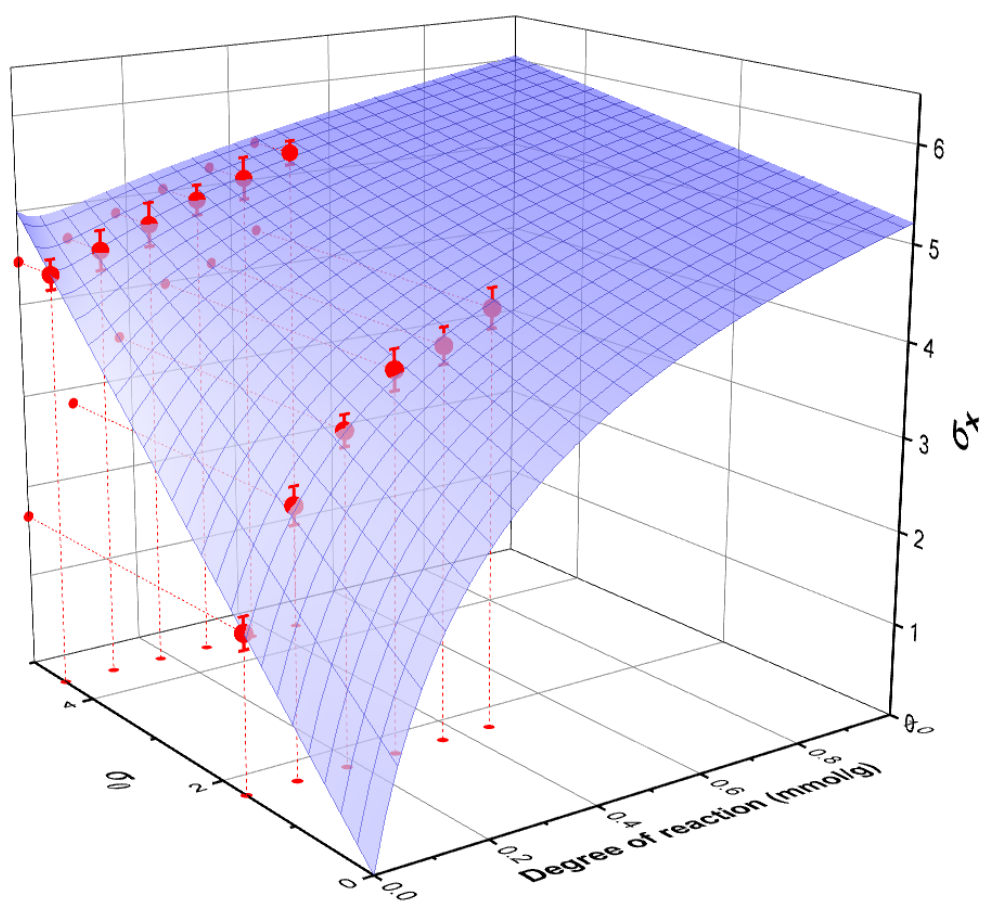
Fig. 4.13. Estimated specific strength of CNTY against degree of reaction and initial strength of CNTY.
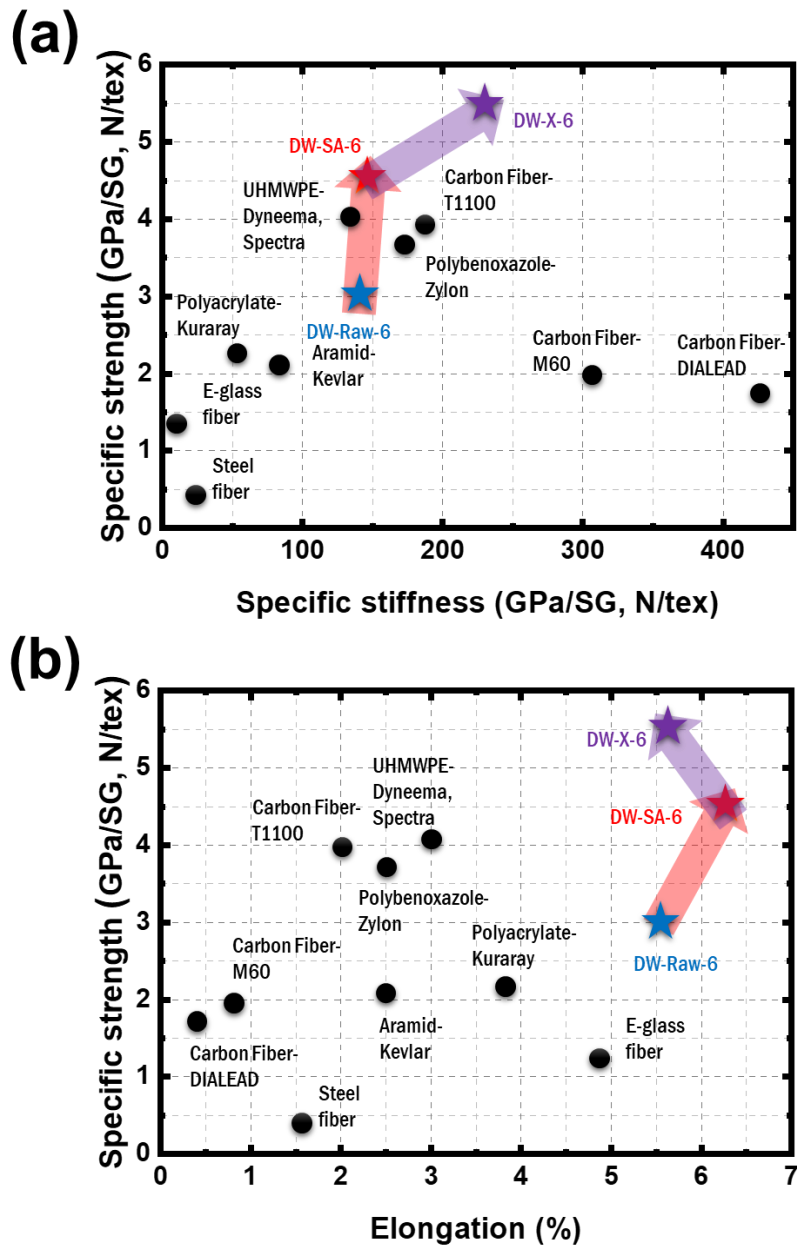
Fig. 4.14. Ashby plot of specific strength versus (a) specific stiffness and (b) elongation of various fibers (circle) with CNTY from this work (star).

4.4 Conclusion

A simplified model was developed for the strength of crosslinked CNT yarn based on crosslinking method devised in this work. According to the model, main factors influencing the strength of CNT yarn are flexural rigidity and polar component of surface energy increasing by linking reagent. Low surface energy and high flexural rigidity prevent CNT to dense packing, which is unfavorable for crosslinking. Tendency of affinity between linking reagent and surface of CNT fitted well to strength of crosslinked CNT yarn, concluding low magnitude of interaction energy leads to high strength yarn by increasing polar component of surface energy. On the other hand, junction between CNT and linking reagent from crosslinking increased curvature energy of graphitic layer in CNT, leading to decrease in strength of the yarn. Through calculating distortion energy loaded on CNT by various junctions, point type or at least pentagon type junction is suitable for crosslinking. Based on the criterion for high strength CNT yarn developed, we designed crosslinking scheme and fabricated CNT yarn with strength of 5.4 N/tex on average. Strength of CNT yarn has increased 20% from that of pristine CNT yarn. Also, increased strength is 93% of estimated maximum strength achievable through our crosslinking reaction. Through the experimental results, it is proven our model and theory well fit to real CNT yarn and can be the guideline for high strength CNT yarn.

4.5 Reference

[1] Y.-L. Li, I.A. Kinloch, A.H. Windle, Direct Spinning of Carbon Nanotube Fibers from Chemical Vapor Deposition Synthesis, Science 304(5668) (2004) 276-278.

[2] S.W. Kim, T. Kim, Y.S. Kim, H.S. Choi, H.J. Lim, S.J. Yang, C.R. Park, Surface modifications for the effective dispersion of carbon nanotubes in solvents and polymers, Carbon 50(1) (2012) 3-33.

[3] J.N. Coleman, U. Khan, W.J. Blau, Y.K. Gun'ko, Small but strong: A review of the mechanical properties of carbon nanotube–polymer composites, Carbon 44(9) (2006) 1624-1652.

[4] Z. Spitalsky, D. Tasis, K. Papagelis, C. Galiotis, Carbon nanotube–polymer composites: Chemistry, processing, mechanical and electrical properties, Prog. Polym. Sci. 35(3) (2010) 357-401.

[5] W. Bauhofer, J.Z. Kovacs, A review and analysis of electrical percolation in carbon nanotube polymer composites, Compos. Sci. Technology 69(10) (2009) 1486-1498.

[6] F.H. Gojny, M.H.G. Wichmann, U. Köpke, B. Fiedler, K. Schulte, Carbon nanotube-reinforced epoxy-composites: enhanced stiffness and fracture toughness at low nanotube content, Composites Science and Technol. 64(15) (2004) 2363-2371.

[7] A. Allaoui, S. Bai, H.M. Cheng, J.B. Bai, Mechanical and electrical properties of a MWNT/epoxy composite, Compos. Sci. Technol. 62(15) (2002) 1993-1998.

[8] J.Y. Oh, S.J. Yang, J.Y. Park, T. Kim, K. Lee, Y.S. Kim, H.N. Han, C.R. Park, Easy Preparation of Self-Assembled High-Density Buckypaper with Enhanced Mechanical Properties, Nano Lett. 15(1) (2015) 190-197.

[9] J.Y. Oh, Y.S. Kim, Y. Jung, S.J. Yang, C.R. Park, Preparation and Exceptional Mechanical Properties of Bone-Mimicking Size-Tuned Graphene Oxide@Carbon Nanotube Hybrid Paper, ACS Nano 10(2) (2016) 2184-2192.

157

[10] J.Y. Oh, Y. Jung, Y.S. Cho, J. Choi, J.H. Youk, N. Fechler, S.J. Yang, C.R. Park, Metal–Phenolic Carbon Nanocomposites for Robust and Flexible Energy-Storage Devices, ChemSusChem 10(8) (2017) 1675-1682.

[11] J.Y. Oh, Y.S. Choi, S.J. Yang, J. Kim, H.S. Choi, G.D. Choi, C.H. Yun, B.K. Lee, C.R. Park, Effect of microstructure and morphological properties of carbon nanotubes on the length reduction during melt processing, Compos. Sci. Technol. 112 (2015) 42-49.

[12] M.-F. Yu, B.S. Files, S. Arepalli, R.S. Ruoff, Tensile Loading of Ropes of Single Wall Carbon Nanotubes and their Mechanical Properties, Phys. Rev. Lett. 84(24) (2000) 5552-5555.

[13] M.-F. Yu, O. Lourie, M.J. Dyer, K. Moloni, T.F. Kelly, R.S. Ruoff, Strength and Breaking Mechanism of Multiwalled Carbon Nanotubes Under Tensile Load, Science 287(5453) (2000) 637-640.

[14] J. Jia, J. Zhao, G. Xu, J. Di, Z. Yong, Y. Tao, C. Fang, Z. Zhang, X. Zhang, L. Zheng, Q. Li, A comparison of the mechanical properties of fibers spun from different carbon nanotubes, Carbon 49(4) (2011) 1333-1339.

[15] X. Zhang, Q. Li, Y. Tu, Y. Li, J.Y. Coulter, L. Zheng, Y. Zhao, Q. Jia, D.E. Peterson, Y. Zhu, Strong Carbon-Nanotube Fibers Spun from Long Carbon-Nanotube Arrays, Small 3(2) (2007) 244-248.

[16] Q.W. Li, X.F. Zhang, R.F. DePaula, L.X. Zheng, Y.H. Zhao, L. Stan, T.G. Holesinger, P.N. Arendt, D.E. Peterson, Y.T. Zhu, Sustained Growth of Ultralong Carbon Nanotube Arrays for Fiber Spinning, Adv. Mater. 18(23) (2006) 3160-3163.

[17] S. Zhang, L. Zhu, M. Minus, H. Chae, S. Jagannathan, C.-P. Wong, J. Kowalik, L. Roberson, S. Kumar, Solid-state spun fibers and yarns from 1-mm long carbon nanotube forests synthesized by water-assisted chemical vapor deposition, J. Mater. Sci. 43(13)

(2008) 4356-4362.

[18] F.A. Hill, T.F. Havel, A.J. Hart, C. Livermore, Enhancing the tensile properties of continuous millimeter-scale carbon nanotube fibers by densification, ACS Appl. Mater. Interfaces 5(15) (2013) 7198-207.

[19] X. Zhang, Q. Li, T.G. Holesinger, P.N. Arendt, J. Huang, P.D. Kirven, T.G. Clapp, R.F. DePaula, X. Liao, Y. Zhao, L. Zheng, D.E. Peterson, Y. Zhu, Ultrastrong, Stiff, and Lightweight Carbon-Nanotube Fibers, Adv. Mater. 19(23) (2007) 4198-4201.

[20] X.-H. Zhong, Y.-L. Li, Y.-K. Liu, X.-H. Qiao, Y. Feng, J. Liang, J. Jin, L. Zhu, F. Hou, J.-Y. Li, Continuous Multilayered Carbon Nanotube Yarns, Adv. Mater. 22(6) (2010) 692-696.

[21] Y. Jung, T. Kim, C.R. Park, Effect of polymer infiltration on structure and properties of carbon nanotube yarns, Carbon 88 (2015) 60-69.

[22] K. Liu, Y. Sun, X. Lin, R. Zhou, J. Wang, S. Fan, K. Jiang, Scratch-Resistant, Highly Conductive, and High-Strength Carbon Nanotube-Based Composite Yarns, ACS Nano 4(10) (2010) 5827-5834.

[23] S. Li, X. Zhang, J. Zhao, F. Meng, G. Xu, Z. Yong, J. Jia, Z. Zhang, Q. Li, Enhancement of carbon nanotube fibres using different solvents and polymers, Compos. Sci. Technol. 72(12) (2012) 1402-1407.

[24] L. Kai, S. Yinghui, Z. Ruifeng, Z. Hanyu, W. Jiaping, L. Liang, F. Shoushan, J. Kaili, Carbon nanotube yarns with high tensile strength made by a twisting and shrinking method, Nanotechnology 21(4) (2010) 045708.

[25] K. Koziol, J. Vilatela, A. Moisala, M. Motta, P. Cunniff, M. Sennett, A. Windle, High-Performance Carbon Nanotube Fiber, Science 318(5858) (2007) 1892-1895.

[26] Y.-O. Im, S.-H. Lee, T. Kim, J. Park, J. Lee, K.-H. Lee, Utilization of carboxylic functional groups generated during purification of carbon nanotube fiber for its strength

improvement, Appl. Surf. Sci. 392 (2017) 342-349.

[27] O.-K. Park, H. Choi, H. Jeong, Y. Jung, J. Yu, J.K. Lee, J.Y. Hwang, S.M. Kim, Y. Jeong, C.R. Park, M. Endo, B.-C. Ku, High-modulus and strength carbon nanotube fibers using molecular cross-linking, Carbon 118 (2017) 413-421.

[28] J. Min, J.Y. Cai, M. Sridhar, C.D. Easton, T. R. Gengenbach, J. McDonnell, W. Humphries, S. Lucas, High performance carbon nanotube spun yarns from a crosslinked network, Carbon 52 (2013) 520-527.

[29] C.F. Cornwell, C.R. Welch, Very-high-strength (60-GPa) carbon nanotube fiber design based on molecular dynamics simulations, J. Chem. Phys. 134(20) (2011) 204708.

[30] Y. Jung, Y.C. Jeong, J.H. Kim, Y.S. Kim, T. Kim, Y.S. Cho, S.J. Yang, C.R. Park, One step preparation and excellent performance of CNT yarn based flexible micro lithium ion batteries, Energy Storage Mater. 5 (2016) 1-7.

[31] J. Choi, Y. Jung, S.J. Yang, J.Y. Oh, J. Oh, K. Jo, J.G. Son, S.E. Moon, C.R. Park, H. Kim, Flexible and Robust Thermoelectric Generators Based on All-Carbon Nanotube Yarn without Metal Electrodes, ACS Nano 11(8) (2017) 7608-7614.

[32] J. Lee, D.M. Lee, Y. Jung, J. Park, H.S. Lee, Y.K. Kim, C.R. Park, H.S. Jeong, S.M. Kim, Direct spinning and densification method for high-performance carbon nanotube fibers, Nat. Commun. 10(1) (2019) 2962.

[33] Y.S. Cho, H. Kim, M. Byeon, D.Y. Kim, H. Park, Y. Jung, Y. Bae, M. Kim, D. Lee, J. Park, K. Kang, D. Im, C.R. Park, Enhancing the cycle stability of Li–O2 batteries via functionalized carbon nanotube-based electrodes, J. Mater. Chem. A 8(8) (2020) 4263-4273.

[34] P.-X. Hou, B. Yu, Y. Su, C. Shi, L.-L. Zhang, C. Liu, S. Li, J.-H. Du, H.-M. Cheng, Double-wall carbon nanotube transparent conductive films with excellent performance, J. Mater. Chem. A 2(4) (2014) 1159-1164.

[35] S. Sarkar, E. Bekyarova, S. Niyogi, R.C. Haddon, Diels-Alder chemistry of graphite and graphene: graphene as diene and dienophile, J. Am. Chem. Soc. 133(10) (2011) 3324-7.

[36] S. Sarkar, E. Bekyarova, R.C. Haddon, Chemistry at the Dirac Point: Diels–Alder Reactivity of Graphene, Acc. Chem. Res. 45(4) (2012) 673-682.

[37] L. Jin, T. Agag, H. Ishida, Bis(benzoxazine-maleimide)s as a novel class of high performance resin: Synthesis and properties, Eur. Polym. J. 46(2) (2010) 354-363.

[38] D.K. Owens, R.C. Wendt, Estimation of the surface free energy of polymers, J. Appl. Polym. Sci. 13(8) (1969) 1741-1747.

[39] M.S. Dresselhaus, G. Dresselhaus, R. Saito, A. Jorio, Raman spectroscopy of carbon nanotubes, Phys. Rep. 409(2) (2005) 47-99.

[40] M.S. Dresselhaus, A. Jorio, R. Saito, Characterizing graphene, graphite, and carbon nanotubes by Raman spectroscopy, Ann. Rev. Condens. Matter Phys. 1 (2010) 89-108.

[41] T.C. Hirschmann, P.T. Araujo, H. Muramatsu, X. Zhang, K. Nielsch, Y.A. Kim, M.S. Dresselhaus, Characterization of Bundled and Individual Triple-Walled Carbon Nanotubes by Resonant Raman Spectroscopy, ACS Nano 7(3) (2013) 2381-2387.

[42] A.C. Ferrari, J.C. Meyer, V. Scardaci, C. Casiraghi, M. Lazzeri, F. Mauri, S. Piscanec, D. Jiang, K.S. Novoselov, S. Roth, A.K. Geim, Raman Spectrum of Graphene and Graphene Layers, Phys. Rev. Lett. 97(18) (2006) 187401.

[43] E. Oh, H. Cho, J. Kim, J.E. Kim, Y. Yi, J. Choi, H. Lee, Y.H. Im, K.H. Lee, W.J. Lee, Super-Strong Carbon Nanotube Fibers Achieved by Engineering Gas Flow and Postsynthesis Treatment, ACS Appl. Mater. Interfaces 12(11) (2020) 13107-13115.

Part III. Maximization of tensile modulus and elongation of carbon nanotube yarn

Chapter 5 Effect of Controlling Behavior of Microbundle on Tensile Strain and Modulus of CNTY

5.1 Introduction

Carbon nanotubes (CNTs) are the most attractive materials as a filler for fiber-reinforced composite (FRC) and a component of super-strong fibers because of its outstanding mechanical strength and high aspect ratio [1-5]. In the early 2000s, manufacturing methodology of CNTYs was dominantly studied and introduced. The representing methods to produce CNTYs are liquid crystalline spinning, CNT array spinning and direct spinning [6-9]. Morphological features such as CNT alignment along the yarn axis and twist angle were widely investigated to improve mechanical properties of CNTYs [10-15]. Though a fiber implementing the mechanical properties of CNT have not yet been reported, recent advances in CNTYs have been directed toward controlling the interaction between CNTs, which determines the tensile performance of CNTY. The tensile properties of CNTY scales with the structural factor of constituent CNTs and microbundle as long as the intertube friction dominantly determines the tensile properties of CNTY [16-19]. The theoretical calculation has predicted that the achievable strength of CNTY could be comparable to that of CNT if the constituent CNTs are longer than a certain length and perfectly dense along the yarn axis [20].

163

In this chapter, we report a possible route to enhancing the tensile properties of CNTY, which are specific modulus and tensile elongation, through the modified *in-situ* direct spinning method, which are water gap control and air gap control. The tensile properties of CNTYs with various bundle structures was analyzed according to the theory in chapter 2 and 3. As a result, we successfully fabricated as-spun CNTY with an average modulus of 190 N/tex through air gap control and a tensile elongation of 12% through water gap control, exceeding that of previously ever-reported as-spun CNTY. From the bundling and orientation behavior analysis of CNTs, the self-assembly behavior control was suggested to be one of the most influential factors determining the tensile properties of the resultant as-directly-spun CNTY.

5.2 Experimental

Synthesis of DWCNTs and DWCNT yarns

A DWCNT yarn was synthesized by a floating catalyst chemical vapor deposition method using a vertical alumina tube reactor as chapter 3. The CNTY was spun on a bobbin after passing through water at the bottom of the vertical furnace at a spinning rate of 6 m/min. For the drawing, the yarn passed through the guide roller and reached the bobbin. The guide roller was located 8cm above the bobbin and 8cm sideways. For water gap control, the roller in water bath was located 3cm below compared to location at chapter 3. On the other hand, for air gap control, both the roller in water bath and the water surface went down by 3cm.

Characterization of CNT yarns

The nanostructure of CNTs was characterized by HR-TEM (JEM-2100F, JEOL) and Raman spectroscopy (RAMANplus, Nanophoton) using 532 nm laser. The thermal gravimetric analysis (TGA; SDT-Q600, TA Instruments) was used to measure the purity of CNTs in air atmosphere. The nanostructures of CNT were observed through field-emission transmission electron microscopy (JEM-3000F, JEOL, Japan). The internal structures of the CNT yarn were observed through field-emission scanning electron microscopy (SUPRA 55VP, Carl Zeiss, Germany) after cutting with a focused ion beam (FIB; Helios 650, FEI). Furthermore, the specific strength was calculated by linear density, which was determined by weighing 15 m-long CNT yarn, divided into a measured load of a single yarn with tensile stage (TST350, Linkam) at a gauge length of 10 mm and strain rate of 3 mm min^{-1}. In the case of the *in-situ* Raman analysis, the tensile

stage for which the sample was set at a gauge length of 30 mm was placed in a Raman device and measured when strain is applied to CNTY.

5.3 Result and discussion

Double-walled CNTs (DWCNT) are synthesized through floating catalyst chemical vapor deposition (FCCVD) as previous reports [21-25]. To control the self-assembly behavior of CNT, the *in-situ* direct spinning technique was modified by controlling water gap and air gap during spinning the aerogel-like CNT assembly, as shown in Fig 5.1. For air gap control, both the roller in water bath and the water surface went down by 3cm compared to normal *in-situ* direct spinning at chapter 3 (Fig. 5.1b). On the other hand, for water gap control, the roller in water bath was located 3cm below compared to normal *in-situ* direct spinning at chapter 3 (Fig. 5.1c). Still, the guide roller was located 8cm above the winding roller and 8cm sideways while the synthesized as-spun CNTY was drawn at the winding rate of 6 m/min without any additional treatments. Water gap and air gap controlled CNTY were named DW-WG-6 and DW-AG-6, respectively.

For comparison under the same conditions, the DWCNT with same structural factor in Chapter 3 was used. DWCNT with an outer diameter of about 5.5 nm (Fig. 3.2b) were obtained. According to the TGA thermogram in Fig. 3.2c, 79.2 wt% of CNTY is composed of DWCNT while 11.2 wt% and 9.2 wt% of the yarn are amorphous carbon and residual Fe, respectively [26]. A high amount of load-bearing unit, which is proportional to the amount of DWCNT, contributes to the mechanical performance. According to the Raman analysis, the intensity ratio of the D-band to G-band (I_D/I_G) was approximately 0.038 ± 0.009 (Fig. 3.2d), confirming that the DWCNT is highly crystalline.
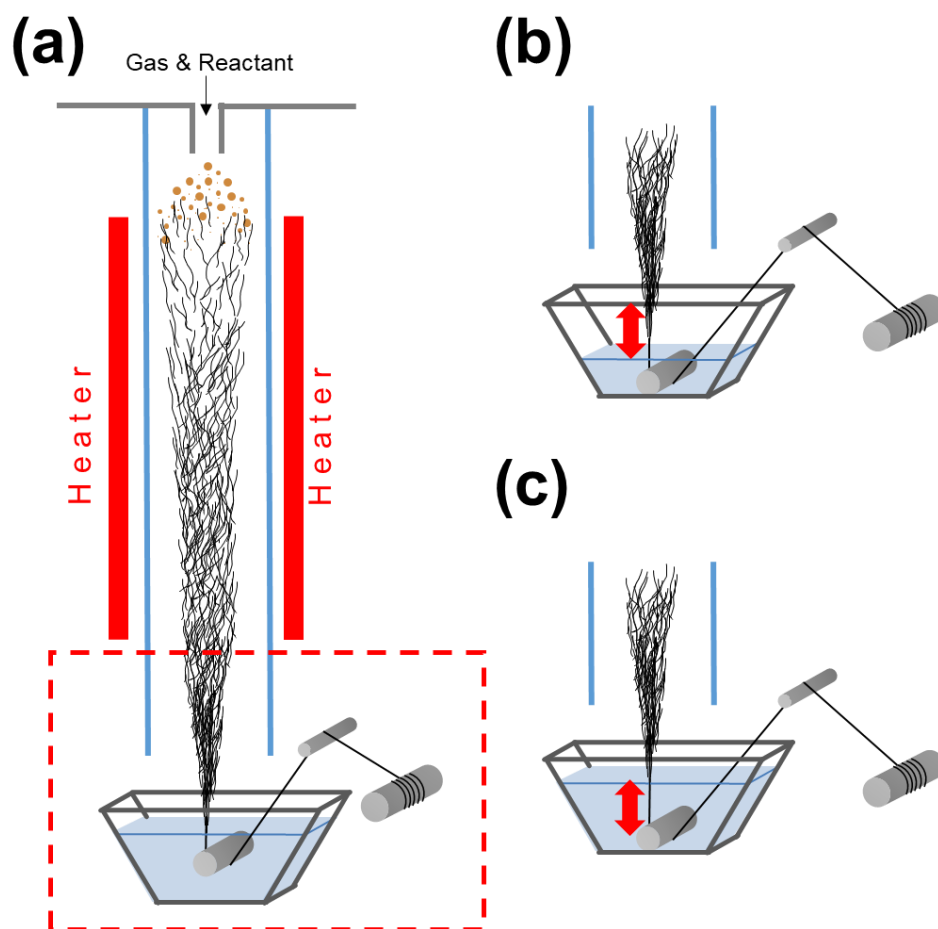
167

Fig. 5.1. Schematic image of (a) the normal, (b) air gap controlled and (c) water gap controlled *in-situ* direct spinning process.

5.3.1 Classical mechanics for elastic and plastic deformation

According to classical mechanics, the stress on a material can be expressed as a function of strain. Reversible deformation is called elastic deformation, and at this time, stress and strain show a linear relation as shown in equation (5.1),

$$\sigma = E\varepsilon \qquad\qquad (5.1)$$

where E is the modulus of elasticity, or Young's modulus. Young's modulus is known to be affected by the orientation of the fiber, which is a load bearing element, in the case of yarn. Elastic deformation is nonpermanent, i.e. the material returns to its original shape and size after the applied stress (load) is released.

When the applied stress exceeds the elastic region, plastic deformation takes place, i.e. the applied stress is no longer proportional to the strain. The point where the nonlinearity of the stress-strain relationship begins is known as the proportional limit. The applied stress is related to the induced strain in the plastic deformation region by the following Hollomon's equation (5.2),

$$\sigma = K\varepsilon^n \qquad\qquad (5.2)$$

where K and n are empirical parameters. Equation (5.2) is applicable when the strain applied to the material is less than the strain (ε_{UTM}) at the ultimate tensile stress. The results of CNTY analysis using Equations 5.1 and 5.2 are summarized in Table 5.1. In the case of CNTY, K and n are functions related to the bundling property covered in Part

2, but ε_{UTM} can be treated as a function of the length of the microbundle.

During plastic deformation, there is a competition between two phenomena in the strength of CNTY: load transfer due to bundling property and load transfer caused by stretching of microbundle. At this time, the case where the latter phenomenon is dominant is called plastic instability, and the material becomes unstable. The conditions of plastic instability are as in equation (5.3).

$$\sigma \geq \frac{d\sigma}{d\varepsilon} \tag{5.3}$$

If equation (5.2) is substituted in equation (5.3), the condition is established when the strain is greater than n, and this case is applied only to the almost perfect plastic material. CNTY does not meet the conditions, so CNTY generally shows stable plastic deformation. As a result, the strain at failure (ε_{fail}) and ε_{UTM} show similar values. However, if the two strains show a large difference, the section in which equation (5.2) does not hold, that is, the section that satisfies the condition of equation (5.3) is revealed. For this section to appear, a microbundle that is long enough for the stretching of the microbundle to become the main load transfer mechanism will be needed.

Furthermore, fractography of DW-AG-6 and DW-WG-6 (Fig. 5.2) is analyze to support the behavior of microbundle. In case of DW-AG-6, though brittle mode appeared, slippage mode was larger than that of DW-SA-6 (Fig. 2.4a), which led to a lower n value. However, the orientation of the failure initiation was higher than that of DW-SA-6, which led to a higher modulus. On the other hand, in the case of DW-WG-6, slippage mode appeared prominently with three steps. This is consistent with the results due to

high strain and plastic instability. That is, it can be confirmed that it is possible to maximize the tensile performance of the CNTY according to the behavior of the microbundle.

Table 5.1. Coefficient of classical mechanics of CNTYs.

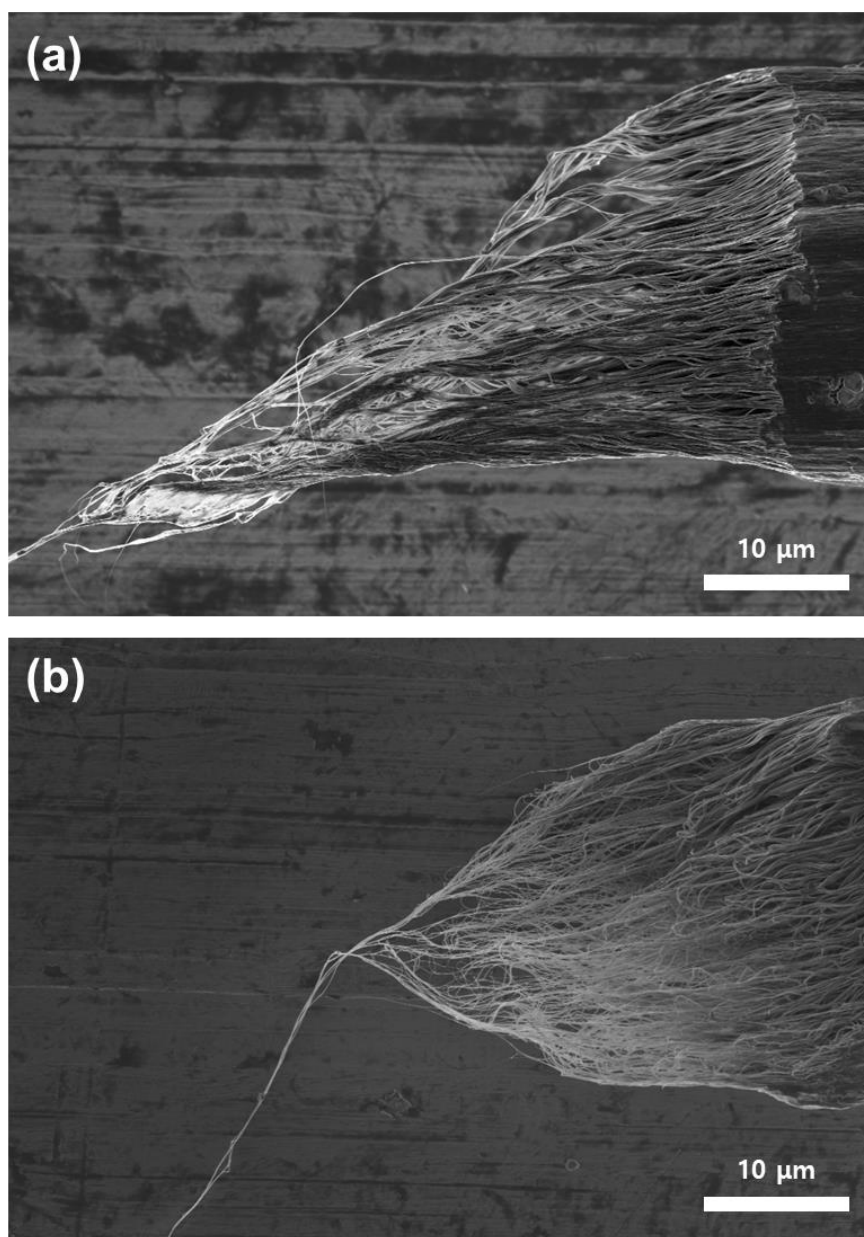| Sample	E (N/tex)	K (N/tex)	n	ε_{UTM} (%)	ε_{fail} (%)
DW-Raw-6	141	15.1	0.502	4.28	4.62
DW-SA-6	141	35.5	0.721	5.74	6.06
DW-X-6	226	34.2	0.610	5.14	5.45
DW-WG-6	97.5	7.56	0.429	10.3	12.6
DW-AG-6	190	14.6	0.446	5.66	6.04

Fig. 5.2. SEM image of fractography of (a) DW-AG-6 and (b) DW-WG-6.

5.3.2 Tensile property from self-assembly behavior

5.3.2.1 Strain specialization: water gap control

Through water gap controlled *in-situ* as-directly-spun CNTYs, we experimentally achieved tensile elongation of 12.5±0.9% with specific strength of 2.6±0.1 N/tex and specific stiffness of 97.5±8.0 N/tex through DW-WG-6 (Fig. 5.3). Although the strength and modulus were decreased, the tensile elongation was extremely high compared to the previous CNTYs. In addition, the cross-section of DW-WG-6 and low A_{eff} shown in Fig. 5.4 well explain the low specific strength of CNTY. Considering the results in Fig. 3.5c, it is estimated that the strength of the CNTY was reduced by applying excessive strain on the CNT assembly to Zone III as the drawing effect in water increased. Though the decrease in strength could be explained, the explanation for increase in elongation is still required. As a special feature, looking at the stress-strain curve in Fig. 5.3, it can be seen that DW-WG-6 withstands a given strain for a long time while reaching ultimate tensile strength. Unlike previous CNTYs where strain at ultimate tensile strength and rupture are almost same, DW-WG-6 showed a large difference (>2%) between the two strains. Since the result states that the load transfer is also performed in Zone IV, it is necessary to analyze bundling and orientation behavior.
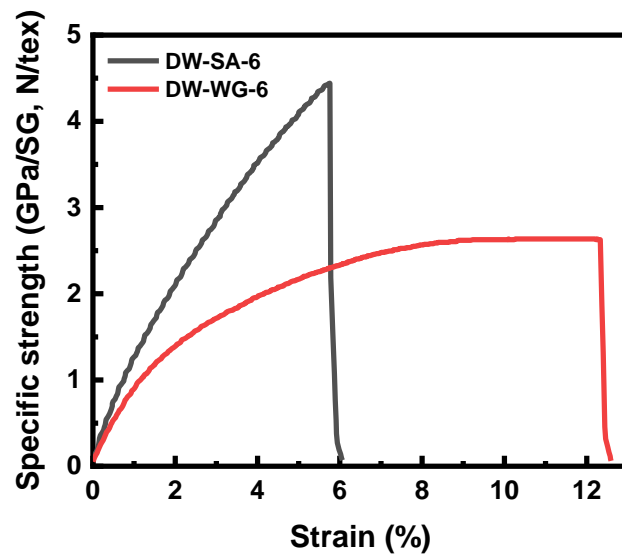
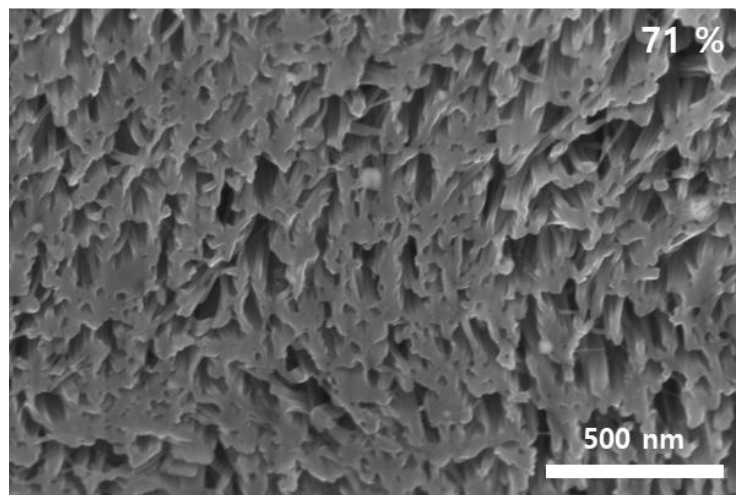**Fig. 5.3.** The stress-strain curve of DW-SA-6 and DW-WG-6.

Fig. 5.4. SEM micrographs of radial cross sections of FIB cuts of DW-WG-6 with effective area ratios in the upper right of the image.

The mechanical properties of CNTY are determined by the assembly of CNTs due to the characteristics of the load-bearing mechanism. DW-WG-6 was analyzed according to the assembly classification, which are bundling and orientation behavior. First, the bundling behavior of microbundles in CNTY in the static state (Fig. 5.5a) and the dynamic state (Fig. 5.5b) was analyzed using Raman spectroscopy. The key factor for the total area of shear failure depends on the extent of bundling of the CNT microbundles. The Raman band is strongly resonant under deformation of CNTs and the down shift rate of the G' peak implies load transfer efficiency between CNT with neighboring CNTs [27, 28]. The Raman G' peak of DWCNT yarns with Lorentzian fitting are provided in Fig 5.4a. Since the orthogonal electronic dispersion occurs when CNTs are in contact with each other and the G' peaks shift to lower energies, the G' peak shift is reflecting the inter-nanotube contact area. The G' peak shifted from 2667.7 cm^{-1} of DW-SA-6 to 2671.3 cm^{-1} of DW-WG-6 through water gap control. The upper shift of the peak from the initial static state resulted in low specific strength.

To further analyze the load-bearing mechanism of CNTY, DW-WG-6 was analyzed through *in-situ* Raman spectroscopy during tensile strain (Fig. 5.5b). The deformation behavior of DW-WG-6 was shown to have 4 zones same as CNTYs in chapter 3. The transfer efficiency of DW-WG-6 was -10.30 cm^{-1}/% in Zone I. The load transfer efficiency showed a significant decrease in absolute value compared to that of DW-SA-6 (-13.65 cm^{-1}/%). Such result matched with the modulus of DWCNT yarns. Furthermore, a significant difference was found in plastic region. The narrowed Zone II of DW-WG-6 states the assembly of CNT in DW-WG-6 was not able to withstand more yielding, resulting decrease in strength. On the other hand, the widened Zone III of DW-WG-6 indicates that the microbundles were able to transfer external load by efficient slippage between them. Excess strain given during spinning caused slippage between

microbundles across CNTY. This is presumed to maintain Zone III by preventing slippage from being concentrated in one place when an external load is given. As a result, Zone IV was also widened, which also resulted in the overall dispersion of partial failure in CNTY. According to the weakest link theory, probability of yarn rupture decreases when length of fiber increases. In case of CNTY, the increase in the length of microbundle resulted in resistance to catastrophic failure through dispersion of partial failure [29]. Thus, by preventing concentration of partial failure, it is estimated that the tensile elongation increased though the strength did not increase.

The orientation behavior of CNTY in the static state (Fig. 5.5a) and dynamic state (Fig. 5.5b) was analyzed using polarized Raman spectroscopy [10, 22]. At the initial state, the intensity factor ($I_{GII}/I_{G\perp}$) of DW-WG-6 was 5.44 ± 0.75 (Fig. 5.5a), showing significant decrease to that of DW-SA-6. Since it is well known that the elastic modulus is related to the initial orientation, decrease in polarized Raman factor well matches with low specific stiffness of DW-WG-6. Furthermore, the slight difference between DW-WG-6 and DW-SA-6 appeared in the dynamic state under tensile strain. While the orientation of CNTs in DW-SA-6 was constant regardless of strain (Fig 3.7c), the orientation of CNT in DW-WG-6 monotonically increased (Fig 5.5b). The orientation behavior rather supported bundling behavior even at Zone III and IV, leading to an efficient load transfer without total failure of CNTY. This water gap-based self-assembly of CNT mainly controls bundling behavior in the direction of improving tensile strain by even distribution of weak points.
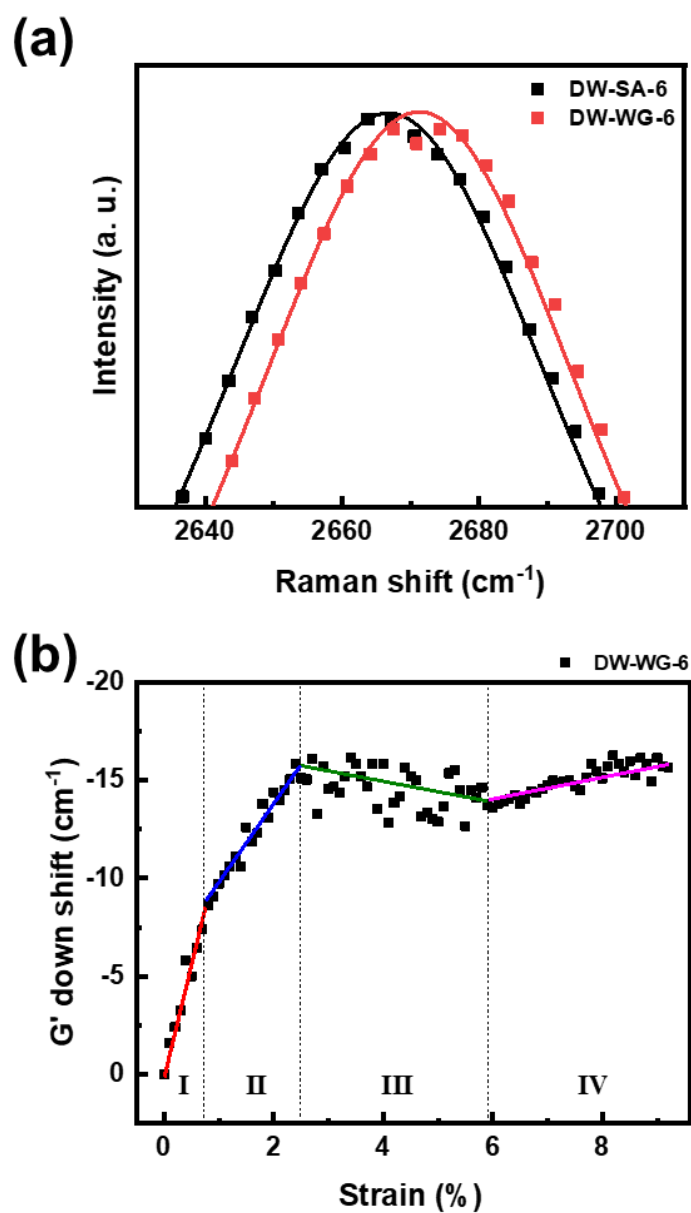
Fig. 5.5. (a) Raman spectra of the G' peak (symbol) that is fitted using a Lorentzian function (solid line) of DWCNT yarns. (b) The down shift rate of the G' peak of DW-WG-6 during tensile loading.
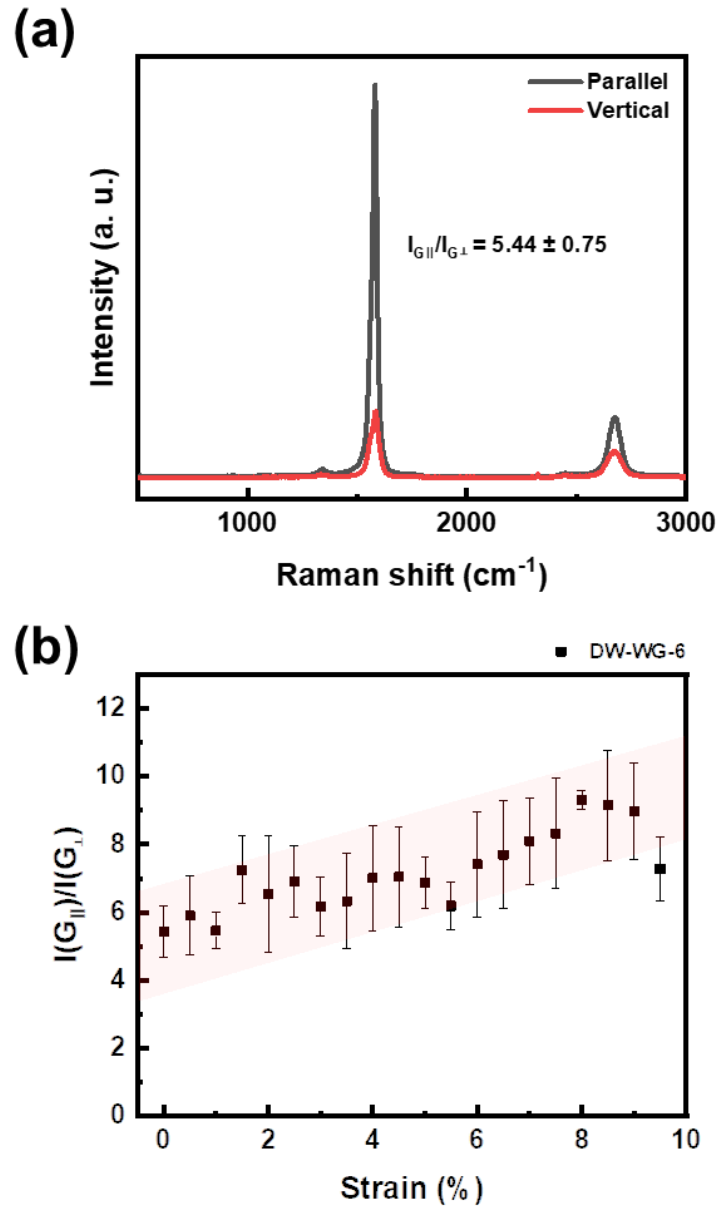
Fig. 5.6. (a) The polarwized Raman spectrum of DW-WG-6 and (b) polarized Raman intensity factor of DW-WG-6 during tensile loading.

5.3.2.2　Modulus specialization: air gap control

Through air gap controlled *in-situ* as-directly-spun CNTYs, we experimentally achieved specific stiffness of 190.4±18.5 N/tex with specific strength of 3.8±0.2 N/tex and elongation of 6.0±0.5% through DW-AG-6 (Fig. 5.7). Compared to DW-SA-6, DW-WG-6 showed similar strength and elongation. Rather, the difference appeared on the modulus and outline of the stress-strain curve. Though the modulus had increased, the outline of stress-strain curve returned to that of DW-Raw-6. In addition, the cross-section of DW-AG-6 and low A_{eff} shown in Fig. 5.8 well explain the low specific strength of CNTY. Considering the results in Fig. 3.5c, it is estimated that the strength of the CNTY was maintained by applying strain comparable to that of DW-SA-6 on the CNT assembly to Zone III as the drawing effect in air increased. As a special feature, looking at the stress-strain curve in Fig. 5.7, it can be seen that load transfer in plastic region of DW-AG-6 has been decreased. Since the change in the outline of the stress-strain curve means that there is a large change in Zone II, it is necessary to analyze bundling and orientation behavior.
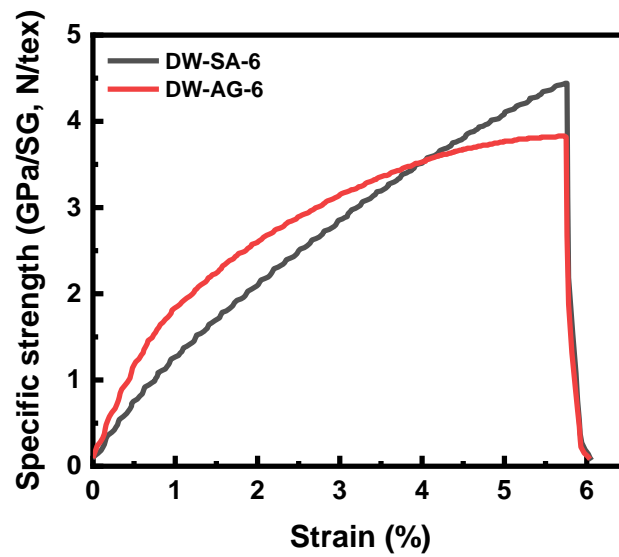
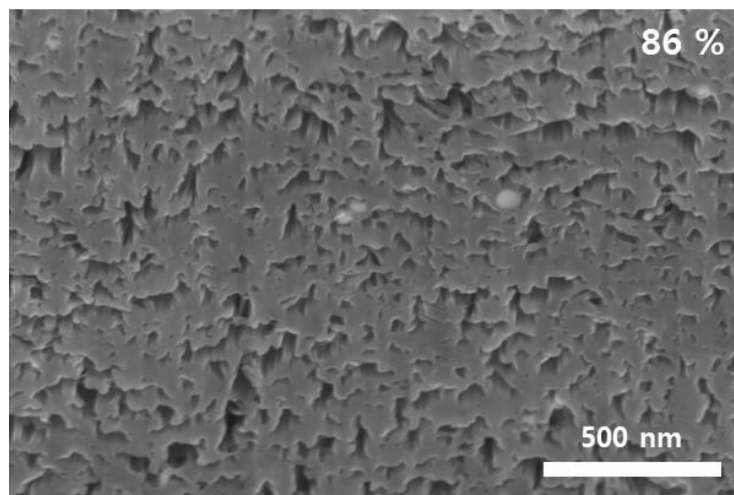**Fig. 5.7.** The stress-strain curve of DW-SA-6 and DW-AG-6.

Fig. 5.8. SEM micrographs of radial cross sections of FIB cuts of DW-AG-6 with effective area ratios in the upper right of the image.

DW-AG-6 was analyzed according to the assembly classification, which are bundling and orientation behavior. First, the bundling behavior of microbundles in CNTY in the static state (Fig. 5.9a) and the dynamic state (Fig. 5.9b) was analyzed using Raman spectroscopy. The Raman G' peak of DWCNT yarns with Lorentzian fitting are provided in Fig 5.9a. The G' peak shifted from 2667.7 cm^{-1} of DW-SA-6 to 2668.3 cm^{-1} of DW-AG-6 through air gap control. The negligible upper shift of the peak from the initial static state resulted in comparable specific strength.

To further analyze the load-bearing mechanism of CNTY, DW-AG-6 was analyzed through *in-situ* Raman spectroscopy during tensile strain (Fig. 5.9b). The deformation behavior of DW-AG-6 was shown to have 4 zones same as CNTYs in chapter 3. The transfer efficiency of DW-WG-6 was -19.77 cm^{-1}/% in Zone I. The load transfer efficiency showed a significant increase in absolute value compared to that of DW-SA-6 (-13.65 cm^{-1}/%). Such result matched with the significant increase in modulus from 141 N/tex of DW-SA-6 to 190 N/tex of DW-AG-6. Furthermore, a difference was also found in plastic region. The narrowed Zone II of DW-WG-6 states the assembly of CNT in DW-WG-6 was not able to withstand more yielding, resulting decrease in strength with change in outline of stress-strain curve. On the other hand, the widened Zone III of DW-AG-6 indicates that the microbundles were able to transfer external load by efficient slippage between them. Unlike concentrated slippage in DW-SA-6, higher strain given during spinning caused slippage between microbundles across CNTY. This is presumed to maintain Zone III by preventing slippage from being concentrated in one place when an external load is given. As a result, catastrophic failure as DW-SA-6 did not happen in DW-AG-6.

The orientation behavior of CNTY in the static state (Fig. 5.10a) and dynamic state

(Fig. 5.10b) was analyzed using polarized Raman spectroscopy [10, 22]. At the initial state, the intensity factor ($I_{GII}/I_{G\perp}$) of DW-WG-6 was 10.18 ± 1.24 (Fig. 5.10a), showing significant increase to that of DW-AG-6. Since it is well known that the elastic modulus is related to the initial orientation, inccrease in polarized Raman factor well matches with high specific stiffness of DW-AG-6. Furthermore, the similar behavior between DW-WG-6 and DW-SA-6 appeared in the dynamic state under tensile strain. While the orientation of CNTs in both CNTYs was constant regardless of strain (Fig 3.7c and 5.6b). Compared to water-gap control, this air gap-based self-assembly control of CNT mainly affects the orientation of CNT rather than bundling behavior.
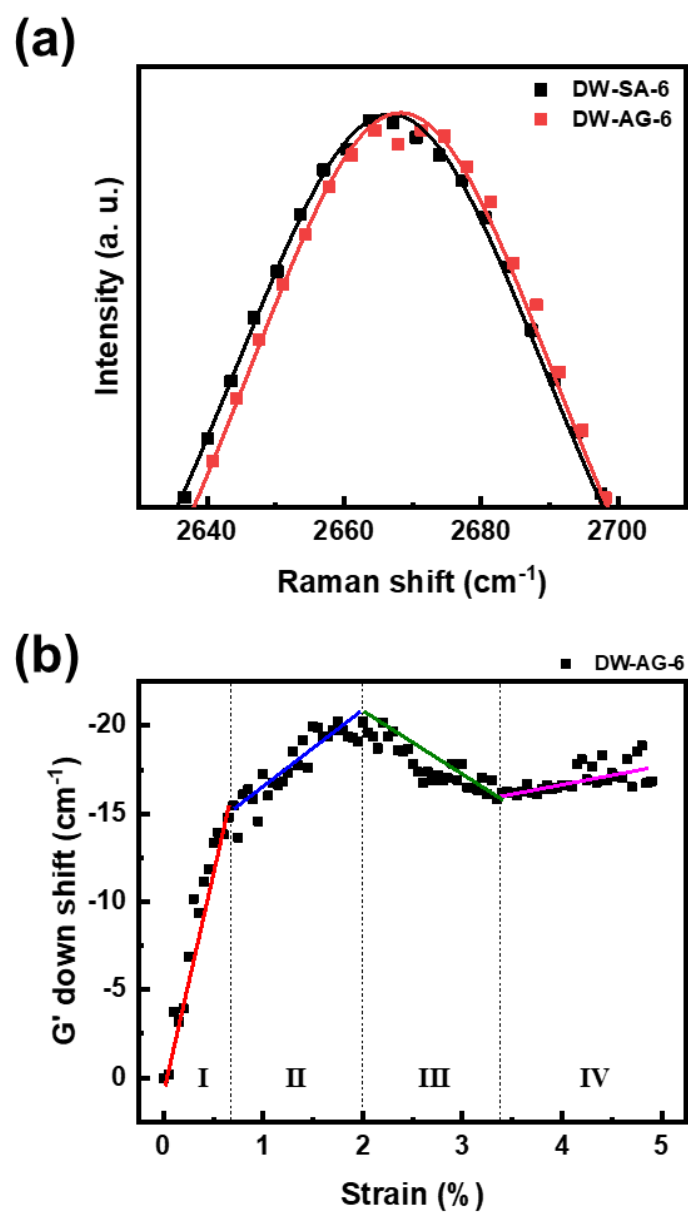
Fig. 5.9. (a) Raman spectra of the G' peak (symbol) that is fitted using a Lorentzian function (solid line) of DWCNT yarns. (b) The down shift rate of the G' peak of DW-AG-6 during tensile loading.
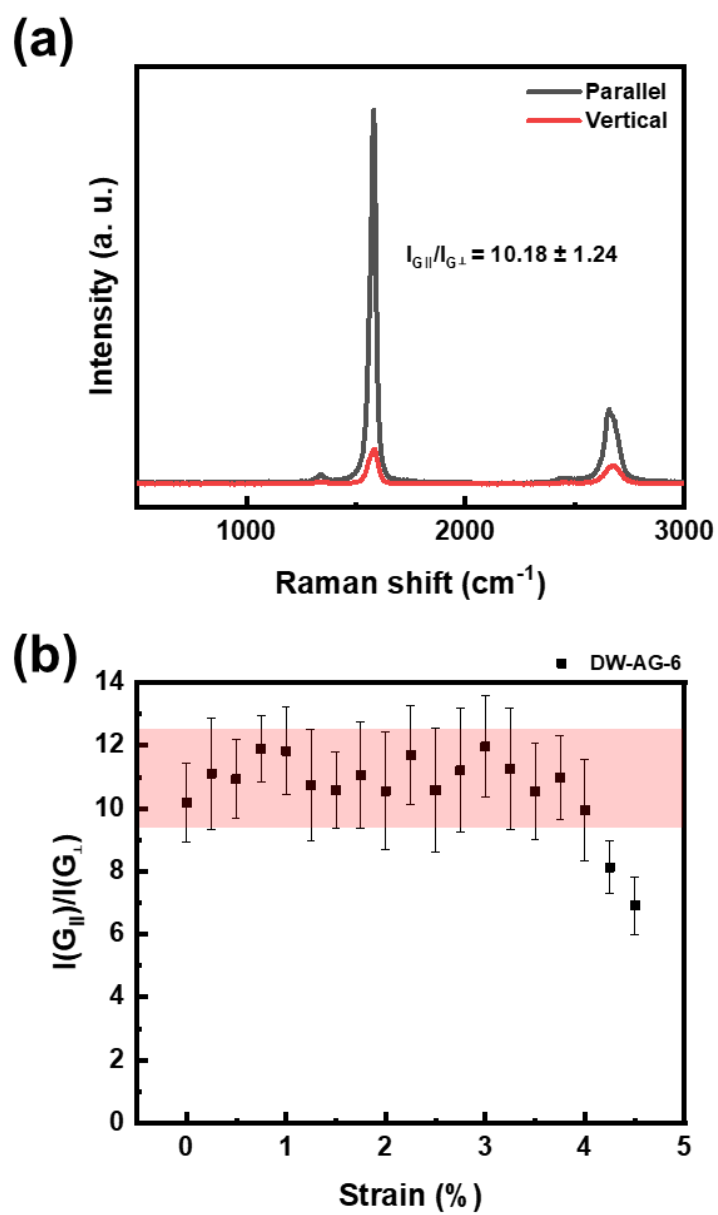
Fig. 5.10. (a) The polarwized Raman spectrum of DW-AG-6 and (b) polarized Raman intensity factor of DW-AG-6 during tensile loading.

The specific strength, specific stiffness, and elongation of CNTYs were compared with those of various state-of-the-art high-performance fibers and metals from industry (Fig. 5.11). Even the commercialized state-of-the-art materials do not possess both high specific tensile strength and elongation or specific stiffness. Our CNTYs have high-average specific tensile strength (2.6 N/tex) as well as high-elongation (12.5 %) or specific strength (3.8 N/tex) as well as superfiber class modulus (190 N/tex).

Fig. 5.11. Ashby plot of specific strength versus (a) specific stiffness and (b) elongation of various fibers (circle) with CNTY from this work (star).

187

5.4 Conclusion

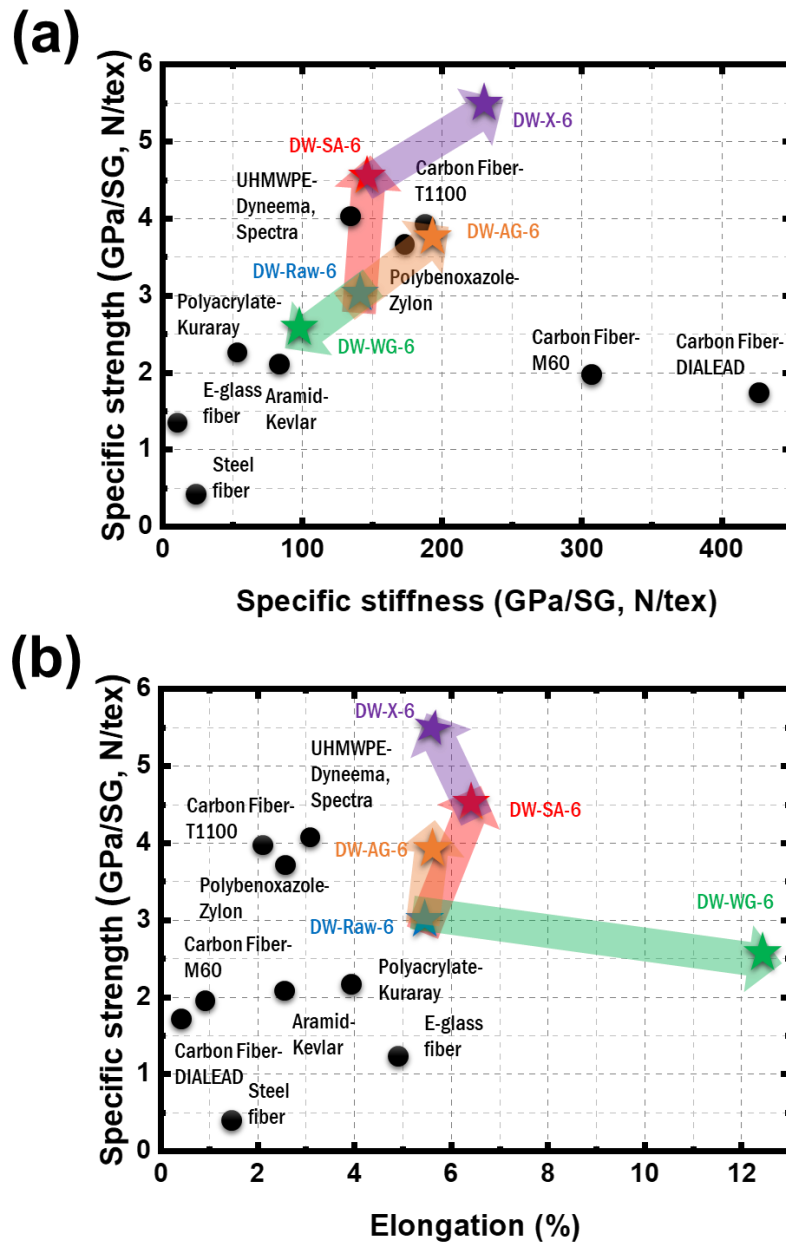We proposed a modified *in-situ* direct spinning technique to fabricate CNTYs with comparable or even superior properties to commercialized state-of-the-art fibers and engineering metals. The water-gap control induced even slippage in bundling behavior, resulting in longer microbundle. On the other hand, air-gap control induced orientation of CNT. However, direct evidence in nanostructure change should be revealed through further research. As a result, we were able to achieve CNTY with high modulus or high elongation without any post treatment, which is best ever reported tensile properties of the as-directly-spun experimental CNTY. These results highlighted the suitability of appropriate self-assembly engineering with a simple *in-situ* direct spinning technique for achieving tailor-fitted CNTYs. Consequently, we opened a new possibility of enhancing the tensile properties of CNTY.

5.5 Reference

[1] J.N. Coleman, U. Khan, W.J. Blau, Y.K. Gun'ko, Small but strong: A review of the mechanical properties of carbon nanotube–polymer composites, Carbon 44(9) (2006) 1624-1652.

[2] M.F. Yu, B.S. Files, S. Arepalli, R.S. Ruoff, Tensile loading of ropes of single wall carbon nanotubes and their mechanical properties, Phys. Rev. Lett. 84(24) (2000) 5552-5555.

[3] B. Vigolo, A. Pénicaud, C. Coulon, C. Sauder, R. Pailler, C. Journet, P. Bernier, P. Poulin, Macroscopic Fibers and Ribbons of Oriented Carbon Nanotubes, Science 290(5495) (2000) 1331-1334.

[4] M.-F. Yu, O. Lourie, M.J. Dyer, K. Moloni, T.F. Kelly, R.S. Ruoff, Strength and Breaking Mechanism of Multiwalled Carbon Nanotubes Under Tensile Load, Science 287(5453) (2000) 637-640.

[5] B.G. Demczyk, Y.M. Wang, J. Cumings, M. Hetman, W. Han, A. Zettl, R.O. Ritchie, Direct mechanical measurement of the tensile strength and elastic modulus of multiwalled carbon nanotubes, Mater. Sci. Eng. A 334(1–2) (2002) 173-178.

[6] L.M. Ericson, H. Fan, H. Peng, V.A. Davis, W. Zhou, J. Sulpizio, Y. Wang, R. Booker, J. Vavro, C. Guthy, A.N.G. Parra-Vasquez, M.J. Kim, S. Ramesh, R.K. Saini, C. Kittrell, G. Lavin, H. Schmidt, W.W. Adams, W.E. Billups, M. Pasquali, W.-F. Hwang, R.H. Hauge, J.E. Fischer, R.E. Smalley, Macroscopic, Neat, Single-Walled Carbon Nanotube Fibers, Science 305(5689) (2004) 1447.

[7] Y.-L. Li, I.A. Kinloch, A.H. Windle, Direct Spinning of Carbon Nanotube Fibers from Chemical Vapor Deposition Synthesis, Science 304(5668) (2004) 276-278.

[8] M. Zhang, K.R. Atkinson, R.H. Baughman, Multifunctional Carbon Nanotube Yarns by Downsizing an Ancient Technology, Science 306(5700) (2004) 1358-1361.

[9] H.W. Zhu, C.L. Xu, D.H. Wu, B.Q. Wei, R. Vajtai, P.M. Ajayan, Direct synthesis of long single-walled carbon nanotube strands, Science 296(5569) (2002) 884-886.

[10] K. Koziol, J. Vilatela, A. Moisala, M. Motta, P. Cunniff, M. Sennett, A. Windle, High-Performance Carbon Nanotube Fiber, Science 318(5858) (2007) 1892-1895.

[11] W. Xu, Y. Chen, H. Zhan, J.N. Wang, High-Strength Carbon Nanotube Film from Improving Alignment and Densification, Nano Lett. 16(2) (2016) 946-952.

[12] B. Alemán, V. Reguero, B. Mas, J.J. Vilatela, Strong Carbon Nanotube Fibers by Drawing Inspiration from Polymer Fiber Spinning, ACS Nano   (2015).

[13] M. Miao, Yarn spun from carbon nanotube forests: Production, structure, properties and applications, Particuology 11(4) (2013) 378-393.

[14] J. Zhao, X. Zhang, J. Di, G. Xu, X. Yang, X. Liu, Z. Yong, M. Chen, Q. Li, Double-Peak Mechanical Properties of Carbon-Nanotube Fibers, Small 6(22) (2010) 2612-2617.

[15] M. Miao, The role of twist in dry spun carbon nanotube yarns, Carbon 96 (2016) 819-826.

[16] X. Zhang, Q. Li, Y. Tu, Y. Li, J.Y. Coulter, L. Zheng, Y. Zhao, Q. Jia, D.E. Peterson, Y. Zhu, Strong Carbon-Nanotube Fibers Spun from Long Carbon-Nanotube Arrays, Small 3(2) (2007) 244-248.

[17] J. Jingjing, J. Zhao, G. Xu, J. Di, Z. Yong, Y. Tao, C. Fang, Z. Zhang, X. Zhang, L. Zheng, Q. Li, A comparison of the mechanical properties of fibers spun from different carbon nanotubes, Carbon 49(4) (2011) 1333-1339.

[18] J.J. Vilatela, J.A. Elliott, A.H. Windle, A Model for the Strength of Yarn-like Carbon Nanotube Fibers, ACS Nano 5(3) (2011) 1921-1927.

[19] A. Ghemes, Y. Minami, J. Muramatsu, M. Okada, H. Mimura, Y. Inoue, Fabrication and mechanical properties of carbon nanotube yarns spun from ultra-long multi-walled carbon nanotube arrays, Carbon 50(12) (2012) 4579-4587.

[20] B.I. Yakobson, G. Samsonidze, G.G. Samsonidze, Atomistic theory of mechanical relaxation in fullerene nanotubes, Carbon 38(11–12) (2000) 1675-1680.

[21] Y. Jung, Y.C. Jeong, J.H. Kim, Y.S. Kim, T. Kim, Y.S. Cho, S.J. Yang, C.R. Park, One step preparation and excellent performance of CNT yarn based flexible micro lithium ion batteries, Energy Storage Mater. 5 (2016) 1-7.

[22] J. Choi, Y. Jung, S.J. Yang, J.Y. Oh, J. Oh, K. Jo, J.G. Son, S.E. Moon, C.R. Park, H. Kim, Flexible and Robust Thermoelectric Generators Based on All-Carbon Nanotube Yarn without Metal Electrodes, ACS Nano 11(8) (2017) 7608-7614.

[23] O.-K. Park, H. Choi, H. Jeong, Y. Jung, J. Yu, J.K. Lee, J.Y. Hwang, S.M. Kim, Y. Jeong, C.R. Park, M. Endo, B.-C. Ku, High-modulus and strength carbon nanotube fibers using molecular cross-linking, Carbon 118 (2017) 413-421.

[24] J. Lee, D.M. Lee, Y. Jung, J. Park, H.S. Lee, Y.K. Kim, C.R. Park, H.S. Jeong, S.M. Kim, Direct spinning and densification method for high-performance carbon nanotube fibers, Nat. Commun. 10(1) (2019) 2962.

[25] Y.S. Cho, H. Kim, M. Byeon, D.Y. Kim, H. Park, Y. Jung, Y. Bae, M. Kim, D. Lee, J. Park, K. Kang, D. Im, C.R. Park, Enhancing the cycle stability of Li–O2 batteries via functionalized carbon nanotube-based electrodes, J. Mater. Chem. A 8(8) (2020) 4263-4273.

[26] P.-X. Hou, B. Yu, Y. Su, C. Shi, L.-L. Zhang, C. Liu, S. Li, J.-H. Du, H.-M. Cheng, Double-wall carbon nanotube transparent conductive films with excellent performance, J. Mater. Chem. A 2(4) (2014) 1159-1164.

[27] M.S. Dresselhaus, G. Dresselhaus, R. Saito, A. Jorio, Raman spectroscopy of carbon nanotubes, Phys. Rep. 409(2) (2005) 47-99.

[28] A.C. Ferrari, J.C. Meyer, V. Scardaci, C. Casiraghi, M. Lazzeri, F. Mauri, S. Piscanec, D. Jiang, K.S. Novoselov, S. Roth, A.K. Geim, Raman Spectrum of Graphene

and Graphene Layers, Phys. Rev. Lett. 97(18) (2006) 187401.

[29] N. Pan, T. Hua, Y. Qiu, Relationship Between Fiber and Yarn Strength, Tex. Res. J. 71(11) (2001) 960-964.

Conclusion and further works

Due to the inherently superb mechanical properties and high aspect ratios of CNTs, efforts to improve the mechanical properties of CNTYs which that exceed those of conventional high-strength fibers such as carbon fibers have continued over the last few decades. Nevertheless, though CNT is the most attractive materials in the fields of structural materials, CNT assembly including CNTY shows relatively very low mechanical performance in macroscopic scale comparing to the strength of individual CNTs in nanoscale. To overcome the limitation, new insight for correlation between properties of CNT and CNTY should be considered. The mechanical properties of CNT assembly depend on structural factors of CNT such as the length, number of walls, and the diameter of the nanotubes. Therefore, the most important issue to fabricate ultrahigh-strength CNTY is to control the nanostructure of CNTs and the microstructure of the CNT assembly by revisiting the hierarchy of CNTYs.

Aim of this study is to design and fabricate ultrahigh strength CNTY through both theoretical and empirical approaches based on structural factors and hierarchy of CNTYs. Though CNT is the most attractive materials in the fields of structural materials, CNT assembly shows relatively very low mechanical performance in macroscopic scale comparing to the strength of individual CNTs in nanoscale. As discussed in state-of-the-art, previous works based on conventional yarn mechanics does not provide a guideline and insight for high strength CNTY. Therefore, in this study, the method of maximizing the tensile strength of CNTY based on the theoretical derivation of strength of CNTY with empirical verification is proposed. On the basis of energy calculation, the actual load-bearing element, which is CNT microbundle, of CNTY is determined. By revisiting

failure mechanism, slippage of load-bearing element, the equation describing the specific strength of CNTYs is derived based on the structural factors of elementary bundle and microbundle, which are number and surface area fraction in contact, length and interfacial shear strength of microbundle relying on the intrinsic structure of CNTs. In particular, structural parameters such as length, diameter and the number of tube walls are considered as a key factor affecting from microbundle to the specific strength of CNTYs. Thus, relation between the specific strength of CNTYs and nanostructure of component CNT microbundle is suggested.

The reliability of theoretical approach is verified by comparing the specific strength of CNTYs made of various nanostructured CNTs. The effect of microstructure of CNT microbundle is investigated through *in-situ* direct spinning for CNTY strengthening. The specific strength of CNTYs with various bundle structures was analyzed and the maximum strength possible through the *in-situ* direct spinning technique was predicted with our CNTs. Furthermore, the strength of fabricated as-spun CNTY successfully reached 80% of the estimated maximum strength achievable. From the bundling and orientation behavior analysis of CNTs, the self-assembly behavior control was suggested to be one of the most influential factors determining the specific strength of the resultant as-directly-spun CNTY.

A simplified model of crosslinked CNT yarn to predict the main factors influencing the strength of the yarn is suggested in function of degree of reaction. To verify and realize the model, simple method of crosslinking based on carbon surface chemistry, which is cycloaddition, was hired. By giving variety to linking reagent or degree of reaction and analyzing junction of linking reagent and surface of CNT from reaction, developed model fitted well to experimental data, giving basis to the model as well as

194

insight to the strategy to strengthen CNTY. Applying the model, ultra-high strength CNTY was realized.

The method of maximizing the tensile strain and modulus of CNTY is suggested. The empirical approach, which is modified *in-situ* direct spinning, to increase elongation and modulus of CNTY was proposed. Through self-assembly control during spinning, elongation specialized CNTY and modulus specialized CNTY are prepared and analyzed based on bundling and orientation properties. However, the analysis of the length of the microbundle and the resulting change in strength could not be quantitatively analyzed in this study. Therefore, the relationship between the length of the microbundle and the strength of the CNTY should be analyzed experimentally for further works.

Abstract in Korean

본 연구는 고강도 탄소나노튜브 섬유 제조를 위한 이론 및 실험적 접근을 통하여 기존의 고강도 섬유의 역학적 물성을 넘어서는 초고강도 탄소나노튜브 섬유 제조를 목적으로 하였다. 탄소나노튜브 고유의 높은 역학적 성질과 종횡비로 인하여 탄소섬유와 같은 기존의 고강도 섬유 물성을 넘어서는 초고강도 탄소나노튜브 섬유를 제조하고자 하는 노력이 지난 수십년 동안 지속되어왔다. 그럼에도 불구하고 여전히 탄소나노튜브 섬유에서 탄소나노튜브 한 가닥이 갖는 우수한 역학적 특성이 발현되지 못하고있다. 이러한 한계를 극복하고자 탄소나노튜브와 섬유 사이의 상관관계에 대한 새로운 통찰이 요구된다. 탄소나노튜브는 나노튜브의 길이, 벽수, 직경 등의 나노구조에 따라서 다양한 물성을 갖는다. 따라서 초고강도 탄소나노튜브 섬유를 제조하기 위해서는 탄소나노튜브 섬유의 계층구조를 재정립하여 탄소나노튜브의 나노구조와 집합체 내에서의 탄소나노튜브 미세구조를 제어하여야 한다.

1장에서는 탄소나노튜브 섬유의 간략한 설명과 섬유의 역학적 성질에

영향을 미치는 관련 인자들을 소개하였다. 섬유의 역학적 성질을 향상시키고자 진행된 최근의 연구들을 탄소나노튜브의 구조적 요소들을 기반으로 분석함으로써 기존의 섬유역학으로는 고강도 탄소나노튜브 섬유를 제조하기에 한계가 있음을 보였다. 또한, 최근의 연구들을 종합하고 아직 해결되지 못한 이슈들과 해결방법을 모색하여 새로운 응력완화 메커니즘을 모색해야한다는 본 연구의 목적을 설명하였다.

2장에서는 CNTY의 하중 분산 메커니즘, 즉 CNTY의 파단 메커니즘을 기반으로 한 비강도 이론 방정식을 도출하였으며, CNTY의 구조적 인자와 섬유의 역학적 물성의 상관관계를 규명하였다. 최종적으로, 이론적 접근을 통하여 고강도 탄소나노튜브 섬유의 이상적인 구조를 제안하였다.

3장과 4장에서는 2장에서 도출된 탄소나노튜브와 나노집합체의 구조적 인자가 섬유의 강도에 미치는 영향을 실험적으로 확인하였다. 3장에서는 CNT의 자기조립 특성 제어에 의한 CNTY의 미세구조 형성과 인장강도 사이의 상관관계를 검증하였고, 4장에서는 CNTY내의 microbundle 간의 가교결합이 CNTY의 인장강도에 미치는 영향을 검증하였다. 그 결과 직접방사법에 의한 As-spun CNTY의 경우는 4.5 N/tex, 가교결합을 도입한

CNTY의 경우는 5.4 N/tex로 두 경우 모두 세계최고 성능의 CNTY을 제조할 수 있었다.

5장에서는 CNT의 인장 변형률과 탄성계수를 최대화하는 방법을 제안하였다. 탄소나노튜브의 축방향 자기조립 특성을 제어할 수 있도록 방사조건을 변화시킴으로써 인장 변형률 혹은 탄성계수를 선택적으로 극대화한 CNTY을 제조하였다. 이 연구는 CNTY의 인장성능 극대화를 위한 이론적 토대를 재정립했을 뿐만 아니라 세계최고성능의 CNTY을 제조해보임으로써, 학문적 측면뿐만이 아니라 산업적 측면으로도 매우 중요한 기여를 했다고 생각되며, 차후 연구에서 탄소나노튜브의 합성법 및 탄소나노튜브의 길이에 대한 영향력 분석 및 개선함으로써 더 높은 역학적 성능을 갖는 탄소나노튜브 섬유의 제조가 가능 할 것으로 예측된다.